

Computational Modeling of Tethered Undersea Kites for Power
Generation

by
Amirmahdi Ghasemi

A dissertation submitted to the Faculty of
Worcester Polytechnic Institute

In partial fulfillment of the requirement for the degree of
DOCTOR OF PHILOSOPHY IN MECHANICAL ENGINEERING

October 2017

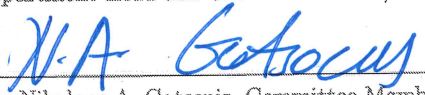
APPROVED:



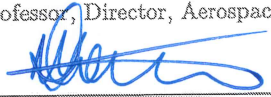
Dr. David J. Olinger, Advisor
Associate Professor, Aerospace Engineering Program, Worcester Polytechnic Institute.



Dr. Gretar Tryggvason, Advisor
Department Head and Charles A. Miller, Jr. Distinguished Professor, Johns Hopkins University



Dr. Nikolaos A. Gatsonis, Committee Member
Professor, Director, Aerospace Engineering Program, Worcester Polytechnic Institute.



Dr. Michael A. Demetriou, Committee Member
Professor, Aerospace Engineering Program, Worcester Polytechnic Institute.



Dr. Mark W. Richman, Graduate Committee Representative
Associate Professor, Aerospace Engineering Program, Worcester Polytechnic Institute.

Abstract

Ocean currents and tidal energy are significant renewable energy resources, and new concepts to extract this untapped energy have been studied in the last decades. Tethered undersea kite (TUSK) systems are an emerging technology which can extract ocean current energy. TUSK systems consist of a rigid-winged kite, or glider, moving in an ocean current. One proposed concept uses an extendable tether between the kite and a generator spool on a fixed or floating platform. As the kite moves across the current at high speeds, hydrodynamic forces on the kite tension the tether which extends to turn the generator spool.

Since the TUSK system is a new technology, the process of bringing a TUSK design to commercial deployment is long and costly, and requires understanding of the underlying flow physics. The use of computational simulation has proven to be successful in reducing development costs for other technologies. Currently, almost all computational tools for analysis of TUSK systems are based on linearized hydrodynamic equations in place of the full Navier-Stokes equations. In this dissertation, the development of a novel computational tool for simulation of TUSK systems is described. The numerical tool models the flow field in a moving three-dimensional domain near the rigid undersea kite wing. A two-step projection method along with Open Multi-Processing (OpenMP) on a regular structured grid is employed to solve the flow equations. In order to track the rigid kite, which is a rectangular planform wing with a NACA-0012 airfoil, an immersed boundary method is used. A slip boundary condition is imposed at the kite interface to decrease the computational run-time while accurately estimating the kite lift and drag forces. A PID control method is also used to adjust the kite pitch, roll and yaw angles during power (tether reel-out)

and retraction (reel-in) phases to obtain desired kite trajectories.

A baseline simulation study of a full-scale TUSK wing is conducted. The simulation captures the expected cross-current, figure-8 motions during a kite reel-out phase where the tether length increases and power is generated. During the following reel-in phase the kite motion is along the tether, and kite hydrodynamic forces are reduced so that net positive power is produced. Kite trajectories, hydrodynamic forces, vorticity contours near the kite, kite tether tension and output power are determined and analyzed. The performance and accuracy of the simulations are assessed through comparison to theoretical estimations for kite power systems. The effect of varying the tether (and kite) velocity during the retraction phase is studied. The optimum condition for the tether velocity is observed during reel-in phase to increase the net power of a cycle. The results match theoretical predictions for tethered wind energy systems. Moreover, the effect of the tether drag on the kite motion and resulting power output is investigated and compared with the results of the baseline simulation. The kite drag coefficient increases by 25% while the effect of the tether drag is included into the baseline simulation. It affects the trajectory and the velocity of the kite. However, it has a small effect on the power generation for the proposed concept of TUSK system.

Certain materials are included under the fair use exemption of the U.S. Copyright Law and have been prepared according to the fair use guidelines and are restricted from further use.

Acknowledgements

First and foremost, I want to express my sincerest gratitude to my supervisors, Professor David Olinger and Professor Gretar Tryggvason, for their supervision, advice, and guidance throughout the research. I have learned a lot from them and their wealth of experience and knowledge have been of immense help to me. I attribute my PhD degree to their encouragement and effort; without them, this thesis would not have been completed.

I would like to thank my thesis committee members, Prof. Nikolaos A. Gatsonis, Prof. Michael A. Demetriou, and Prof. Mark W. Richman for their help and support. I also would like to gratefully acknowledge the support of the NSF Energy for Sustainability Program through Grants CBET-1336130 and CBET-1033812.

I would like to thank ME department for their support during my PhD program. Special thanks to Mr. Siamak Najafi and his group for their help on using Linux servers on WPI Computational Center.

I am fortunate in having so many friends during my time at WPI. Dr. Ali Nematbakhsh, Dr. Mehdi Heydari, Dr. Morteza Khaleghi and everybody who helped me with this thesis, as well as expressing my apology that I could not mention all the names personally one by one.

Last but not least, I want to show my gratitude to my parents, who sincerely raised me with their caring and gentle love. Also, I would like to thank my brothers, Amirhossein and Amirreza, who are supportive, helpful and have always kept me in their thoughts through all these years. I love you all. You are more important to me than you realize.

Contents

List of Figures	vii
List of Tables	xiii
Nomenclature	xiii
1 Introduction	1
1.1 Literature Review	9
1.2 Modeling of Fluid-Solid Interaction	16
1.3 Goals and Contributions	17
2 Governing Equations and Numerical Methods	21
2.1 Mathematical Formulation	21
2.2 Boundary Conditions	23
2.3 Two-step Projection Method	24
2.4 Fluid-solid Interaction	25
2.5 Tether Modeling	26
2.6 Control Scheme	27
2.7 Numerical Algorithm	28
2.8 Time Step Restriction	30
2.9 Kite Lift and Drag Calculation	32

2.10	Moving Computational Domain	33
2.11	Slip Modeling at the Kite Interface	34
2.12	Tether Drag Modeling	37
3	Verification of the Computational Method	40
3.1	Grid and Reynolds Number Independency of the Computational Method	40
3.2	Moving Domain Verification	44
3.2.1	Free Fall of an Airfoil Wing in a 3D Fluid Container	46
3.2.2	A Moving Tethered Underwater Kite for Power Generation	47
3.3	The Effects of Slip and No-slip Boundary Conditions	49
3.4	The Effects of Domain Size on Numerical Results	55
4	Results	57
4.1	Two-dimensional Baseline Simulation	57
4.1.1	Parametric Study	63
4.2	Three-dimensional Baseline Simulation	70
4.2.1	Tether Retraction Velocity	80
4.2.2	Tether Drag Effect	83
5	Conclusion	90
5.1	Discussion and Conclusion	90
5.2	Recommendations for Future Work	92
	Bibliography	94

List of Figures

1.1	Ocean current distribution around the world. © NOAA.	1
1.2	TUSK system concept.	2
1.3	Fly-Gen configuration for airborne wind energy devices. a) A tethered flight of special gliders, design by Makani Power [8]. b) Flight with multiple wings, design by Joby Energy [9]. c) Aerodynamically shaped aerostats filled with lighter-than-air gas, design by Altaeros Energies [10]. d) Rotor thrust flying with the same turbines used for electrical power generation, design by Sky WindPower [11].	3
1.4	Fly-Gen configuration for underwater kite systems by Minesto UK, Ltd [12].	4
1.5	Ground-Gen configuration of TUSK systems.	5
1.6	Ocean current velocity around gulf stream.© Delft Institute for Earth Oriented Space Research	6
1.7	The outer portion of turbine blades compared to the kite in the TUSK systems.	9
1.8	Underwater kite systems design by SeaCurrent company [20].	11
2.1	a) Schematic diagram of the kite-tether system in which the attachment point is outside of the computational domain. b) zoom-in view.	27
2.2	Unstretched and actual tether lengths vs time.	29

2.3	Flow chart of the algorithm for modeling of a tethered undersea kite, based on the Navier-Stokes equations.	31
2.4	Schematic of a moving computational domain which is used in 3D baseline simulations instead of the fixed numerical domain to decrease the computational run-time.	33
2.5	Schematic of a kite (solid object) interface and a neighbor cell with a distance h normal to the kite interface.	36
2.6	Schematic of modeling of the tether drag.	38
3.1	a) Schematic diagram of the kite-tether system, and b) computational grid in 3D simulations. Not to scale.	41
3.2	Grid resolution effect in 3D simulations on: a) cross-current motion of the kite, b) power generation, c) tether force.	42
3.3	a) Schematic diagram of the kite-tether system and computational domain in 2D simulations. Not to scale. b) Numerical grid.	43
3.4	Grid refinement study in 2D simulations showing the effect of different grid resolutions on the kite position and velocity.	43
3.5	Schematic of the tethered kite in a fixed numerical domain to study Re independency for 3D simulations.	44
3.6	The effect of Reynolds number on the displacement of the kite center of mass in: a) x, b) y, and c) z directions, for 3D simulations.	45
3.7	The effect of varying Reynolds number in 2D simulations on the kite position and velocity.	45
3.8	Initial position of the airfoil wing in computational domains.	46
3.9	Displacement of the center of mass of the airfoil-wing free-falling in a fluid container in fixed and moving numerical domains.	47

3.10	Schematics of the moving and fixed computational domains for tethered kite which is placed across the uniform flow. Not to scale.	48
3.11	The comparison of the center of mass trajectory of a tethered kite placed in a uniform flow in moving and fixed computational domains.	49
3.12	Schematic of a 2D airfoil wing with zero angle of attack which is placed across the uniform current flow.	51
3.13	Lift and drag coefficients of a NACA-0012 airfoil wing at different grid resolutions for zero angle of attack ($AOA = 0$). The no-slip condition is imposed at the wing interface.	52
3.14	Drag coefficient of a NACA-0012 airfoil wing for different grid resolutions at zero angle of attack ($AOA = 0$). The slip condition is imposed at the wing interface.	53
3.15	Streamline around the airfoil wing at zero angle of attack ($AOA = 0$). The slip condition is imposed at the wing interface.	54
3.16	Drag, lift, and lift to drag ratio of the airfoil wing at three different angle of attack ($AOA = 0$). The slip condition at the wing interface is imposed.	54
3.17	a) The location of airfoil wing far from the inlet and far from the outlet. b) The location of the airfoil wing close to the outlet. c) The location of the an airfoil wing in the numerical domain in the baseline simulation that is tested in section 3.3.	55
3.18	Drag coefficient of the airfoil wing at three different domain sizes. The slip condition at the wing interface is imposed.	56

4.1	Snapshots of the kite position during a power-retraction cycle showing vorticity contours. The tethers are attached 5 m above the top of the computational domain.	59
4.2	Angle of attack of the kite vs time.	60
4.3	Trajectory of the kite vs time. The direction of the kite motion is shown by the arrows	61
4.4	Hydrodynamic lift and drag coefficient of the kite vs time.	61
4.5	Tethers tension vs time.	62
4.6	Tether velocity vs time.	62
4.7	Power obtained for successive cycles for a 2D tether kite system vs time.	62
4.8	Effect of the ratio of tether to current velocity on power output. Enlarged views show details of the power output during the power and retraction phases.	63
4.9	Comparison of power coefficients from the simulations with Loyd [15] prediction at $L/D = 0.6$	65
4.10	Effect of the kite density on power.	66
4.11	Effect of the kite to water density ratio on normalized power coefficient.	66
4.12	Power generated in different ocean current velocity.	66
4.13	Comparison of power generated in different ocean currents with V^3 curve fit.	67
4.14	Output power vs time for different ratios of tether to chord length.	68
4.15	Trajectory of the kite center of gravity with $L_t/c = 30$	68
4.16	Kite position and vorticity contours with $L_t/c = 30$ at various times.	69
4.17	Schematic diagram of the tethered underwater kite system and computational domain for the 3D baseline simulation. Not to scale.	71
4.18	Trajectory of kite center of mass vs time.	73

4.19	Top view of the kite position with flow vorticity (λ_2) contours.	74
4.20	Comparison of the actual and trim kite angles vs time. a) Pitch angle b) Roll angle, c) Yaw angle.	75
4.21	Effective and side-slip angles of attack of the kite vs time.	76
4.22	Lift, drag and resultant coefficients for the kite vs time	77
4.23	The ratio C_R/C_d for the kite.	77
4.24	Lift, drag, and resultant coefficients of the kite using a no-slip boundary condition at the kite interface.	78
4.25	Power output using a no-slip boundary condition at the kite interface.	78
4.26	Tether parameters in the 3D baseline simulation using slip condition at the kite interface.	79
4.27	Power output of 3D baseline simulation vs time.	80
4.28	The tether parameters at four different tether retraction velocities.	82
4.29	Power output vs time at four different tether retraction velocities.	83
4.30	a) The net power output at four different ratios of tether velocity during the reel-out phase to tether velocity during the reel-in phase (γ_{out}/γ_{in}). b) The net power output at four different ratios of tether tension during the reel-in phase to tether tension during the reel-out phase (T_{in}/T_{out}). c) The net power output at four different ratios of power output during the reel-in phase to power output during the reel-out phase (P_{in}/P_{out}).	84
4.31	Optimum power output at different ratios of tether reel-out to tether reel-in speed (γ_{out}/γ_{in}), tether force ratio (T_{in}/T_{out}), and power ratio of reel-in to reel-out (P_{in}/P_{out}) vs the cube of lift to drag ratio ($F_{out}/F_{in} =$ (C_l/C_d) ³) [34].	85
4.32	Hydrodynamic coefficients of the kite vs time	86

4.33 Comparison of kite drag coefficient with and without the tether drag effect.	86
4.34 The effect of the tether drag on the kite drag force.	87
4.35 The effect of the tether drag on the kite trajectory and velocity in the cross-current direction.	88
4.36 The effect of tether drag on the tether force.	88
4.37 The effect of tether drag on the power generation.	89

List of Tables

1.1	Comparison of TUSK and fixed marine turbine systems.	8
3.1	Input parameters for the tethered kite in the moving and fixed numerical domains.	50
4.1	Input parameters for 2D baseline simulation	58
4.2	Input parameters for the 3D baseline simulation using the moving numerical domain.	72

Nomenclature

A	area of the kite
ψ	volume-of-solid function, a scalar function
Δt	timestep
\vec{F}_B	body force per unit volume
\vec{F}_S	fluid-solid interaction force
\vec{F}_{tether}	tether force
g	gravity
CPU	central processing unit
GPU	graphic processing unit
\vec{V}	velocity vector
v	volume
t	time
p	pressure
\hat{n}	unit normal vector
\hat{t}	unit tangential vector
F_s	theoretical power coefficient
L/D	lift to drag ratio
K	tether spring stiffness

Re	Reynolds number
T_d	phase shift (unstretched tether length
V_c	current velocity
V_k	kite velocity
V_t	tether velocity
u_{so}	velocity of the solid object
x_s	location of the solid object
ρ_k	kite density
ρ_w	water density
ϵ	small value
μ	water dynamic viscosity
ν	kinematic viscosity
ρ	density
τ	shear stress tensor
a_s	acceleration of the solid object
c	kite chord length
C_L	lift coefficient
C_d	drag coefficient
$C_{damp.}$	damping coefficient of tether
$C_d^{tet.}$	tether drag coefficient
C_d^k	kite drag coefficient
C_R	resultant coefficient
C_p	power coefficient
A^T	transpose transformation matrix
I	moment of inertia

$\vec{\omega}_s$	angular acceleration of the solid object
\vec{r}	relative position vector
P	power
∇	del operator

Subscripts and Superscripts

$n, n + 1$	time levels
so	solid
s	tangential direction
t	tangential direction
T	test cell
l	fluid
$*$	interim value

Chapter 1

Introduction

Fossil fuels are presently used to satisfy the majority of global energy needs. Due to climate change concerns, researchers are studying sustainable energy technologies as alternatives to fossil fuels. One renewable energy resource that has not been adequately utilized is ocean and tidal currents. International Energy Agency stated that the potential exploitable ocean current energy resource is 800 TWh per year.

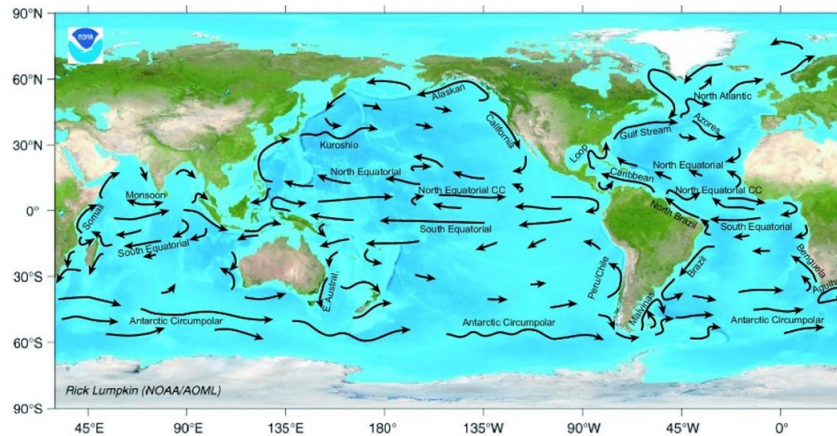


Figure 1.1: Ocean current distribution around the world. © NOAA.

For instance, the energy potential of Agulhas current off the coast of south Africa has been estimated at about 1913 GWh per year [1], while the Gulf Stream’s energy potential is about 219 GWh [2]. Tethered undersea kite systems (TUSK) are a pro-

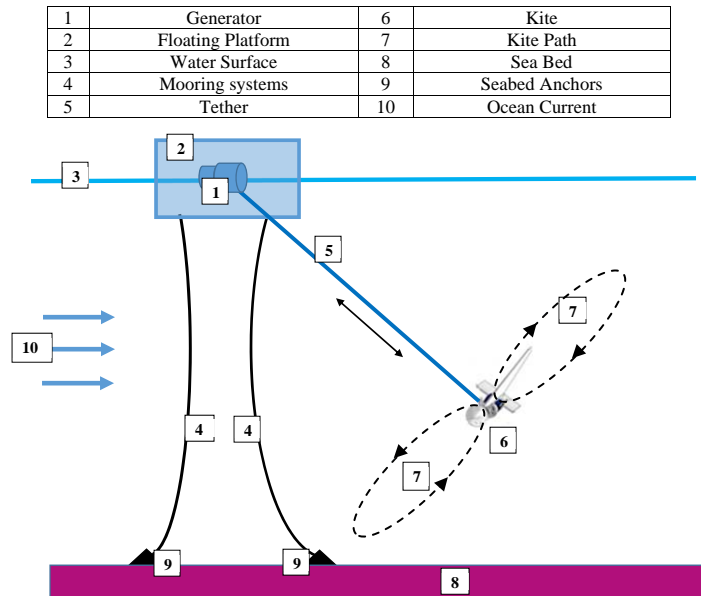


Figure 1.2: TUSK system concept.

posed technology which can extract ocean current energy. In TUSK systems, which were first proposed by Landberg [3], a rigid-winged kite is connected by a tether to a floating platform at the ocean surface as shown in Fig. 1.2. The rigid-winged kites in TUSK systems are similar to gliders in airborne kite energy devices [4]. Generated hydrodynamic forces, which are obtained solely due to the current passing over the kite, lead the kite moving across the current at high velocity. The exact path of the kite can be specified by controlling the motion of the kite about its pitch, roll and yaw axes.

There are two main configurations of extracting power for airborne kite energy systems, FlyGen and Ground-Gen configurations, and similar ideas can be used for underwater kite systems. In Fly-Gen devices, a wind turbine and generator on the kite itself produce on-board electric energy of the glider during its flight [5]. The obtained energy is transmitted to the ground by a tether which integrates electric ca-

bles. Fly-Gen systems have different principals such as wing lift, Buoyancy and static lift, and Rotor thrust (Fig. 1.3) [5]. There is another Fly-Gen concept that aims at exploiting high altitude wind energy by using a rotating aerostat which exploits the Magnus effect [6, 7].

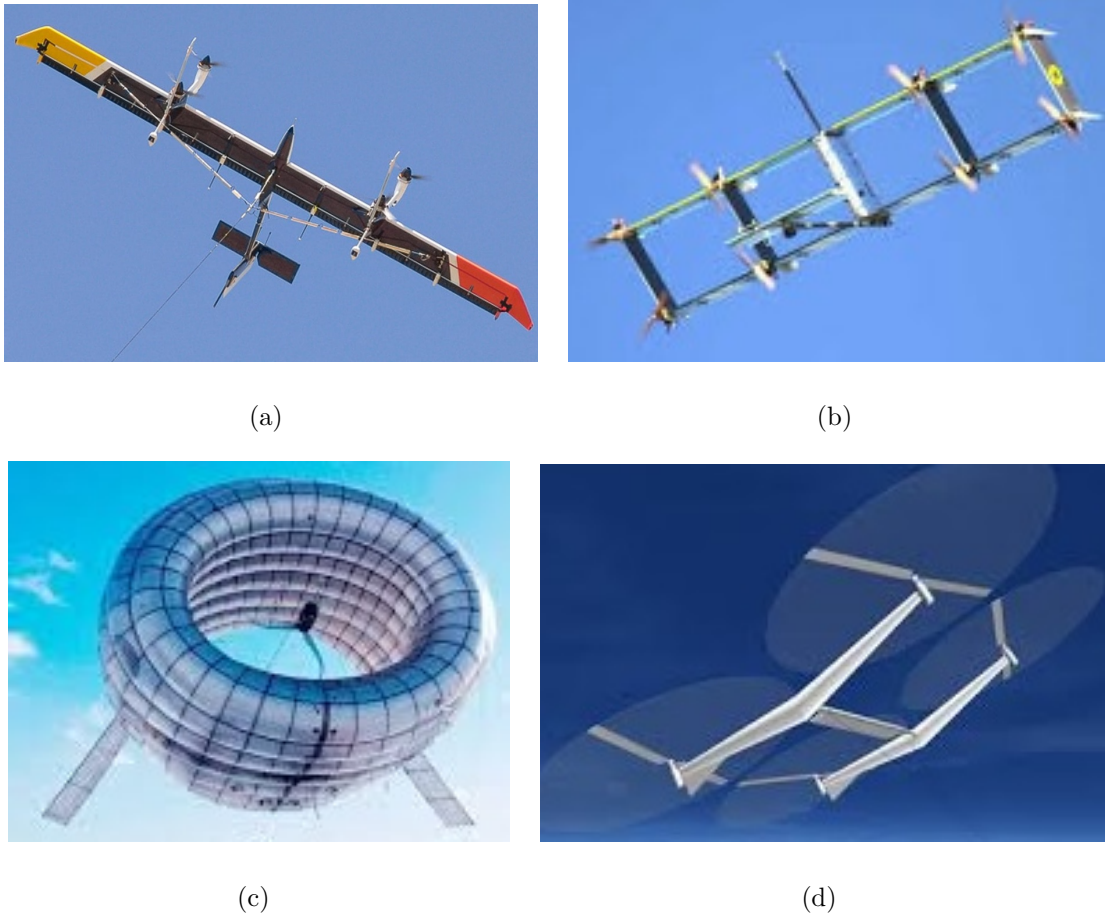


Figure 1.3: Fly-Gen configuration for airborne wind energy devices. a) A tethered flight of special gliders, design by Makani Power [8]. b) Flight with multiple wings, design by Joby Energy [9]. c) Aerodynamically shaped aerostats filled with lighter-than-air gas, design by Altaeros Energies [10]. d) Rotor thrust flying with the same turbines used for electrical power generation, design by Sky WindPower [11].

The Fly-Gen configuration is used for underwater kite systems to obtain energy from

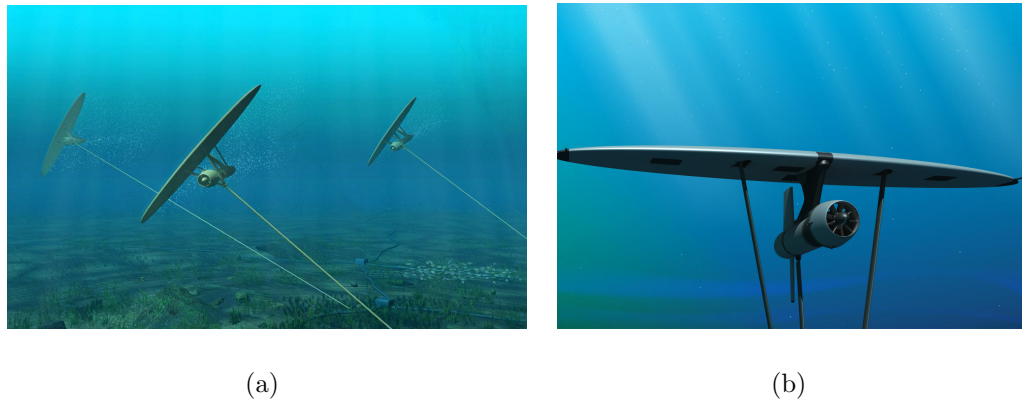
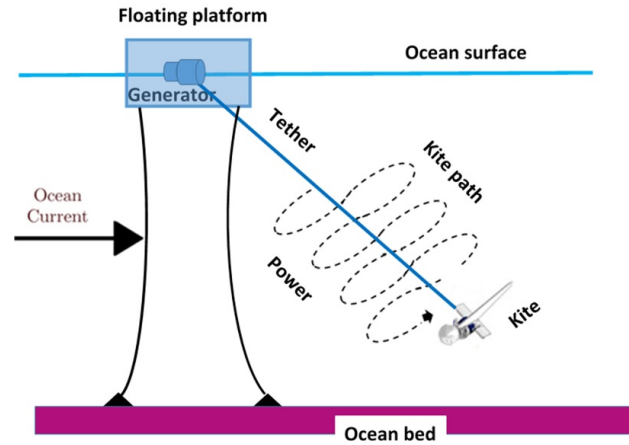


Figure 1.4: Fly-Gen configuration for underwater kite systems by Minesto UK, Ltd [12].

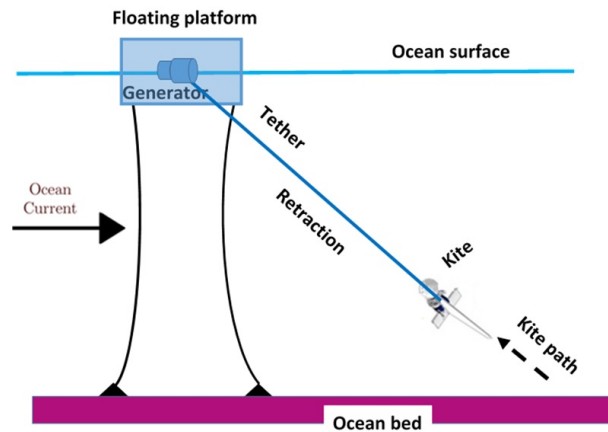
ocean currents as shown in Fig. 1.4. In Fly-Gen configuration the length of tethers do not extend or retract, therefore, simpler controller can be employed. The kite is controlled to move in a circular or figure-8 shapes motion with a constant tether length. In this concept, the risk of damage during a kite crash, due to decreasing the current speed below minimum values required to sustain flight, is high. Moreover, in order to lower the losses during the transmission, large transformers are required to increase the voltages which leads to increase the weight and size of TUSK systems. Since it is not always practical to use large transformers, the voltage of the power coming down the tethers is lower than the optimal value for the tether length distance between the kite and a step-up transformer on the ground [4].

In another concept TUSK systems which is studied in this dissertation, a tether attached to the kite is wound around a generator spool on a fixed or floating platform in an ocean current. The electrical energy is obtained using the hydrodynamic forces imposed on the kite that are transmitted from the rigid underwater kite to the generator through the tether shown in Fig. 1.5. It is similar to the Ground-gen configuration

in airborne wind kite systems.



(a) The power is generated in this phase while the length of the tether increases.



(b) The power is consumed during the retraction phase.

Figure 1.5: Ground-Gen configuration of TUSK systems.

Power is obtained with a two-phase cycle, in which electrical energy is produced in a reel-out (power) phase, and a smaller amount of energy is consumed during reel-in (retraction) phase. While the kite moves down stream in a circular or figure-8 motion during a reel-out phase as shown in Fig. 1.5(a), the tether spools out and rotates

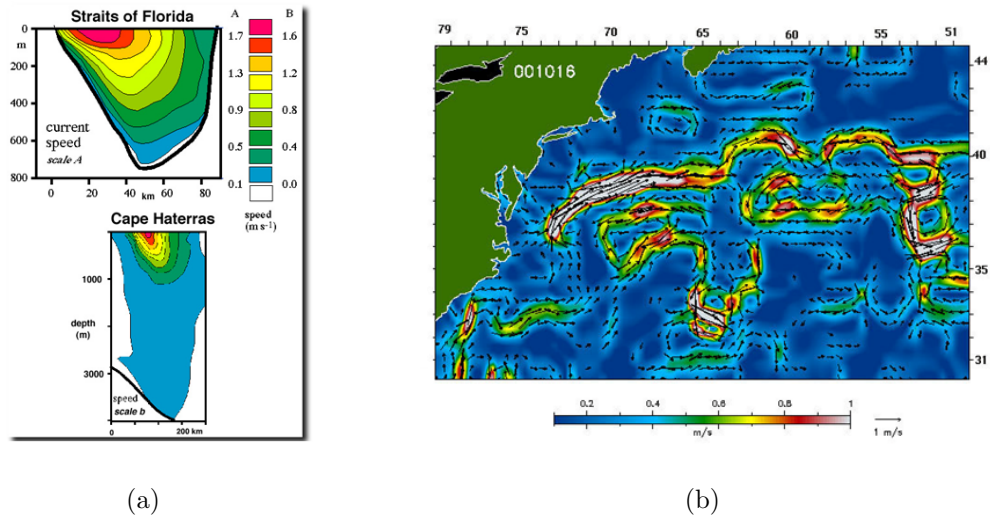


Figure 1.6: Ocean current velocity around gulf stream. © Delft Institute for Earth Oriented Space Research

the generator shaft. When a maximum tether length is reached, the kite pitch, roll and yaw angles are adjusted to reduce the hydrodynamic forces on the kite during a subsequent reel-in phase. Since the hydrodynamic forces during the reel-out phase are larger compared to the reel-in phase, a positive net power is obtained during a power-retraction cycle. The net power is guaranteed by a control system that adjusts the hydrodynamic forces imposed on the kite [13] and the flight path [14] to enhance the power production in the power phase and reduce the power consumption in the retraction phase. Moreover, TUSK systems are preferred to implement near the ocean surfaces due to higher velocity at the ocean surface (Fig. 1.6) and its effect on the power generation. Since the generation equipment is placed on the floating platform in the Ground-Gen configuration, the risk of damage from a kite crash is lower than the Fly-Gen configuration.

The proposed TUSK system can extract significant power from an ocean current. Loyd [15] presented the maximum theoretical power from a constant flowing current

during the power phase of a kite by:

$$P_{theo.} = \frac{2}{27}\rho AV^3 C_R \left(\frac{C_R}{C_d}\right)^2, \quad (1.1)$$

where ρ is the water density, V is the current velocity, A is the area of the kite, C_R is the resultant kite coefficient, and C_d is the total drag coefficient including the kite and the tether. A kite with the area of $A = 24 \text{ m}^2$, and average mean aerodynamic coefficients of $C_R = 0.7$ and $C_d = 0.1$ over the power phase, moving around the ocean surface with a speed of $V = 1 \text{ m/s}$, with a tether unwinding at an average longitudinal velocity of $V_t = 0.33 \text{ m/s}$ would theoretically produce power around 60,000 Watt (60 KW). System inefficiencies would lower the power, however the power calculation is also conservative in several aspects, for example larger kite areas could be achieved. In order to calculate a power coefficient for comparison to the Betz limit ($C_p = 16/27 = 59\%$), the area swept by the kite ($A_{cross-current}$) during an assumed cross-current motion through a 15° arc at tether length $L_t = 100 \text{ m}$, with a wingspan $b = 8 \text{ m}$, would be $A_{cross-current} = 240 \text{ m}^2$ which is then used to find:

$$C_P = \frac{P_{theo.}}{\frac{1}{2}\rho A_{cross-current} V_c^3}. \quad (1.2)$$

Table 1.1 presents typical values for key performance and design parameters for TUSK and conventional marine hydro-kinetic (MHK) turbine systems. It presents maximum theoretical power output for both systems. Typical power coefficients for both systems is also given confirming that they do not violate the Betz limit. The theoretical power is calculated based on Eq. 1.1 for TUSK systems while for a fixed marine turbine is obtained by:

$$P = \frac{1}{2}C_p\rho AV_c^3. \quad (1.3)$$

Here, for the fixed marine turbine, C_p is considered as Betz limit (16/27). It should be noted that the theoretical power for TUSK systems is considered just during the

Table 1.1: Comparison of TUSK and fixed marine turbine systems.

Parameter	TUSK Systems	Fixed Marine Turbine
Area (m^2)	24	24
Density (kg/m^3)	1000	1000
Velocity (m/s)	1.0	1.0
C_R	0.70	—
C_d	0.10	—
Theoretical Power (Watt)	$\sim 60,000$	~ 7000
Cross-current Area (m^2)	240	24
Power Coefficient (C_P)	$0.47 < 0.59$	0.59

power phase, while the power required to retract the TUSK systems will reduce the net power output. This reduction can be estimated by noting that the most efficient AWE systems currently achieve peak power output of about 80%, and average power output of about 40% of the maximum theoretical power [11].

Another way to consider the increased power output of TUSK systems follows the observation that the outer portion of a fix turbine blade contributes the majority of the power produced by the turbine (Fig. 1.7). Therefore, the inner portions of the blade, hub, and tower which comprise the majority of the weight and complexity of the turbine, generate a minor part of the power produced by the turbine. In TUSK systems, the inner portion of the blade, hub and tower of conventional marine turbines are replaced with a single lightweight tether. This leads to an increased power/weight ratio for TUSK systems [11]. In the Ground-Gen configuration, a discontinuous power output, with alternating time-periods is achieved but optimal design and deployment could significantly reduce the size of electrical storage needed [5].

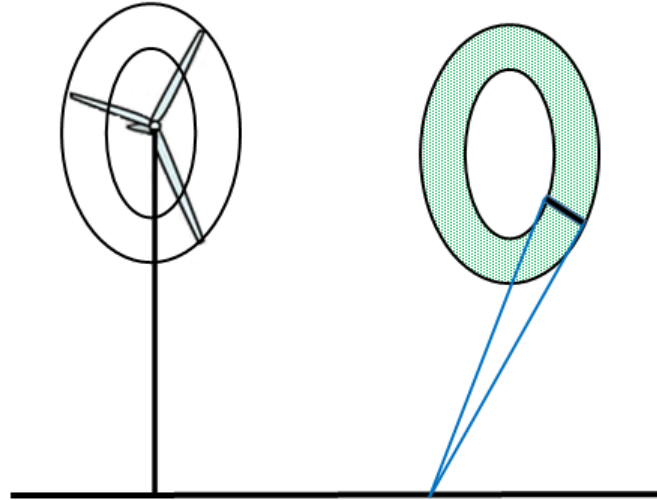


Figure 1.7: The outer portion of turbine blades compared to the kite in the TUSK systems.

1.1 Literature Review

Underwater kites were first proposed by Landberg [3] in 2007. Minesto UK Ltd, founded in 2007, is developing a system it calls Deep Green. That system uses an underwater wing with upturned tips, a kite-mounted turbine, and a tether that runs to the ocean floor as shown in Fig. 1.4. Moodley et al. [1] conducted a preliminary economic analysis on the feasibility of the Minesto Deep Green technology, which uses undersea kites to extract tidal and ocean current energy, for the Agulhas Current near South Africa. They found Deep Green to be more cost-effective than other hydro kinetic technologies. Lazakis et al. [16] have also conducted a risk assessment of installation and maintenance activities for the Minesto Deep Green system, and Lazakis et al. [16,17] have investigated operational and maintenance parameters that affect system cost. Minesto has conducted long-term sea trials of quarter-scale kites, which have been underway off the coast of Northern Ireland since 2010. At the same

time, researchers at the University of Strathclyde in the United Kingdom, working with Minesto, have developed a kite motion simulator that includes hydrodynamic force, tether, buoyancy, and added mass models to aid Deep Green technology development [18]. Minesto's next step is to implement a grid-connected, 500 kW per device off the coast of Wales in 2017. Minesto UK Ltd. has advanced their research and development to the sea-trial stage, but to the best of the author's knowledge have published limited technical analyses of their system in the archival literature. A Canadian company, HydroRun Technologies Ltd. [19], started developing its Free-stream Glider technology for use in river currents in 2012. Its underwater wing resembles a glider, complete with rudders and elevators on tail surfaces behind the wing. The glider is tethered to a generator on a buoy on the river surface. After successfully testing a 40 kW pilot plant, HydroRun suspended operations in 2015 due to some changes in the economics of the energy industry in Canada. Moreover, SeaCurrent is a start-up created to make electricity generated from tidal currents affordable and internationally accessible. To achieve this, the company develops an innovative system using an underwater kite that is ecologically friendly [20]. They use two kites (one creates power as the other retracts), to extract the energy which is anchored to an ocean bottom as shown in Fig. 1.8. Also, Japan's New Energy and Industrial Technology Development Organization (NEDO) with Tokyo - IHI Corporation and Toshiba Corporation has launched, a research program that will investigate current power by floating kite turbines in the Kuroshio Current [21]. This system consists of a power generation device with two turbines whose blades rotate in opposite directions to each other. Although the kite turbines do not have a cross-current motion, it can be installed at great depths as it is operated by mooring it to the ocean floor and allowed to float in the ocean current like a kite [21].

Olinger and Wang have published some of the first technical analysis of TUSK sys-

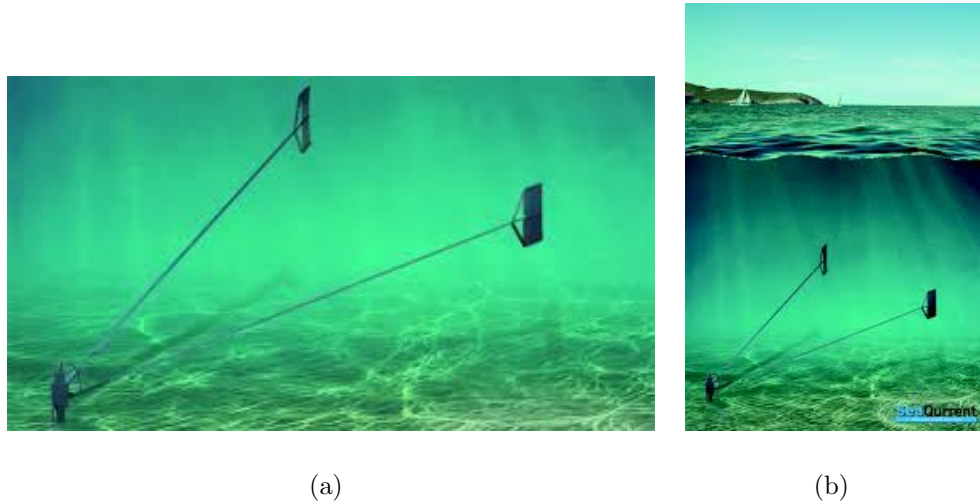


Figure 1.8: Underwater kite systems design by SeaQurrent company [20].

tems in the archived literature [22,23]. Initial design studies including power estimates have been conducted. A six degree of freedom TUSK model was also used to simulate TUSK kite trajectories to verify these power estimates. Wang and Olinger [23] extended those simulations by incorporating improved hydrodynamic models for the kite and tether, and adding a detailed cavitation model. Also, Li et al. [24,25] studied the dynamics of TUSK system and proposed a passivity controller to control the trajectory of the kite. The studies cited above [18,22–25] that develop models for TUSK systems are differential equation based, and use relatively simple (linear, inviscid) models to obtain kite lift and drag forces.

While TUSK systems have rarely been investigated, airborne kite systems have been studied extensively. Using kites to extract wind energy was first studied by Loyd [15]. He investigated the concept of using crosswind kite to harness high altitude wind energy. He calculated that wind turbines in a crosswind motion could produce more power than equivalent turbines placed on the ground. He also patented his idea in 1981 [26]. Airborne wind energy systems (AWE) inspired by Loyd’s work, have

been extensively studied [13, 14, 27, 28] as an alternative to wind turbines. Moreover [29–32] have established the feasibility of AWE systems and advanced the ability to model the dynamics and design of tethered kite components such as aerodynamic kites, high strength tether and control system of the kite. Analysis and design of autonomous kite trajectory controllers for AWE systems, have been recently studied in Archer et al. [33], Williams et al. [13], Aragofov and Silvennoinen [32], and Erhard and Strauch [30]. In addition, the availability of global wind resources has been investigated by many research centers and companies:

KiteGen Research: KiteGen Research (KGR) is one of the first companies to test a Ground-Gen configuration prototype in Italy [34]. They control the kite (aircraft) based on two power-tethers from a control station on the ground [35, 36]. They successfully demonstrated the first prototype in 2006 [35, 37]. KiteGen Research focused on, “KiteGen Stem”, a new generator that can generate 3 MW, and patented in 2008 [38, 39]. They retracted the kite with a side-slip maneuver which aims to consume minimum energy during this phase [40]. KiteGen Research is developing special aerodynamic tethers [41] in order to enhance the system performances which is patented in 2010. Moreover, they are going to use the stem technology for offshore airborne wind energy devices [42] because offshore AWE devices are very promising [43].

Kitenergy: This is another Italian company where the similar control scheme is used to control the kite as KiteGen Research have done [44, 45]. While they can generate 60 kW of rated power [46], they submitted another patent in Ground-Gen configuration of AWE devices [47].

SkySails Power: This company was founded in Germany where they developed a wind propulsion system based on kites for cargo vessels [48, 49]. They control the kite angle

of attack using a single tether and a control pod [50]. They also submitted a patent for a recovery system [49] designed for packing the kite in a storage compartment [51].

TwingTec: Twingtec is a Swiss company that is producing a 100 kW Ground-Gen configuration AWE system. They are developing a glider with embedded rotors which can take-off and land automatically. They intend to use a generator in a 20-foot container to target off-grid and remote markets which would supply continuous and reliable electrical power due to the integration with conventional diesel generators [5, 52].

TU Delft: One of the first research on AWE devices was started at Delft university by Professor Ockels, in 1996 [27]. They collaborate with Karlsruhe University of Applied Sciences to develop and test a 20 kW experimental pumping kite generator [53] in which the wing demonstrated fully automatic operation [54]. Delf University also tested a new alternative device for controlling the kite in 2013, while the concept was too complex and too sensitive to deviations from nominal operation [55].

Ampyx Power: The Dutch Ampyx Power was the first company that proposed the pumping glider generator [56,57]. They currently are developing “PowerPlanes” which are controlled automatically by state of the art avionics [58]. They can generate 6 kW with peaks of over 15 kW power using a glider flight which is fully autonomous during normal operations.

EnerKite: This is another German company that test and develop the portable pumping kite generator. They can generate a continuous power of 30 kW in which they use a Ground-Gen configuration of AWE devices and is controlled by three tethers [5]. Their goal is to achieve 100 kW power using an autonomous launch and landing system for semi-rigid wings [59]

Windlift: Windlift was founded in US and have developed the Ground-Gen concept AWE devices similar to that of Enerkite. They tested a prototype which achieved 12 kW rated of power [60]. They intended to sell their products to the military [5].

KU Leuven: KU started their research and investigation on AWE devices in 2006. They tested and developed a tether glider with a novel procedure [61]. They are currently developing a larger experimental test set-up, with a 10 kW rate of power production.

SwissKitePower: SwissKitePower was founded in Swiss in 2009 which involved four laboratories from different universities: FHNW, EMPA, ETH, and EPFL. They tested and developed a new Ground-Gen configuration of AWE device in 2012 [62], but that project was ended in 2013. Then, one of the involved laboratories (FHNW) started to collaborate with the company TwingTec [5].

NASA Langley: NASA conducted a study on AWE devices in one of their research center, Langley, in which they developed a Ground-Gen configuration of the AWE systems. The kite is controlled by two tethers, a vision system and sensors which are located on the ground [63].

Makani Power: Makani Power company have developed and tested different prototypes of AWE devices for 9 years [8]. They tested Ground-Gen configuration with single and multiple tethers, and with soft and rigid wings [64]. They submitted different patents on tether tension sensor [65], aerodynamic cable [66] and a new idea of a bimodal flight to solve take-off and landing barriers [67]. Makani developed “M600”, a 600 kW prototype, which is working with 8 turbines and is undergoing testing [5]

Joby Energy: Joby Energy was founded in 2008 in the US and developed the Fly-Gen

configuration AWE systems. They use a multi-frame structure with embedded airfoil for airborne vehicle [9] and submitted a patent for aerodynamic tethers [68]. While the airborne vehicle is different than those of Joby Energy and Makani companies, they have similar power generation method and take-off and landing maneuvers [69, 70].

Altaeros Energies: MIT and Harvard alumni [10, 71, 72] led a Massachusetts-based business that developed and tested flying wind turbines in a stationary position. They used ring shaped aerostat with a wind turbine installed inside the ring and due to the lighter weight of generator than the air, the take-off and landing maneuvers are simplified. They only need to overcome the stability barrier in which the generator would be in the right position relative to the wind [73].

Sky Windpower: They proposed a different kind of tethered craft in which three identical rotors mounted on an airframe that is connected to a ground station by a tether with inner electrical cables [74–77]. This is the first concept of AWEs that is tested at at University of Sidney in 1986 [11]. While similar concept of Take-off and landing maneuvers are used as those of Makani’s, the electric generation operation is different. Sky Windpower went out of business in 2015.

New companies: There are many companies that have been founded recently [5, 34]. e-Kite was founded in the Netherlands in 2013. They tested a 50 kW Ground-Gen configuration that fly at the low altitude [78]. Enevate company conducted a study on TU Delft AWES systems to bring it in commercial product [5]. Kitemill, founded in Norway, where their focus is on Ground-Gen configuration AWE devices where a one tether rigid wing system with on-board actuators is used to control the kite [5]. Moreover, eWind is a US company developing the Ground-Gen configuration AWE systems with rigid wing that fly at low altitude [5].

There are other different research centers that have been conducting and studying on AWEs systems, such as University of Grenoble [79], Sussex University [80], Department of Mechanical Engineering of Rowan University [81] and Worcester Polytechnic Institute [82]. The state-of-the-art in AWE systems has been recently summarized in Ahrens et al. [34].

Due to the similarity of AWE and TUSK systems, lessons could be used from AWE to guide TUSK development. Although there are some similarities between the two classes of systems, there are distinct advantages associated with utilizing underwater kites; such as higher density of the water than air, which leads to increased power output and the stability of the ocean currents in direction and intensity compared to air wind. A detailed account of the amount of power that can be obtained with TUSK, AWE and MHK is presented in [22].

1.2 Modeling of Fluid-Solid Interaction

In order to model the interaction of the solid underwater kite with the surrounding fluid current, an immersed boundary (IB) method is used. There are different methods have been proposed to capture the fluid-solid interaction, such as body conformal [83–85], fictitious domain [86], and immersed boundary methods [87–89]. In the body conformal mesh method, the computational domain includes only the fluid and the mesh conforms to the solid geometry. Since this method is complex, using an unstructured grid is inevitable. Also, due to the motion of the solid object, the computational domain is changing in time, and re-meshing is required [90]. Moreover, the flow quantities, including velocity and pressure, have to be mapped from the previous to the new time step, and this mapping can be computationally intensive [83]. The

immersed boundary and the fictitious-domain method are based on relatively similar ideas, with the immersed boundary term usually used when the underlying fluid solver is a finite volume method, and the fictitious-domain term used when the flow solver is based on finite elements [91]. The immersed boundary method was introduced by Peskin [87] to model cardiac mechanics. In this method, a body force is added to the Navier-Stokes equations along the solid-fluid interface. The Navier-Stokes equations are solved on the entire computational domain and interpolated fluid velocities inside the solid are used to determine the motion of the solid [92]. The computational cost of this method is very low. The efficiency of the immersed boundary method, used in this thesis, is well-established [93–95].

1.3 Goals and Contributions

This dissertation seeks to develop numerical simulations to model the 3D kite and tether dynamics of a TUSK system using a moving computational domain method. Nonlinear effects are captured in the present study since the full Navier-Stokes equations are solved for the ocean current flow field surrounding the underwater kite. The computational tool includes a flow solver to solve the flow equations where a two-step method in the finite-volume context is used coupled with Open Multi-Processing (OpenMP) [96]. The immersed boundary method [97] is incorporated to simulate the interaction of the kite with the flow. Since TUSK system kites generally fly in cross-current paths, a PID controller is used to control the trajectory of the kite during the cross current motion of the kite. Although the focus of this dissertation is numerical modeling of TUSK systems in 3D, 2D simulations have been performed as a preliminary step in which the kite geometric and effective angles of attack are

controlled by changing the length of tethers. The numerical power output from a simple kite moving in two-dimensional motion is verified against theoretical results from Loyd [15]. Also, the effect of varying different parameters on the power output of 2D TUSK systems is studied. Computational run time limitations of the numerical simulation of 3D kite trajectory occur if a fixed computational domain is used. Therefore, a moving numerical domain is used in the computational methods in this thesis in order to decrease the computational run-time. In order to capture boundary layer and viscous drag at the kite interface, a very fine grid resolution is required. This leads to increase the computational run-time drastically in 3D simulations. Therefore, the slip condition is applied at the kite interface to accurately estimate the kite drag prediction using coarse grid resolutions.

A baseline simulation study of a full-scale TUSK wing is conducted. The simulation captures the cross-current motions during a kite reel-out phase where the tether length increases and power is generated. During the following reel-in phase the kite motion is along the tether, and kite hydrodynamic forces are reduced so that net positive power is produced. Kite trajectories, hydrodynamic forces, vorticity contours near the kite, kite tether tension and output power are determined and analyzed. The effects of tether retraction velocity and tether drag on the underwater kite performance are also investigated.

The main contributions of this research are:

- Development of a computational tool based on the Navier-Stokes equations for accurate modeling of tethered undersea kites for power generation in ocean currents. To the best of author's knowledge, this is one of the first dedicated codes based on the Navier-Stokes equations for modeling TUSK systems.

- Baseline simulations for a full-scale TUSK wing have been performed and basic TUSK performance such as net power, hydrodynamic forces and the kite trajectory are shown. The results in 2D and 3D are compared with the theoretical data, conducted by Loyd [15] and Ahrens [34], to verify the accuracy of the numerical model.
- A moving computational domain is incorporated into the computational tool to reduce the computational run-time.
- A very fine grid resolution is required to capture boundary layer and viscous drag at the kite interface, and it increases the computational run-time in 3D simulations drastically. In order to more accurately estimate kite lift and drag forces at coarser grid resolutions, the slip condition is implemented at the kite interface.
- Grid refinement and Reynolds number independency have been studied. The accuracy of the moving numerical domain has been investigated by conducting different simulations and comparing the results with fixed computational domain simulations.
- The effect of varying tether drag and tether retraction velocity in 3D simulations, and tether velocity during the power phase and inlet current velocity in 2D simulations on the performance of TUSK systems is investigated.
- Different control schemes are implemented to control the desired trajectory and kite geometric angles. A PID controller in the 3D simulations is utilized to control the kite to have a cross flow motion while the kite angle of attack is controlled by the length of tethers in 2D simulations.

- The computational code is parallelized using Open MP to reduce the computational run-time.

This thesis is organized as follows: Chapter 2 reviews the governing equations and the boundary conditions of incompressible flows. Then, the details of the numerical methods employed in this work are explained. The independency of the numerical results to grid resolution and Reynold number are studied in chapter 3. Moreover, in this section different simulations have been conducted to verify the accuracy of the moving computational domain method. The effect of slip and no-slip conditions at the kite interface, on the kite lift and drag forces is also studied in this section. Chapter 4 reports the interaction of the tethered undersea kite systems with the ocean current. Results from baseline simulations of a full-scale kite-tether wing are presented in this section including predicted kite hydrodynamic forces, trajectory of the kite, and power generation values. Moreover, the effects of varying different parameters, including tether velocity during the power phase, inlet current velocity, the tether velocity during the retraction phase and the tether drag on the performance of TUSK systems are presented. Conclusions along with recommendations for future work are presented in chapter 5.

Chapter 2

Governing Equations and Numerical Methods

In this chapter the governing equations and corresponding boundary conditions for the interaction of a tethered undersea kite with an ocean current are presented. Then, it provides details on the numerical model of the flow solver, including the two-step projection method and corresponding discretization of the pressure Poisson problem. Also, the numerical models to capture the fluid-solid interaction, kite controller schemes, tethers modeling, the kite lift and drag calculation, moving numerical domain, the slip method implemented on the kite interface and the tether drag modeling are presented.

2.1 Mathematical Formulation

A numerical method is developed to study the behavior of a rigid underwater kite which is attached by a tether to a fixed structure. A flow solver in a rectangular domain with a regular structured grid is implemented. The interaction of the rigid kite with an ocean current is captured by the immersed boundary method, and Hook's law with the effect of the tether damping included, is used to model the tether tension. Moreover, controller schemes which controls the angles of the kite are utilized to

achieve a desired trajectory. The governing equations for unsteady, incompressible fluid flow are the Navier-Stokes equations.

$$\nabla \cdot \vec{V} = 0 \quad (2.1)$$

$$\frac{\partial(\rho\vec{V})}{\partial t} + \nabla \cdot (\rho\vec{V}\vec{V}) = -\nabla p + \nabla \cdot \tau + \vec{F}_b + \vec{F}_t + \vec{F}_{so}. \quad (2.2)$$

Here, \vec{V} denotes the velocity vector, ρ the density, p the pressure. \vec{F}_b represents any body forces such as gravity, and \vec{F}_t and \vec{F}_{so} represent the tether tension and fluid-solid interaction force, respectively. Also τ is the stress tensor expressed as:

$$\tau = \mu[(\nabla\vec{V}) + (\nabla\vec{V})^T], \quad (2.3)$$

where μ is the dynamic viscosity. The full Navier-Stokes equations are used, instead of the potential flow or Euler equations to retain rotational effects (such as wake vortex shedding) and the stabilizing effect of viscosity in numerical simulations.

A NACA-0012 airfoil is used for the cross section shape of the kite using Eq. 2.4.

$$\begin{aligned} \frac{Z_{th}}{c} = 5t(\{ & 0.2969\sqrt{\frac{x}{c}} - 0.1260(\frac{x}{c}) - 0.3516(\frac{x}{c})^2 \\ & + 0.2843(\frac{x}{c})^3 - 0.1015(\frac{x}{c})^4\}). \end{aligned} \quad (2.4)$$

where t is the maximum thickness as a fraction of the chord, c is the chord length, x is the position along the chord and Z_{th} is the airfoil half thickness [98]. The rectangular wing planform with an aspect ratio (span/chord) of 8/3 is used in the three dimensional computational simulations. The kite is represented by a scalar function ψ :

$$\psi(\vec{x}) = \begin{cases} 1, & \vec{x} \in \text{solid} \\ 0, & \vec{x} \notin \text{solid} \end{cases} \quad (2.5)$$

where ψ is defined by the

$$\psi = \frac{\text{Volume of occupied region by solid}}{\text{Cell volume}} \quad (2.6)$$

The marker function transitions smoothly near the kite interface by [99]:

$$\psi = 0.5 + 0.5 \frac{(Z - Z_{th})^3 + 1.5\epsilon^2(Z - Z_{th})}{((Z - Z_{th})^2 + \epsilon^2)^{1.5}}, \quad (2.7)$$

where ϵ can be adjusted to control the thickness of the transition zone. $Z - Z_{th}$, is the distance between the local grid position to the kite interface. The effect of ψ can be seen in the material properties which are defined as:

$$\rho = \psi\rho_{so} + (1 - \psi)\rho_l. \quad (2.8)$$

Where, ρ_{so} and ρ_l are solid and liquid density, respectively.

2.2 Boundary Conditions

Boundary conditions for the computational domain are specified as follows. At the upstream end of the domain, a constant velocity is specified for the current flow and the fluid is allowed to flow out at the downstream of the domain. The pressure and velocity gradient at the downstream end of the domain is assumed to be zero [100]:

$$\vec{\nabla}p \cdot \hat{n}_\perp = 0. \quad (2.9)$$

$$\vec{\nabla}\vec{V} \cdot \hat{n}_\perp = 0. \quad (2.10)$$

Therefore, mass conservation is satisfied over the entire numerical domain at every time step. Full slip boundary conditions are imposed on all other sides of the numerical domain. Free slip and no penetration are satisfied simultaneously by

$$\frac{\partial(\vec{V} \cdot \hat{t}_s)}{\partial n_s} = 0. \quad (2.11)$$

While in order to implement the no-slip boundary condition we have:

$$\vec{V} \cdot \hat{n}_\perp = 0, \quad \vec{V} \cdot \hat{t}_\perp = 0. \quad (2.12)$$

Here, \hat{n}_\perp and \hat{t}_\perp are the normal and tangential vectors on the surface of the boundary condition. Also, a steady uniform velocity is considered as an inlet boundary condition.

2.3 Two-step Projection Method

For the discretization of the governing equations in our computational method, an explicit second-order predictor-corrector method on a staggered grid has been used in which the continuity and momentum equations are solved in two steps as shown below:

$$\frac{\rho^{n+1}\vec{V}^* - \rho^n\vec{V}^n}{\Delta t} = -\nabla \cdot (\rho\vec{V}\vec{V})^n + \nabla \cdot (\mu(\nabla\vec{V} + \nabla^T\vec{V}))^n + \vec{F}_B^n + \vec{F}_{so}^n \quad (2.13)$$

$$\frac{\rho^{n+1}\vec{V}^{n+1} - \rho^{n+1}\vec{V}^*}{\Delta t} = -\nabla p^{n+1}. \quad (2.14)$$

Here the superscripts n and $n+1$ denote the current and next time steps, respectively, and \vec{V}^* represents an intermediate velocity. A second-order essentially non-oscillatory (ENO) method and a simple second order centered difference approximation were used to discretized the advection and viscous terms, respectively.

By applying the continuity on Eq. 2.14 the Poisson equation is obtained:

$$-\nabla^2 p^{n+1} = \frac{1}{\Delta t} \nabla \cdot (-\rho^{n+1}\vec{V}^*). \quad (2.15)$$

p^{n+1} is obtained by solving Eq. 2.15 iteratively using Successive Over-relaxation (SOR) solver. V^{n+1} is then evaluated via Eq. 2.14.

Solving Poisson's equation is very computationally intensive. To make our simulation run faster, OpenMP acceleration is utilized. The OpenMP is explained in detail in [96].

2.4 Fluid-solid Interaction

Since the governing equations for fluid flow are discretized in an Eulerian form, then the immersed boundary method is coupled with the flow solver in the computational method to simulate the interaction of a rigid kite with a fluid flow. The governing equations for the fluid are solved in the entire computational domain including in the region occupied by the kite (solid object). Therefore, it is not needed to solve any additional equation for the solid object in this step. The numerical algorithm stays the same irrespective of the nature of fluid flow: laminar, or turbulent, Newtonian, or non-Newtonian. Since the kite is considered as a fluid and the Navier-Stokes equations are solved inside it, the velocity field inside the kite obtained from the flow solver does not satisfy the kite rigidity condition. To enforce rigidity of the kite and correct the velocity, the kite velocity is decomposed into two components, translational and rotational, which are calculated by taking an average over the entire kite domain:

$$M_{so}\vec{V}_{so} = \int_{solid-zone} \rho\vec{V} dv \quad (2.16)$$

$$I_{so}\vec{\omega}_{so} = \int_{solid-zone} \vec{r} \times \rho\vec{V} dv \quad (2.17)$$

where M_{so} , I_{so} are the mass and moment of inertia, respectively, of the kite. v is the volume and \vec{r} denotes position vector relative to the center of mass of the kite.

The moment of inertia tensor components with respect to center of mass,

$$\begin{bmatrix} I_{xx} & -I_{xy} & -I_{xz} \\ -I_{yx} & I_{yy} & -I_{yz} \\ -I_{zx} & -I_{zy} & I_{zz} \end{bmatrix} \quad (2.18)$$

are calculated by integration on the part of the computational domain that includes the kite.

After obtaining the translational and angular center of mass velocities, the kite velocity is thus calculated by taking a summation of the two components,

$$\vec{V}_{kite} = \vec{V}_{so} + \vec{\omega}_{so} \times \vec{r} \quad (2.19)$$

Note that the velocity in the kite proposed by the flow solver was corrected (averaged) to enforce the kite rigidity.

Since the original velocity field which is obtained by solving Poisson's equation is divergence free, the new velocity field given by Eq. 2.19 should be divergence free everywhere. Sometimes that is not exactly true at the kite interface and a few iteration are performed to reach the divergence free velocity [99].

The difference between the proposed and averaged velocity fields determines the body force \vec{F}_{so} , which is applied only on the kite (solid) body as shown in Eq. 2.20.

$$\vec{F}_{so} = \frac{\rho}{\Delta t} (\vec{V}_{kite}^{n+1} - \vec{V}^{n+1}) \quad (2.20)$$

where \vec{V}^{n+1} and \vec{V}_{kite}^{n+1} are the velocity of the kite before and after averaging, respectively. For more information about the coupling the Navier-Stokes equations with fluid-solid interaction force see [86, 97, 101]

2.5 Tether Modeling

Various support structure and tether attachment concepts are being considered for TUSK systems, including tether attachment to the ocean floor; floating or fixed structures at the ocean surface; or submerged buoyant structures. While each of these has its own advantages and drawbacks, in this work for simplicity we assume a fixed support structure for tether attachment at the ocean surface. To model the tension

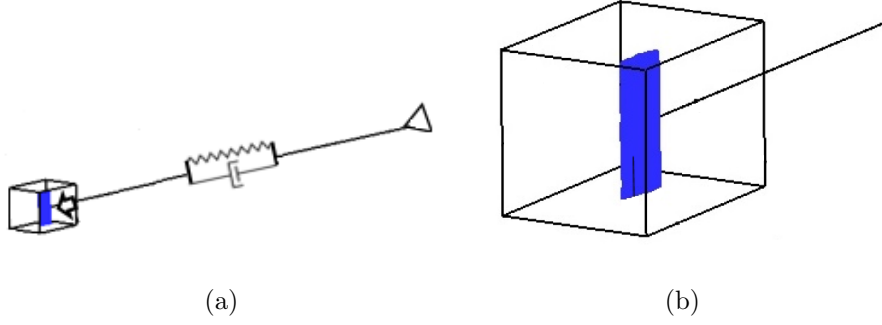


Figure 2.1: a) Schematic diagram of the kite-tether system in which the attachment point is outside of the computational domain. b) zoom-in view.

forces in the elastic tethers that connect the kite to the fixed structure at the ocean surface, a simple Hooke's law is used while damping effect is also considered.

$$\vec{F}_t = K(\max(L_{act.}, L_i) - L_i) + C_{damp} \vec{V} \frac{\max(L_{act.}, L_i) - L_i}{L_{act.} - L_i}. \quad (2.21)$$

Here, K and C_{damp} are the tether stiffness and damping coefficient, respectively. Also, $L_{act.}$ is the actual length of the tether, and L_i is the rest length of the tether. In the baseline simulation, a single tether is connected from the kite center of mass to a fixed point far from the kite. The tether can go slack if the tether tension goes to zero, however, positive tether tension is maintained during a simulation. Then, the forces from the tethers are added as a body force to Eq. 2.2. The computational cost was reduced by placing the fixed tether attachment point outside of the computational domain which leads to reduce the domain size as shown in Fig. 2.1.

2.6 Control Scheme

In order to achieve the desired kite trajectory, a proportional-integral-derivative (PID) controller is used to control the kites pitch, roll and yaw angles to achieve a desirable kite trajectory. In the controller, an error is defined based on the difference between

the actual and trim angles of the kite, and the error is minimized over time by adjustment of control moments applied on the kite. The control moments are calculated by:

$$\vec{F}_M = K_p(\alpha_t - \alpha_a) + K_i \int_0^t (\alpha_t - \alpha_a) dt + K_d \frac{d(\alpha_t - \alpha_a)}{dt}. \quad (2.22)$$

where \vec{F}_M is the applied moment, α represents pitch, roll and yaw angles. The subscripts t and a denote the trim and actual angles, and K_p , K_i , and K_d , denote the coefficients for the proportional, integral, and derivative terms of PID controller, respectively. The kite trim angles were varied over multiple simulation runs to identify a baseline simulation case with the highest achievable net power production. Application of more complex kite control schemes [31, 102] could be considered as a future work.

Moreover, as a preliminary step, the unstretched tether lengths of the two straight-line tethers (between a kite control unit and the kite) are specified as an input control command in order to control the geometric angle of attack of the kite in 2D simulations as shown in Fig. 2.2. A periodic triangular wave shape is prescribed on both tether unstretched lengths for this purpose. Fig. 2.2 shows that the unstretched (input) which has a small difference with the actual (output) tether lengths due to fairly large tether spring stiffnesses.

2.7 Numerical Algorithm

The overall numerical algorithm is shown in Fig 2.3. The outer loop is the integration in time and the second loop is the iteration where the kite is coupled with the Navier-Stokes solver. Each iteration includes predicting the kite motion with the Navier-

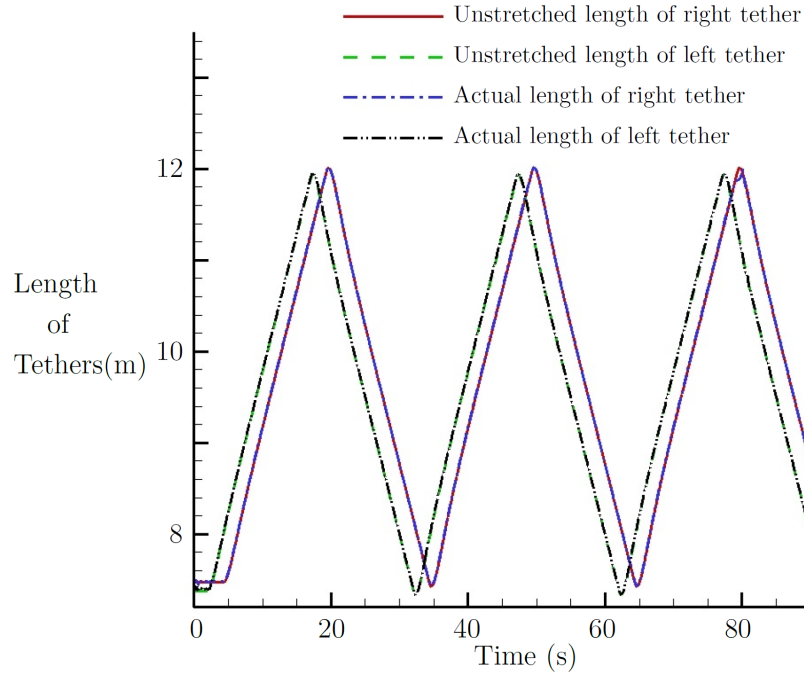


Figure 2.2: Unstretched and actual tether lengths vs time.

Stokes equations and correction of the prediction by linear and angular momentum conservation (Eq. 2.16 and Eq. 2.17). At the beginning of each iteration, the values from the previous time step, such as position, velocity and pressure are assumed as the initial guess. Then the density and viscosity at every grid point in the computational domain, including inside the kite, are assigned, based on the scalar function of the kite (step 2). Momentum equation is solved in step 3, and the velocity and the pressure in the whole domain at the new time level are found. After that, the kite position is updated and used in the next step to update the solid scalar function. In step 6, the kite position the linear and angular velocity of the kite are calculated, based on the conservation of linear and angular momentum. These two values are used to correct the velocity found by solving the Navier-Stokes equations in step 7 and then used for tracking the solid interface. Convergence is reached when the values

calculated in steps 3 to 7 do not change. In fixed numerical domain simulations (i.e. 2D simulations), once the solution has converged, the parameters such as velocity and location and solid scalar function are assigned as the new guess and start the procedure again. While in the 3D simulations, the moving computational domain is used, in which the boundary of the computational tool is updated based on the movement of the kite in x, y and z directions (h, g, and k), and then we go to the next time step. The numerical model is solved in a second order in time, but because of simplicity only the first order version in Figure 2.3 is shown. In order to reach the convergence a few iteration (one or two) is required for the inner loop after the initial time steps. While for the initial time steps, we usually require around 10 iterations for convergence.

The simulations have been conducted on the Linux servers supported by Worcester Polytechnic Institute Computational Center. Single Intel(R) Xenon(R) Processor X5690 with 3.47Ghz Clock speed has been used for the simulations.

2.8 Time Step Restriction

Our computational method is constrained by two time step restrictions. The time step is restricted by viscosity, and velocity which are shown in Eqs. 2.23 and 2.24 respectively.

$$\Delta t \leq \Delta t_{vis} = \frac{\rho(\Delta x)^2}{2\mu}, \quad (2.23)$$

$$\Delta t \leq \Delta t_{CFL} = \frac{1}{3} \frac{\Delta x}{U_{max}}. \quad (2.24)$$

Because the dimensions in underwater kite systems are large enough, the surface tension effects in these devices are small.

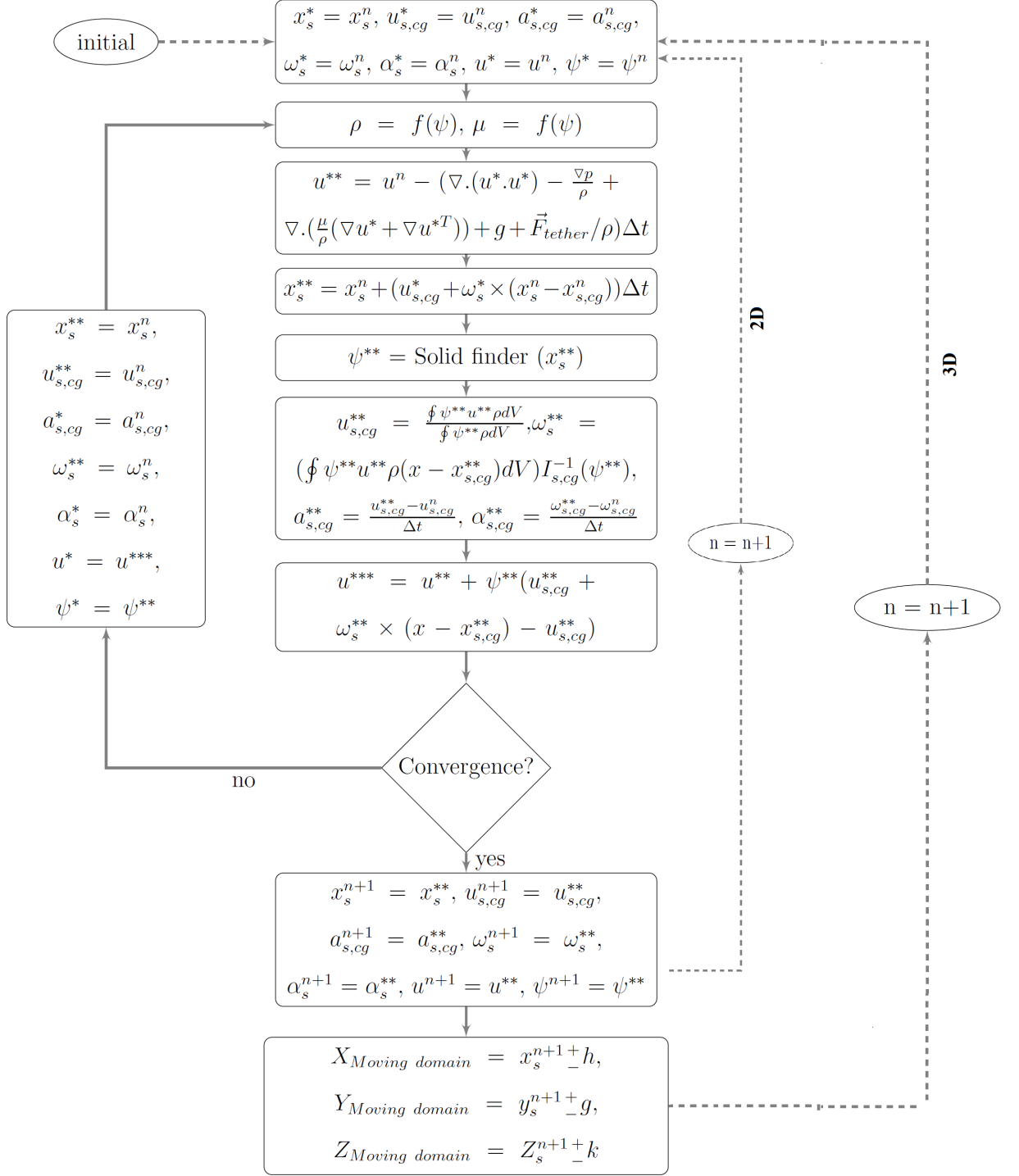


Figure 2.3: Flow chart of the algorithm for modeling of a tethered undersea kite, based on the Navier-Stokes equations.

2.9 Kite Lift and Drag Calculation

The kite lift and drag force directions are calculated using [13]:

$$L = \frac{1}{2}\rho AC_L |V_a|^2 (t_2 \sin\phi + t_3 \cos\phi), \quad (2.25)$$

$$D = \frac{1}{2}\rho AC_d |V_a|^2, \quad (2.26)$$

where V_a is the apparent kite velocity vector (resultant of current and kite velocities), A is the kite area and ϕ is defined in such a way that it represents the tilt of the lift vector relative to the tether direction [13]. The lift force, when ϕ is zero (which is considered in this study), is parallel to the vector

$$t_3 = \frac{t_2 \times V_a}{|t_2 \times V_a|}, \quad (2.27)$$

where

$$t_2 = \frac{V_a \times t_1}{|V_a \times t_1|}. \quad (2.28)$$

Here t_1 is the tangential identical vector to the tether. Therefore, the kite lift and drag forces are calculated by solving any two out of three equations as below:

$$F_x^k = (L + D)\hat{i}, \quad F_y^k = (L + D)\hat{j}, \quad F_z^k = (L + D)\hat{k}, \quad (2.29)$$

where F_x^k , F_y^k , and F_z^k are the components of the tether force in three directions. The acceleration of the kite in each time step is considered negligible in this study. It should be noted that the tether drag effect is studied in the 3D simulations while the tether weight effect is not modeled in this study.

C_L , C_d and C_R are the kite lift, drag and resultant coefficients, respectively which are calculated as follows:

$$C_L = \frac{Lift}{\frac{1}{2}\rho V^2 A}, \quad C_d = \frac{Drag}{\frac{1}{2}\rho V^2 A}, \quad C_R = \sqrt{C_L^2 + C_d^2}. \quad (2.30)$$

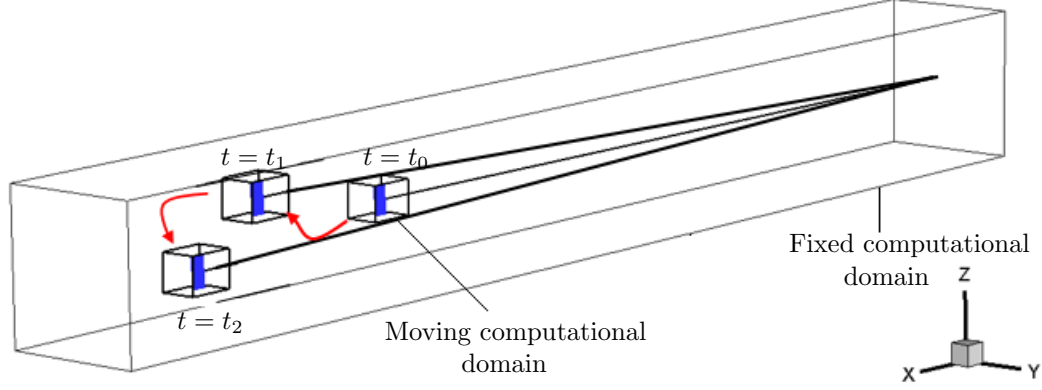


Figure 2.4: Schematic of a moving computational domain which is used in 3D baseline simulations instead of the fixed numerical domain to decrease the computational run-time.

Here, V is the magnitude of the current velocity, and A is the area of the kite to find the kite lift and drag coefficient. Moreover, it is seen in literature [13], that the apparent velocity, V_a , is used to obtain the kite lift and drag coefficients. Therefore, in this manuscript the kite lift and drag coefficients which are obtained by the apparent velocity are shown by:

$$C_{L,a} = \frac{Lift}{\frac{1}{2}\rho V_a^2 A}, \quad C_{d,a} = \frac{Drag}{\frac{1}{2}\rho V_a^2 A}, \quad C_{R,a} = \sqrt{C_{L,a}^2 + C_{d,a}^2}. \quad (2.31)$$

2.10 Moving Computational Domain

In general, a conventional approach to model a flow field around a kite when the kite travels a long distance in an arbitrary direction would require a huge three dimension computational domain. To evade this constrain of region size, a moving computational domain method is applied in this dissertation in which a numerical domain moves based on the motion of the kite as shown in Fig. 2.4.

The moving computational domain, including the embedded kite, moves in the fixed, inertia Cartesian coordinate system, so the governing equations for moving numerical domain are still Eqs. 2.1 and 2.2. Therefore, the same approach which is discussed earlier can be used to find the flow variables such as velocity and pressure. It only needs to find the proper boundary conditions of the moving computational domain. As is mentioned earlier, since all the properties such as velocity and pressure are defined with respect to the fixed inertia Cartesian coordinate system, the boundary conditions which are given in Eqs. 2.9, 2.11 are still valid for outflow, and slip wall, respectively. In this study, the boundary condition of the surrounding surfaces of the numerical domain is considered as a slip wall and the boundary condition at the end of domain is considered as an outflow. Only crucial assumption is the condition in front of the moving computational domain which has to be known as a boundary condition of the flow solver [103]. Due to the incompressibility of the ocean current flow, a constant fluid flow velocity is considered in front of the moving computational domain at every time steps. Since the motion of the computational domain based on the movements of the body in the physical space is arbitrary, then any kind of the motion of the kite can be simulated by this approach.

2.11 Slip Modeling at the Kite Interface

In this section, the effect of slip condition imposed at the kite-fluid interface is studied. In the free-slip boundaries, the kite interface is considered impermeable. Therefore, the Dirichlet condition at the kite interface $U^n = 0$ is imposed, but the boundary conditions in the tangential directions should be Neumann conditions. In order to achieve the free-slip condition, the tangential components of the stress vector at the interface are zero, since no fluid force is exerted from the fluid to the interface in these

directions. Therefore, in three dimensional simulation:

$$\begin{aligned} U^n &= 0, \\ (\tau \cdot n) \cdot s &= 0, \\ (\tau \cdot n) \cdot t &= 0. \end{aligned} \tag{2.32}$$

Here, s and t are the tangential directions to the kite interface. Also, n is the normal direction to the kite interface and is calculated by:

$$n = \frac{\nabla\psi}{|\nabla\psi|}. \tag{2.33}$$

where, ψ is the solid volume fraction.

The basic idea to apply a free-slip boundary at the kite interface is to modify the velocity components tangential (U^t , and U^s) to the kite surface which the shear stress in tangential directions vanishes. This can only be obtained by using the flow field information outside the kite. The computation of the velocity gradients at the kite interface is obtained by using the velocity at the kite interface and the vicinity cells outside of the kite as shown in Fig. 2.5. Here, T is the vicinity test-grid which is located at a distance of h normal to the kite interface. Two coordinate system, body-fixed coordinate system (x' , y') and space-fixed coordinate system (X , Y), are considered to determine the tangential flow field at the kite interface and transfer it to the space-fixed coordinate system to continue solution procedure as:

$$\vec{U}_T^b = A^T(\vec{U}_T - \vec{U}_k). \tag{2.34}$$

Where, \vec{U}_T^b is the body-reference velocity vectors at the test-grid T , while \vec{U}_T , and \vec{U}_k are the velocity vectors of the test-grid T and the kite interface velocity of the grid w , respectively. It should be noted that \vec{U}_T , and \vec{U}_k are considered in the space-fixed coordinate system, and A^T is the transpose of transformation matrix. Then

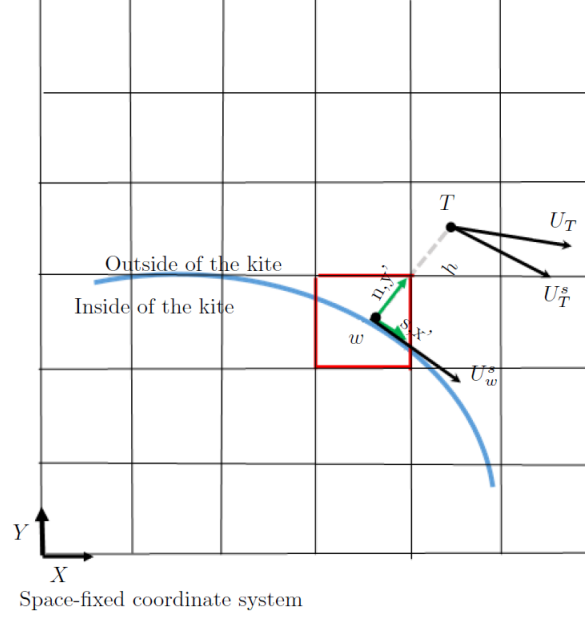


Figure 2.5: Schematic of a kite (solid object) interface and a neighbor cell with a distance h normal to the kite interface.

the desired velocity at the kite interface in tangential directions are function of the velocity at the test point to satisfy the free-slip condition.

$$\begin{aligned} U_w^s &= f(U_T^s), \\ U_w^t &= f(U_T^t). \end{aligned} \quad (2.35)$$

Here, U^s and U^t are the tangential velocity at the kite interface in three dimensional case while the normal velocity is set to zero to satisfy the impermeable condition. Since, U^s and U^t are the velocities in the body-reference frame, the desired velocity at the kite interface should be transferred into space-fixed coordinate system by:

$$\vec{U}_w = A(\vec{U}_w^b + \vec{U}_k^b). \quad (2.36)$$

Here, \vec{U}_w is the space-fixed velocity vector at the kite interface and A is the matrix transformation. After the computation of Eq. 2.36, the solution procedure continues to find the fluid-solid interaction force (Eq. 2.20) and the solution of the fluid equations

in the space-fixed coordinate system i.e. two step projection method for computation of pressure.

In order to impose the free-slip condition at the kite interface, the tangential fluid forces and shear stresses should vanish. The shear stress is computed by the derivative of the tangential velocity at the kite interface in the body Cartesian coordinate system as:

$$\tau_{x'y'} = \mu \frac{\partial u_{x'}}{\partial y'}, \quad (2.37)$$

where $\tau_{x'y'}$ is the tangential shear stress which is discretized by:

$$\tau_{x'y'}|_{y'=0} = \mu \frac{U_T^s - U_w^s}{h}. \quad (2.38)$$

Here, U_T^s is the tangential velocity at the test-grid near the kite interface and U_w^s is the tangential velocity at the kite interface. Both U_T^s and U_w^s are considered in the body-reference coordinate system. Therefore, in order to impose the free-slip condition at the kite interface we have:

$$\begin{aligned} U_s^T &= U_s^w, \\ U_t^T &= U_t^w. \end{aligned} \quad (2.39)$$

This is the standard approach to impose the free-slip at the wall interface with a curvature [104].

2.12 Tether Drag Modeling

In this work, the tether is considered as a long, rigid cylinder where one ends is connected to the fixed structure and the other end moves with the kite velocity. In order to consider the effect of the tether on the kite movement, the tether drag is added to

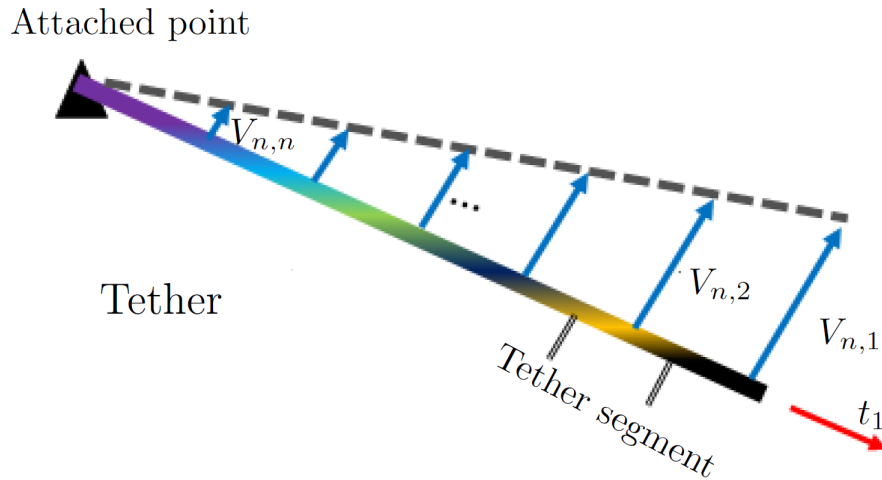


Figure 2.6: Schematic of modeling of the tether drag.

the momentum equation as a body force. The drag forces on the tether are derived by assuming that the drag tangential to the tether is negligible. Since the apparent velocity along the tether is not constant and each part of the tether is moving at a different speed, the tether is discretized into a series of element as shown in Fig. 2.6. Therefore, the contribution of the drag force of each element can be summed to find the total tether drag force [13]. Then, the total drag force applied as a body force into Eq. 2.13 to consider the effect of the tether drag on TUSK performance. Because of the contribution of tether drag force to the normal velocity, the normal velocity of each segment is calculated by:

$$V_{n,1} = V_k - (V_k \cdot t_1)t_1, \quad (2.40)$$

where $V_{n,1}$ is the normal velocity of the kite, V_k is the kite velocity and t_1 is the tether direction.

Since the velocity of the tether attachment is zero, and the velocity of the kite is known ($V_{n,1}$), then the velocity of each segment is calculated by:

$$V_{seg} = \frac{S(j)}{L_{tet}} V_{n,1}. \quad (2.41)$$

Here, V_{seg} is the normal velocity of each segment and $S(j)$, L_{tet} are the distance of each segment from the attachment of the tether and the length of tether, respectively.

Therefore, the drag force of each segment would be:

$$D_{tether,seg} = 0.5C_{d,seg}\rho_t V_{seg}^2 A_{seg}. \quad (2.42)$$

Here, $C_{d,seg}$ is the drag coefficient of each segment, ρ_t is the tether density, A_{seg} is the area of each element, which is obtain by multiplying of the diameter of the tether by the length of the each segment. Finally, the drag force of each segment is summed up and added as a body force to the governing equations. In this study the drag coefficient of each segment, $C_{d,seg}$, is taken to be 1.2 [23].

Chapter 3

Verification of the Computational Method

In this chapter a number of comparisons with existing results, Reynold independency, and grid refinement studies have been conducted in order to verify the moving computational method, and to assess the grid resolution requirements for the problems considered in the chapter 4. Note that the computational method was initially developed by extending and modifying a code used to model tethered floating structures in [99]. The accuracy of that computational method was also validated in [99] by comparing simulation results with various analytical, numerical and experimental predictions for floating bodies exposed to unsteady wave loadings. Since 2D simulations have been conducted as a preliminary step of modeling TUSK system, Reynold independency and grid refinement studies of 2D numerical tool is also investigated.

3.1 Grid and Reynolds Number Independency of the Computational Method

A uniform, regularly structured grid that encompasses a $6\text{ m} \times 5\text{ m} \times 10\text{ m}$ domain size is used for mesh in-dependency study in 3D simulations as shown in Fig. 3.1.

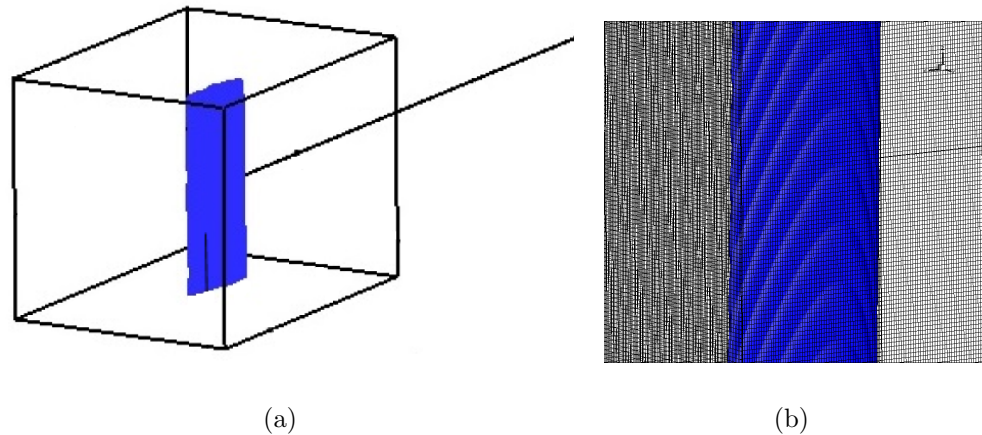


Figure 3.1: a) Schematic diagram of the kite-tether system, and b) computational grid in 3D simulations. Not to scale.

The kite is controlled to have a figure-8 shape motion in a moving numerical domain. Figure 3.2 shows the tether force, power output and the cross-current velocity for three different mesh resolutions. The results have converged for the 1.6×10^6 grid in a moving numerical domain, which is then used for the 3D simulations.

A grid refinement study has been carried out to ensure the independency of the 2D baseline simulation with grid mesh resolution in which a uniform grid that encompasses a $11\text{ m} \times 9\text{ m}$ domain size is used as shown in Fig. 3.3(b). Figure 3.4 shows the vertical position and velocity of the kite's center of mass vs time for three different mesh resolutions. The results converged for an 880×720 mesh.

In addition, the independency of the 3D computational results with Reynolds number is studied through three simulations at Reynolds number (based on kite chord) of 10^3 , 10^4 , and 10^5 . A schematic of the numerical domain is shown in Fig. 3.5. The length of the tether is constant in these simulations. The Reynold number is calculated by

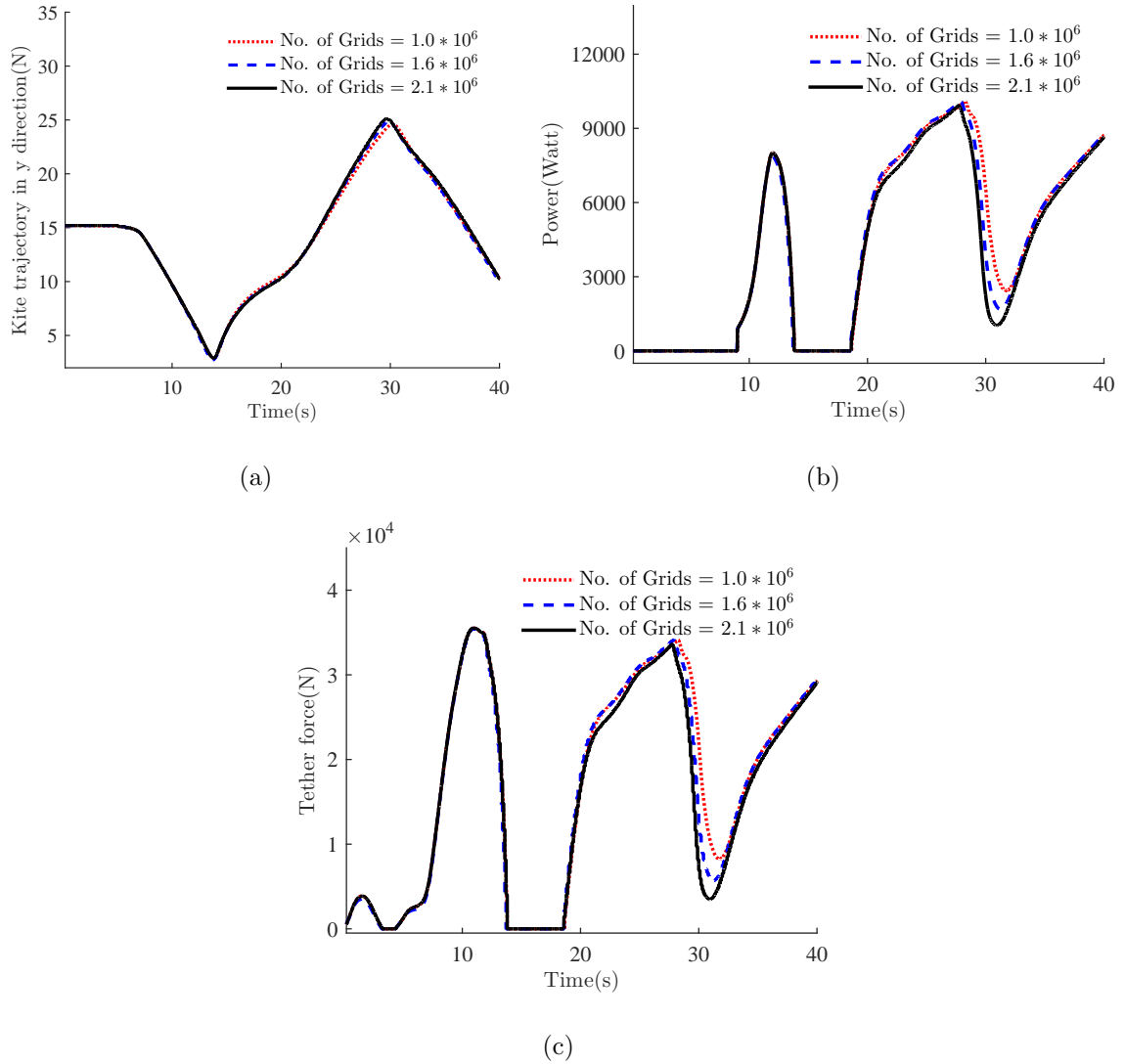


Figure 3.2: Grid resolution effect in 3D simulations on: a) cross-current motion of the kite, b) power generation, c) tether force.

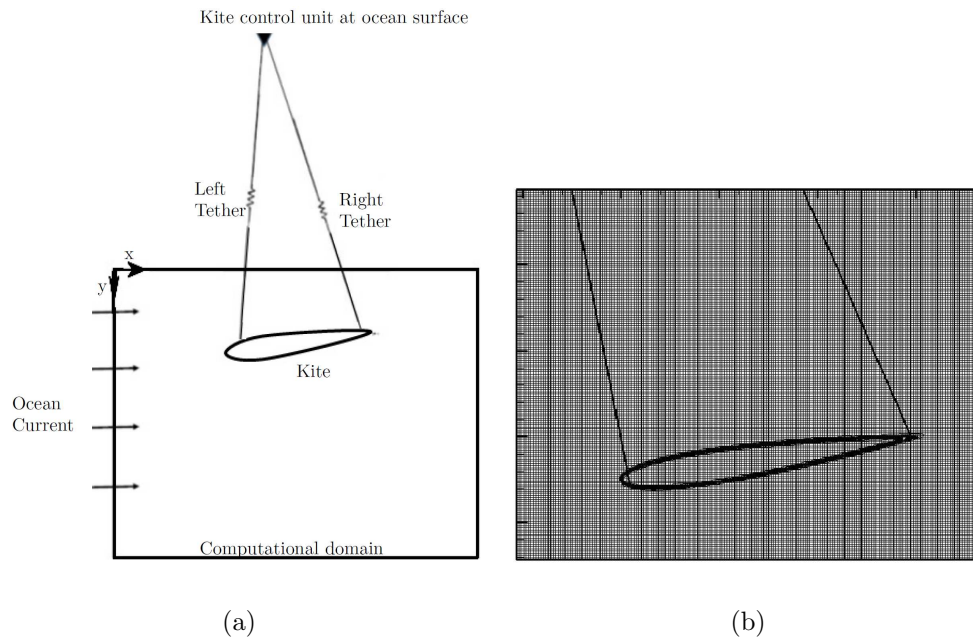
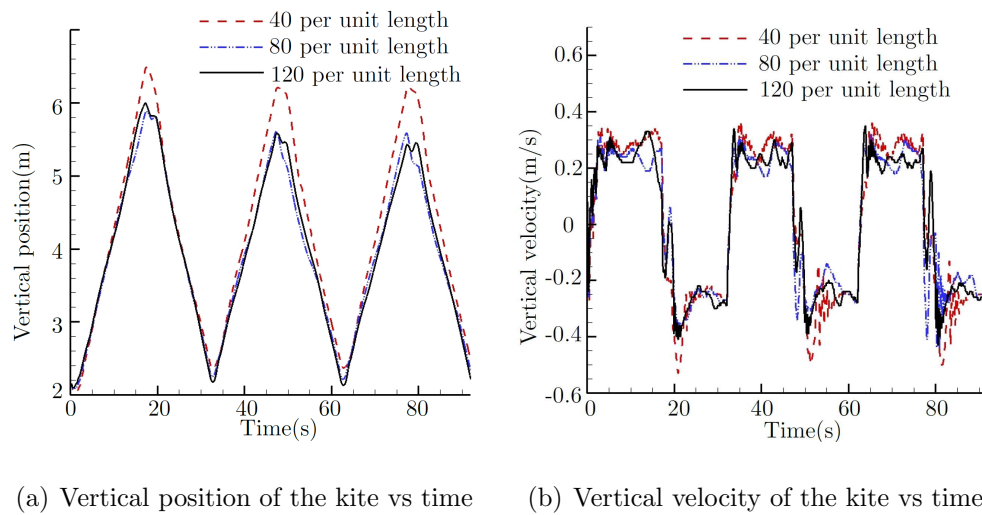


Figure 3.3: a) Schematic diagram of the kite-tether system and computational domain in 2D simulations. Not to scale. b) Numerical grid.



(a) Vertical position of the kite vs time (b) Vertical velocity of the kite vs time

Figure 3.4: Grid refinement study in 2D simulations showing the effect of different grid resolutions on the kite position and velocity.

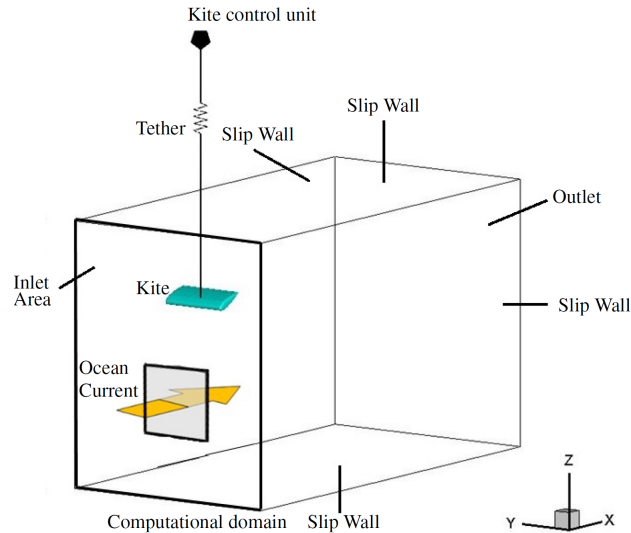


Figure 3.5: Schematic of the tethered kite in a fixed numerical domain to study Re independency for 3D simulations.

Eq. 3.1.

$$Re = \frac{\rho u c}{\mu}. \quad (3.1)$$

Here, ρ is the water density, u is the inlet current velocity, and c is the chord length of the kite. It is shown in Fig 3.6 that the 3D simulation results are largely independent of Reynolds number.

Also, four simulations with Reynolds number equal to 3000, 6000, 12000 and 20000 have been performed in 2D numerical domain. It is shown in Fig. 3.7 that the effect of viscous forces is small in the 2D baseline simulation.

3.2 Moving Domain Verification

As mentioned earlier, the moving computational domain is used to reduce the computational cost. Therefore, two test cases are studied to assess the accuracy and

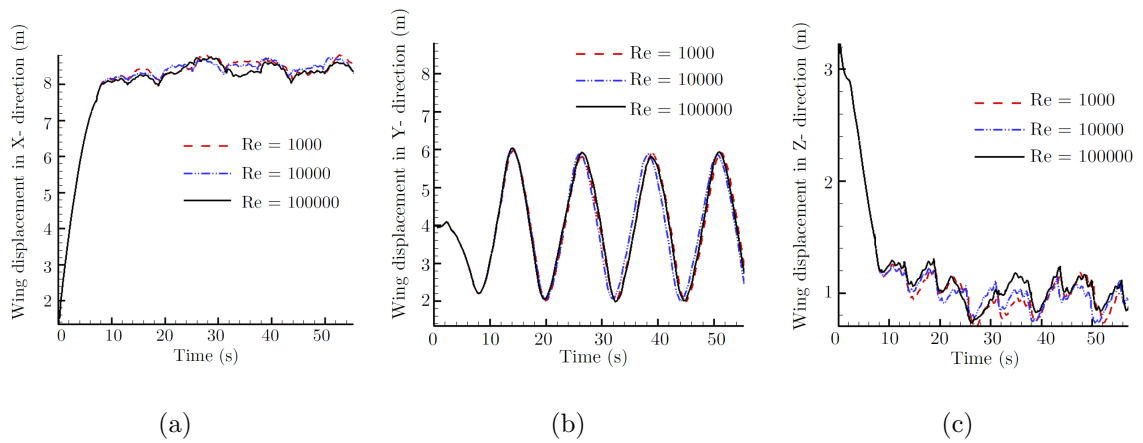


Figure 3.6: The effect of Reynolds number on the displacement of the kite center of mass in: a) x, b) y, and c) z directions, for 3D simulations.

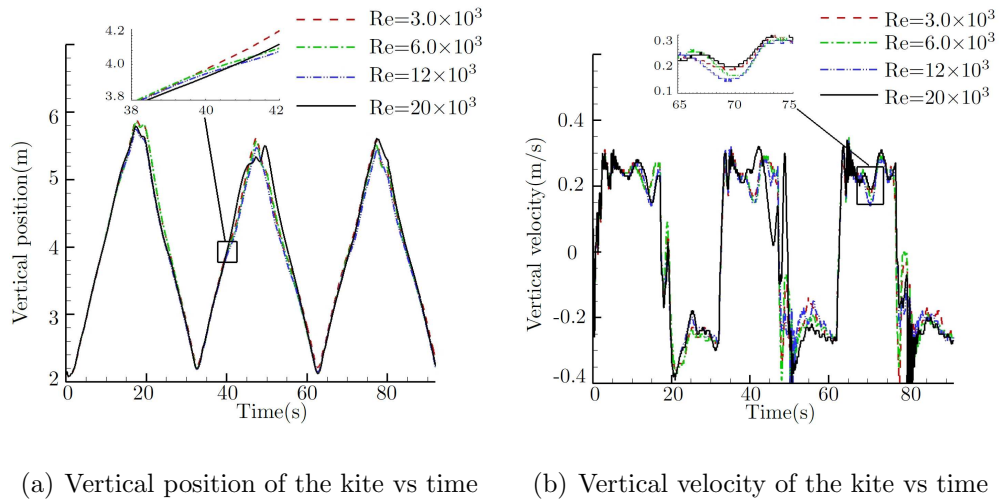


Figure 3.7: The effect of varying Reynolds number in 2D simulations on the kite position and velocity.

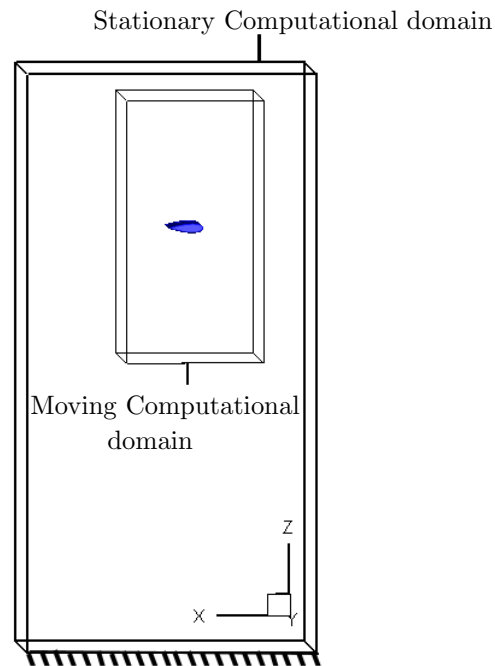


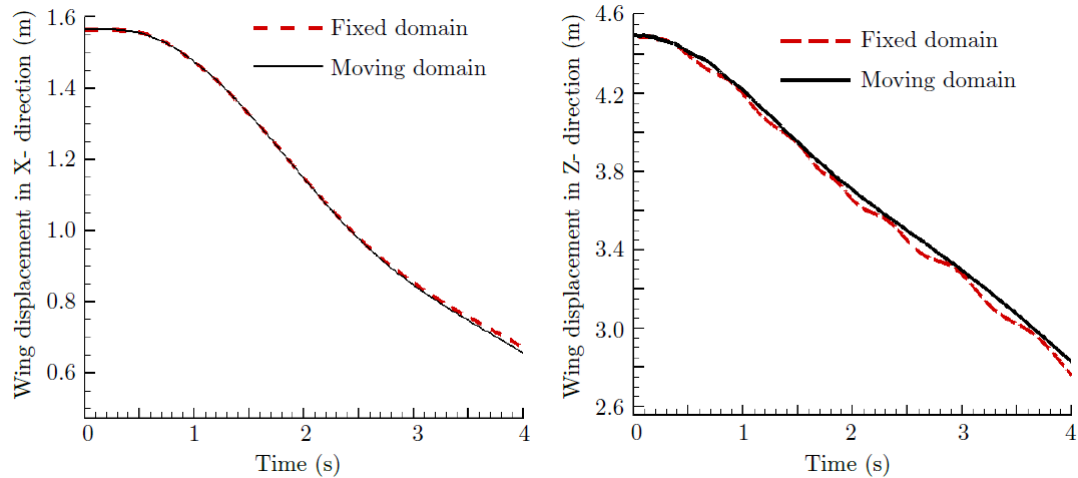
Figure 3.8: Initial position of the airfoil wing in computational domains.

performance of the approach in moving computational domain. The results from moving numerical domain simulations are compared and verified with the fixed computational domain results. The accuracy of a fixed numerical domain was validated with various analytical, numerical and experimental predictions for floating bodies exposed to unsteady wave loadings [99].

3.2.1 Free Fall of an Airfoil Wing in a 3D Fluid Container

Two simulations have been carried out in which a rigid 3D airfoil wing is made to fall under the influence of gravity in a stationary and a moving domain as illustrated in Fig. 3.8.

A NACA 0021 airfoil wing with the span/chord ratio of 1.33 falls from 4.5 m above



(a) Trajectory of the center of mass of the airfoil wing in x direction. (b) Trajectory of the center of mass of the airfoil wing in z direction.

Figure 3.9: Displacement of the center of mass of the airfoil-wing free-falling in a fluid container in fixed and moving numerical domains.

the stationary domain bottom. The solid to fluid density ratio ($\frac{\rho_s}{\rho_f}$) is 1.5 and the fluid dynamic viscosity is 10^{-5} kg/ms . The height of moving numerical domain is the half of the height of the fixed computational domain and it can move freely in x and z directions based on the motion of the wing. Fig. 3.9 presents center of mass trajectories in the x-z plane and shows a very good agreement between moving and stationary domain results.

3.2.2 A Moving Tethered Underwater Kite for Power Generation

Two other simulations were performed using fixed and moving numerical domains in which a tethered kite is placed in a uniform current flow, as shown in Fig. 3.10. The

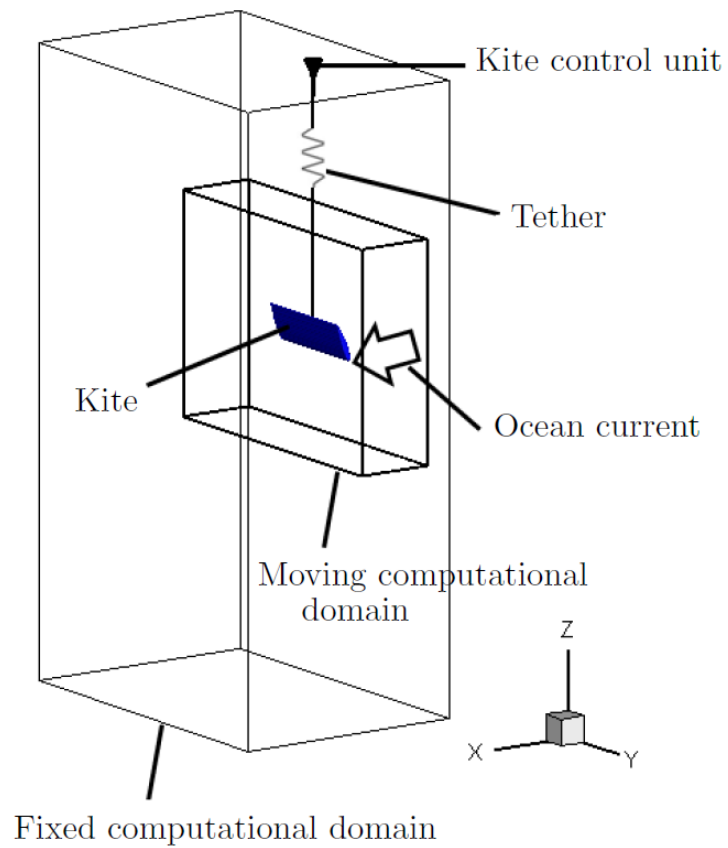


Figure 3.10: Schematics of the moving and fixed computational domains for tethered kite which is placed across the uniform flow. Not to scale.

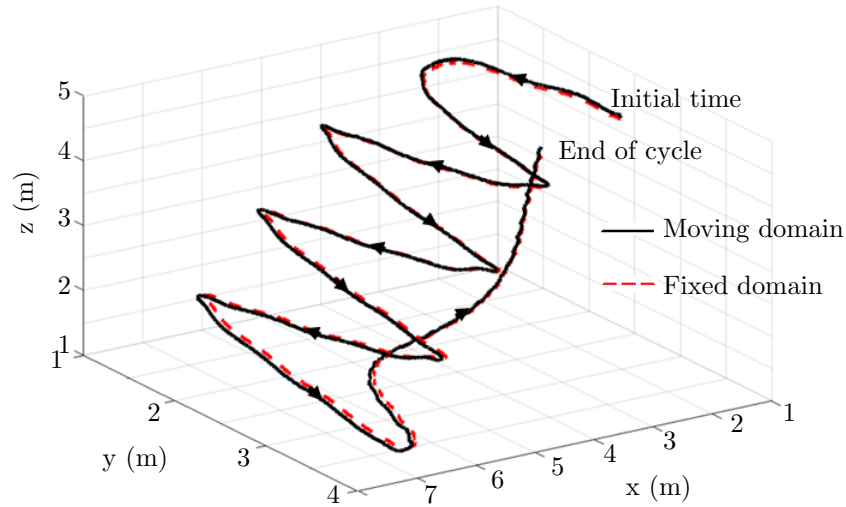


Figure 3.11: The comparison of the center of mass trajectory of a tethered kite placed in a uniform flow in moving and fixed computational domains.

kite is controlled to generate net power output during a power-retraction cycle by a PID controller in which the actual kite angle in pitch, roll and yaw are controlled to reach a desired trajectory. The input parameters for both fixed and moving numerical domain simulations are presented in Table 3.1. Since it is computationally intensive for the simulation with a fixed numerical domain, the cross-current movement of the kite center of gravity is restricted to 2 m . The trajectory of the kite center of mass is illustrated in Fig. 3.11 which demonstrates that the results of the moving numerical domain simulation match well with the data of the fixed numerical domain.

3.3 The Effects of Slip and No-slip Boundary Conditions

In this section, the effect of slip and no-slip boundary condition at the wing (solid) interface is investigated. The numerical domain size is 6 $m \times 4 m$, in which a 2D stationary airfoil wing is located across the uniform current flow as shown in Fig. 3.12.

Table 3.1: Input parameters for the tethered kite in the moving and fixed numerical domains.

	Fixed domain	Moving domain
Domain Size	$10 \times 5 \text{ m} \times 6$	$3 \times 4 \text{ m} \times 4$
Kite Chord Length	$c = 0.75 \text{ m}$	$c = 0.75 \text{ m}$
Kite Span Length	$b = 1.5 \text{ m}$	$b = 1.5 \text{ m}$
Tether Spring Stiffness	$k = 1.2 \times 10^4 \text{ N/m}$	$k = 1.2 \times 10^4 \text{ N/m}$
Reynolds Number	$Re = 7.5 \times 10^4$	$Re = 7.5 \times 10^4$
Power Cycle Time Period	$T = 37 \text{ s}$	$T = 37 \text{ s}$
Retraction Cycle Time Period	$T = 23 \text{ s}$	$T = 23 \text{ s}$
Tether Velocity	$V_t = 0.15 \text{ m/s}$	$V_t = 0.15 \text{ m/s}$
Ocean Current Velocity	$V_c = 1 \text{ m/s}$	$V_c = 1 \text{ m/s}$
Number of Tether Springs	1	1
Water Viscosity	$\mu = 10^{-5} \text{ Pa.s}$	$\mu = 10^{-5} \text{ Pa.s}$
Water Density	$\rho_w = 1000 \text{ kg/m}^3$	$\rho_w = 1000 \text{ kg/m}^3$
Kite Density	$\rho_k = 1350 \text{ kg/m}^3$	$\rho_k = 1350 \text{ kg/m}^3$
Time Step Size	$\Delta t = 2 \times 10^{-3} \text{ s}$	$\Delta t = 2 \times 10^{-3} \text{ s}$
Initial Length of Tether	7 m	7 m
Temperature	20°	20°

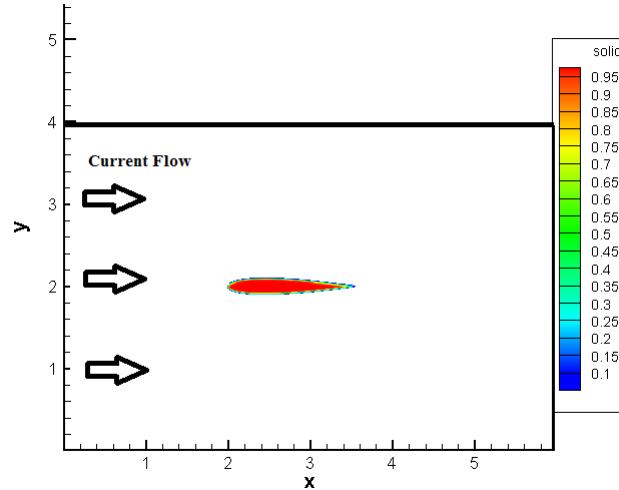
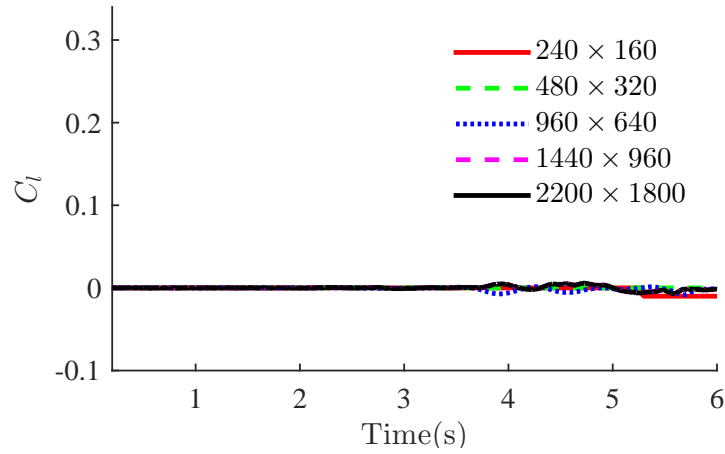


Figure 3.12: Schematic of a 2D airfoil wing with zero angle of attack which is placed across the uniform current flow.

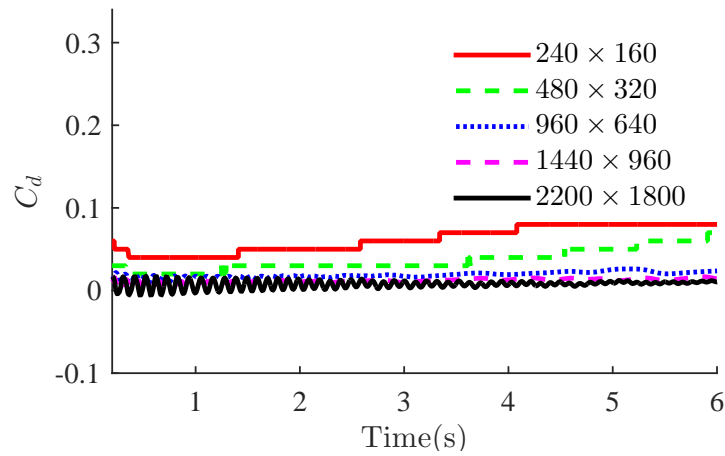
Simulations with different grid resolutions have been carried out in which the chord length and Reynolds number are 1.5 m and 1.5×10^6 , respectively for the simulations.

The effect of no-slip condition at different grid resolutions is shown in Fig. 3.13. Since the symmetry airfoil wing (NACA 0012) is used in these simulations, the lift coefficient is almost zero (Fig 3.13(a)), and the wing drag coefficient has converged for the 1440×960 grid in x and y directions (240 grids per unit length) as shown in Fig. 3.13(b). Three dimension simulations using this grid resolution would be very computationally intensive and are not feasible.

The effect of viscous drag is considered in no-slip boundary condition. Since the direct numerical simulation (DNS) scheme is used in this study, the drag estimation is highly dependent to the grid resolution. In order to capture the precise viscous drag, adequate grid resolution should be used in the boundary layer which increases the computational run-time drastically. The coarser grid resolution demonstrated



(a) The airfoil wing lift coefficient at different grid resolutions.



(b) The airfoil wing drag coefficient at different grid resolutions.

Figure 3.13: Lift and drag coefficients of a NACA-0012 airfoil wing at different grid resolutions for zero angle of attack ($AOA = 0$). The no-slip condition is imposed at the wing interface.

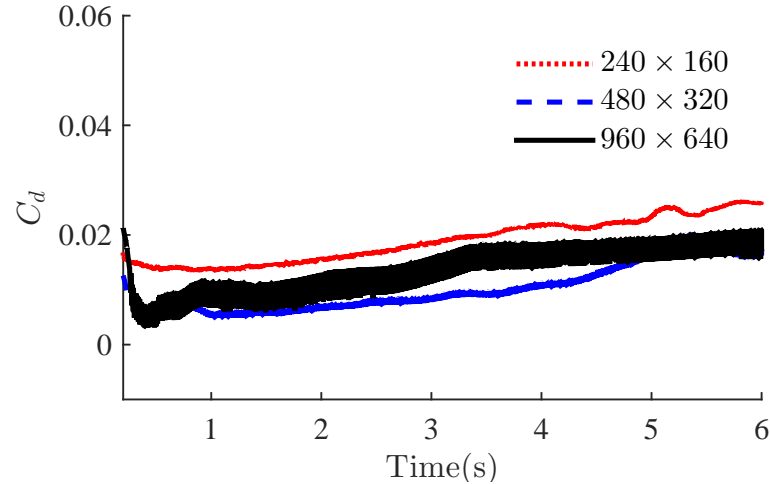
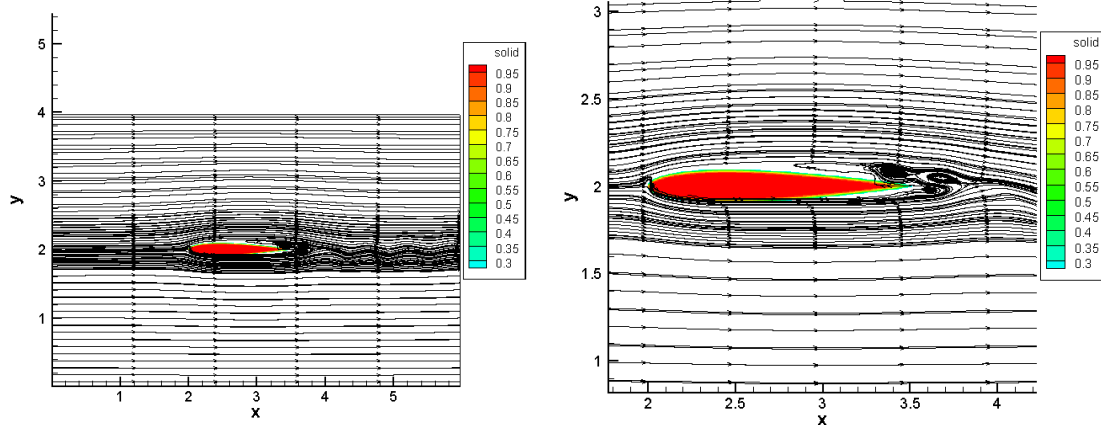


Figure 3.14: Drag coefficient of a NACA-0012 airfoil wing for different grid resolutions at zero angle of attack ($AOA = 0$). The slip condition is imposed at the wing interface.

the higher wing drag compared to the theoretical value as shown in Fig. 3.13(b) which leads to lowered accuracy of estimation of the lift to drag ratio for TUSK systems. Therefore, the slip boundary condition is implemented at the kite interface to accurately predict of the the kite drag, in lower grid resolutions. So, 3D baseline simulations would be feasible to perform and study in a resealable time. In summary, the inability to accurately resolve the boundary layer due to run time limitations in 3D simulations, allows us to relax the no-slip condition, and use a slip condition to accurately model wing pressure drag.

The effect of the grid resolution for the slip boundary condition at the wing interface for $AOA=0$ is considered in Fig 3.14. It shows that the drag coefficient matches well with the analytical result at the coarser grid resolutions. Also, the drag coefficient of the wing is converged for 480×320 grids in x and y directions (80 grids per unit length). It should be noted that the drag coefficient is not zero in slip condition due to the presence of the flow separation (pressure drag) at the wing trailing edge



(a) Streamline around the airfoil wing. (b) Streamline around the airfoil wing. Zoom-in

Figure 3.15: Streamline around the airfoil wing at zero angle of attack ($AOA = 0$). The slip condition is imposed at the wing interface.

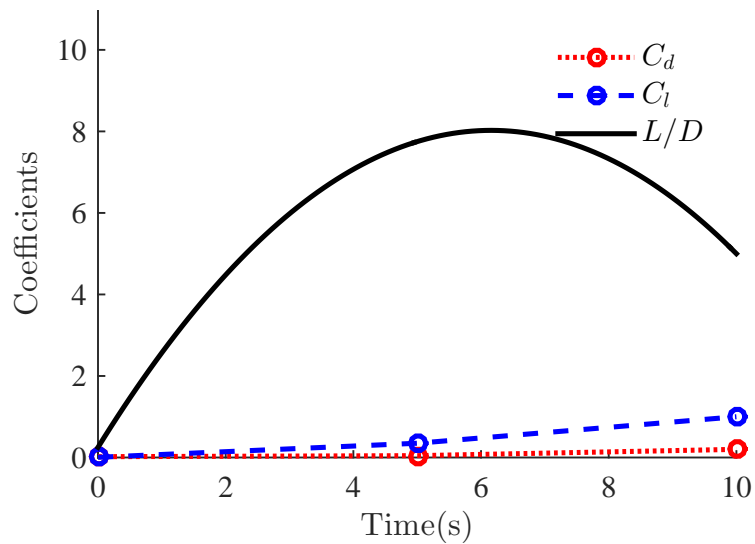


Figure 3.16: Drag, lift, and lift to drag ratio of the airfoil wing at three different angle of attack ($AOA = 0$). The slip condition at the wing interface is imposed.

as shown in Fig. 3.15. The separation is captured by solving the full Navier-Stokes equations, while this effect cannot be caught by linear potential flow theory.

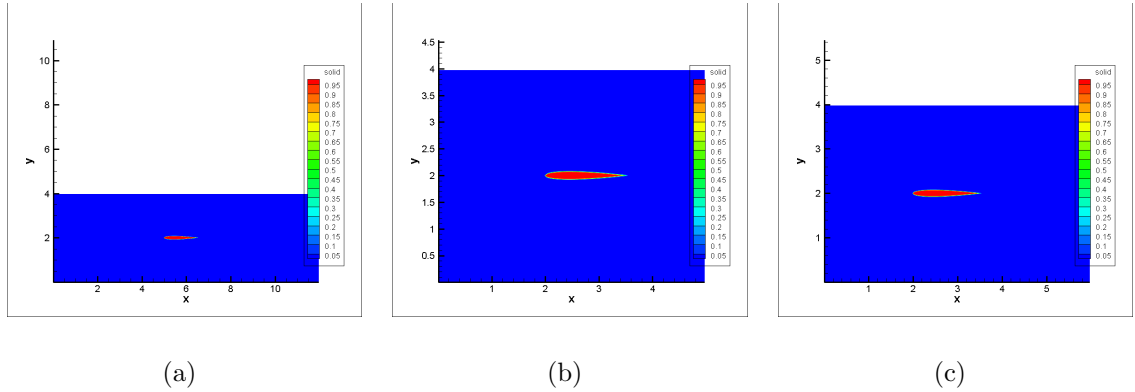


Figure 3.17: a) The location of airfoil wing far from the inlet and far from the outlet. b) The location of the airfoil wing close to the outlet. c) The location of the an airfoil wing in the numerical domain in the baseline simulation that is tested in section 3.3.

Moreover, the effect of variation of the angle of attack with the slip condition around the airfoil wing is considered. Three different simulations with the $AOA=0$, $AOA=5$ and $AOA=10$ have been carried out and it is shown that the lift to drag ratio is maximized at an angle of attack around $6^\circ - 7^\circ$, as shown in Fig. 3.16.

3.4 The Effects of Domain Size on Numerical Results

In this section, the effect of boundary condition and domain size on the numerical results is studied. Three different simulations in 2D have been performed with the numerical domain sizes are $12\text{ m} \times 4\text{ m}$, $6\text{ m} \times 5\text{ m}$, and $6\text{ m} \times 4\text{ m}$, in which a 2D stationary airfoil wing is located across the uniform current flow as shown in Figures 3.17. The slip boundary condition is imposed at the wing interface and the effective angle of attack of the wing is zero.

The effect of domain size on the wing drag coefficient is shown in Fig. 3.18. It shows

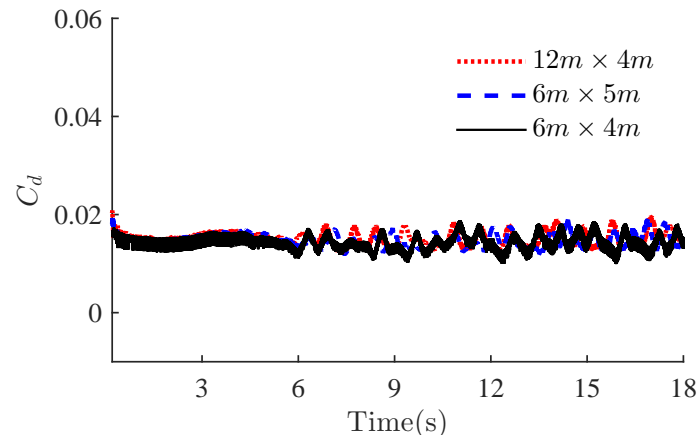


Figure 3.18: Drag coefficient of the airfoil wing at three different domain sizes. The slip condition at the wing interface is imposed.

that the domain size and boundary conditions have a small effect on numerical results (wing drag coefficients) when there is a reasonable distance between boundaries and the airfoil wing.

Chapter 4

Results

In this section the results for simulations of the a tethered undersea kite, are examined in detail. The effects of key design parameters on TUSK systems performance are explored. The power output is compared with established theoretical results by Loyd [15]. The performance of the controller schemes to control the kite angles to have a desired trajectory is studied. As mentioned earlier, a 2D computational tool is developed as a preliminarily step for studying TUSK systems. Therefore, a baseline simulation and the effect of varying different parameters on the power output of 2D TUSK systems is studied first in this section. Then, a baseline simulation in a three dimensional domain, where a high net power output is achieved during a power and retraction cycle, is investigated. Finally, the effect of the tether velocity during the retraction phase and the tether drag on TUSK performance have been studied.

4.1 Two-dimensional Baseline Simulation

The input parameters for the 2D simulation are listed in Table 4.1.

The tether spring stiffness is set to match the elasticity of Nylon 6, a potential TUSK tether material. The phase shift for unstretched tether length (see Fig. 2.2) was

Table 4.1: Input parameters for 2D baseline simulation

Domain Size	$11 \times 9 \text{ m}$
Kite Chord Length	$c = 1.5 \text{ m}$
Tether Spring Stiffness	$k = 10^5 \text{ N/m}$
Reynolds Number	$Re = 12 \times 10^3$
Power-Retracton Cycle Time Period	$T = 30 \text{ s}$
Phase Shift (unstretched tether length)	$T_d = 2.3 \text{ s}$
Tether Velocity	$V_t = 0.3 \text{ m/s}$
Ocean Current Velocity	$V_c = 1 \text{ m/s}$
Number of Tether Springs	2
Water Viscosity	$\mu = 0.5 \text{ Pa}\cdot\text{s}$
Water Density	$\rho_w = 1000 \text{ kg/m}^3$
Kite Density	$\rho_k = 2000 \text{ kg/m}^3$
Time Step Size	$\Delta t = 10^{-3} \text{ s}$
Tether Attachment Point Coordinates	$(2.25, -5) \text{ m}$

adjusted to achieve the maximum achievable power output for the baseline simulation. Also, Fig. 2.2 shows that the tether could be consider as a rigid body since the difference between the actual and unstretched lengths of the tether is very small. Input values in Table 4.1 are set to model typical TUSK system parameters. The computational domain size and the resultant kite motion amplitudes are kept small in this study to limit computational run time. Instantaneous snapshots (in time) from an animation of the kite motion during a power-retraction cycle are shown in Fig. 4.1.

In Fig. 4.2, time records of the kite geometric (α_G) and effective (α_{eff}) angles of

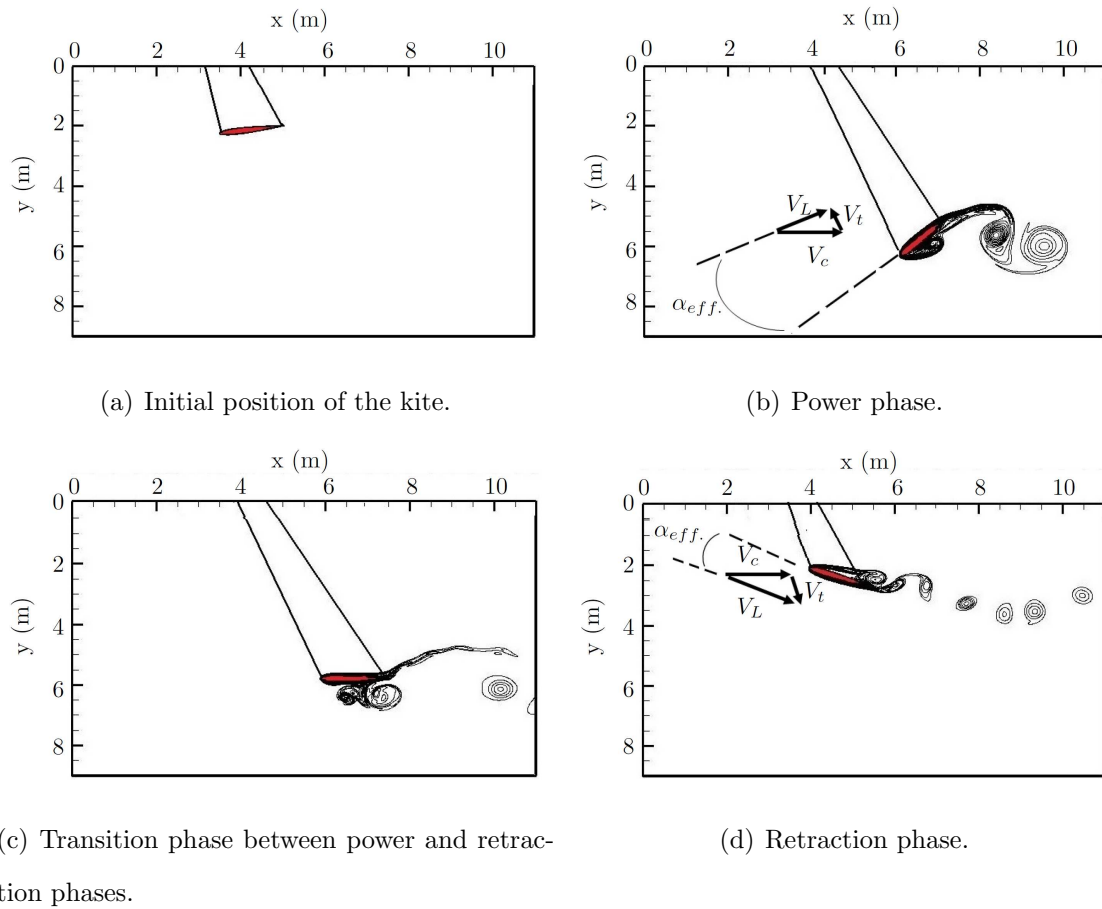


Figure 4.1: Snapshots of the kite position during a power-retraction cycle showing vorticity contours. The tethers are attached 5 m above the top of the computational domain.

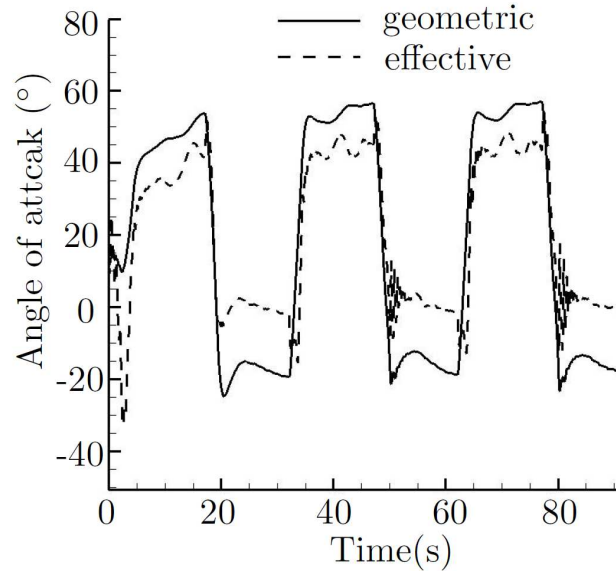


Figure 4.2: Angle of attack of the kite vs time.

attack are presented. The velocity diagrams in Figs. 4.1(b) and 4.1(d) define the kite effective angle of attack. All velocity vectors are with respect to an observer on the kite. The effective angle of attack is defined based on the kite chord line and local current vectors, and thus accounts for the effect of the kite motion on the angle of attack. Positive geometric and effective angles of attack are required during the power phase to obtain larger hydrodynamic forces. Effective angles of attack near 0° during the retraction phase yields low kite hydrodynamic forces and less power consumed. By adjusting the rest length of the tethers as in Fig. 2.2, appropriate geometric and effective angles of attack can be achieved to maximize net power production. The effective angle of attack values during power phase approach 40° which is above the stall angle of NACA 0012 airfoil in steady flow.

The trajectory of the kite center of mass for three power-retraction cycles is presented in Fig. 4.3. It is shown that after the first cycle, the kite travels along a fairly stable periodic path.

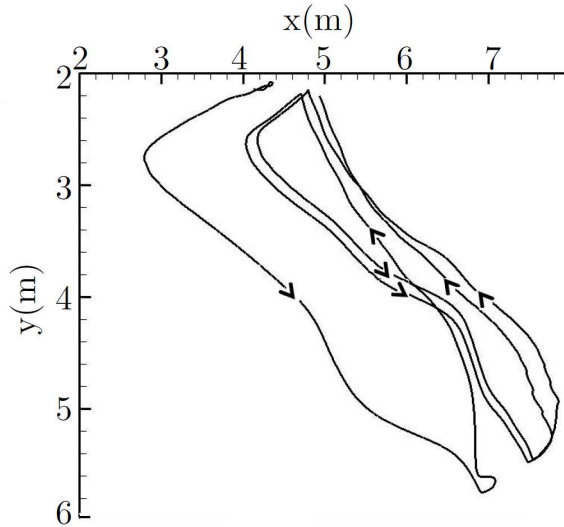


Figure 4.3: Trajectory of the kite vs time. The direction of the kite motion is shown by the arrows

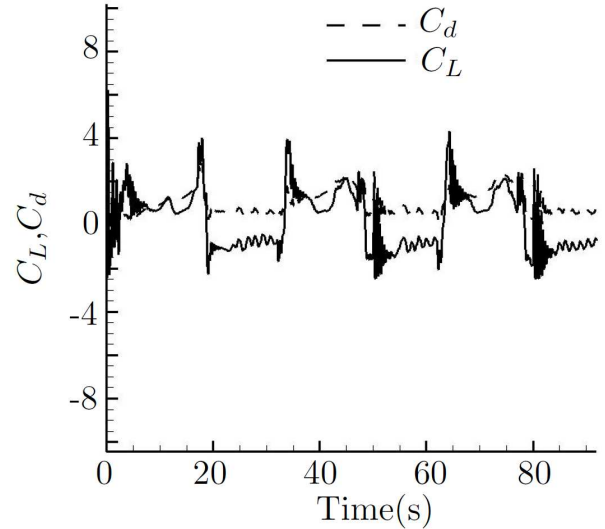


Figure 4.4: Hydrodynamic lift and drag coefficient of the kite vs time.

Hydrodynamic lift and drag coefficients are shown in Fig 4.4. Lift and drag forces in the 2D baseline simulation were obtained by determining the resultant force of tethers in the vertical and horizontal directions, respectively. Kite weight and buoyancy forces were subtracted from the resultant force on the tethers to isolate the hydrodynamic lift. The lower L/D ratios observed in Fig 4.4 are due to the higher effective angle ($\alpha_{eff} = 40^\circ$) above stall and the lower Reynolds number.

The tether tensions during the power and retraction cycle are shown in Fig 4.5. Tether tensions can help determine required tether materials for TUSK systems. The reel-in and reel-out velocity of the tethers and the instantaneous power are shown in Fig. 4.6 and Fig. 4.7, respectively. Power is calculated from multiplying the tether tension by the reel-out or reel-in velocity of the tethers. Fig. 4.7 demonstrates that the average power that is produced during power phase is almost twice that of the

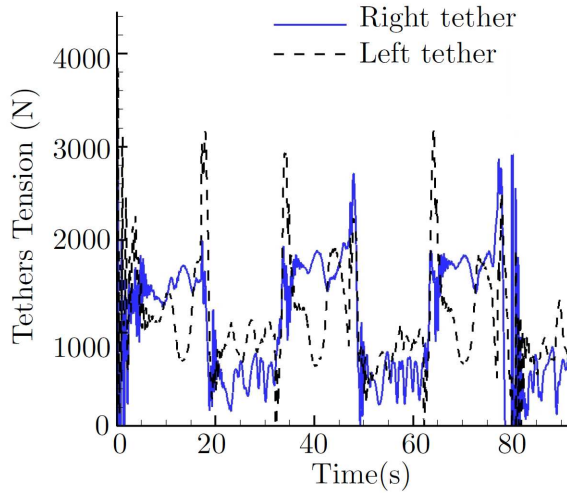


Figure 4.5: Tethers tension vs time.

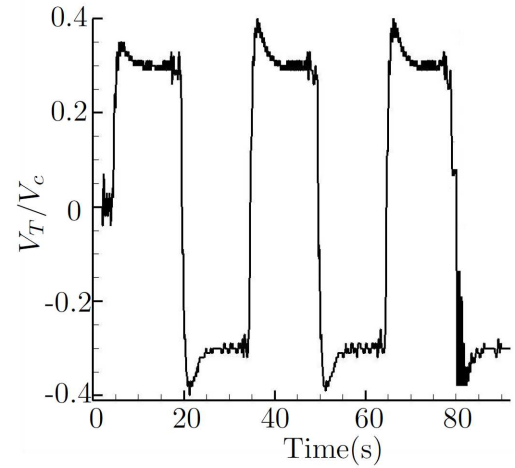


Figure 4.6: Tether velocity vs time.

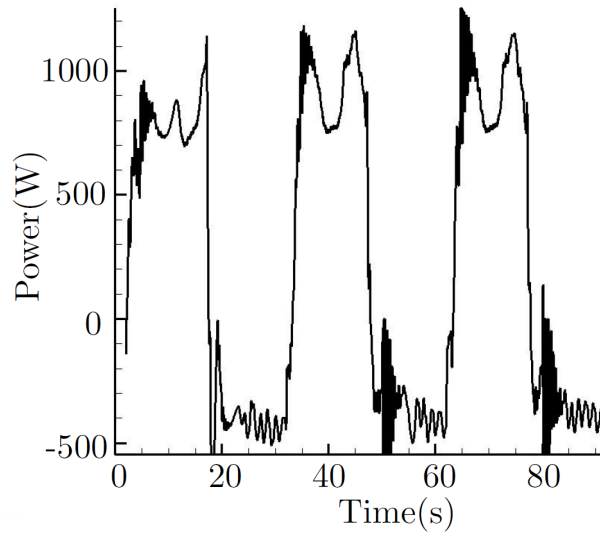


Figure 4.7: Power obtained for successive cycles for a 2D tether kite system vs time.

power consumed during retraction phase, yielding a positive net power production.

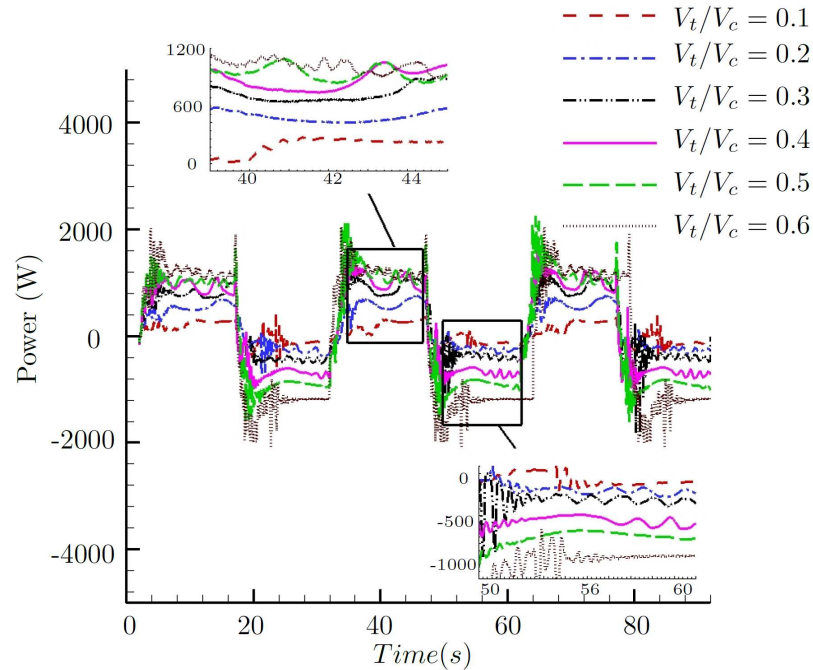


Figure 4.8: Effect of the ratio of tether to current velocity on power output. Enlarged views show details of the power output during the power and retraction phases.

4.1.1 Parametric Study

Effect of Tether to Current Velocity Ratio

In order to validate our power estimates and numerical scheme, a parametric study on input tether velocity was undertaken to allow us to compare with earlier theoretical results of Loyd [15]. Six different simulations with different V_t/V_c ratios have been conducted. In these six simulations other input values are adjusted to keep the average lift-to-drag ratio L/D of the kite at $L/D = 0.6$. By carefully studying the close-up views in Fig. 4.8, it is observed that the average power output during the power phase peaks for $0.4 \leq V_t/V_c \leq 0.6$. However, during retraction there is increasing consumed power as V_t/V_c increases from 0.4 to 0.6.

Therefore the optimal ratio should be near $V_t/V_c = 0.4$. The results are compared with a theoretical power prediction for a simple moving kite in two dimensional motion during the power phase from Loyd [15]. The normalized power coefficient, F_s , for the current 2D numerical simulations is obtained by:

$$F_s = \frac{P}{0.5\rho cV^3C_L}, \quad (4.1)$$

which is used to non-dimensionlize the average power phase output, P , from the simulations (after subtracting the power created by the net buoyancy force). c is the chord length of the kite and the average lift coefficient C_L in Eq. (4.1) is output from the simulations and varies between $0.5 \leq C_L \leq 1.8$ for different simulations. The theoretical power coefficient from Loyd [15] is given in Eq. (4.2).

$$F_{sL} = \frac{\frac{V_t}{V_c} \left\{ \sqrt{1 + \frac{1}{(L/D)^2} - \left(\frac{V_t}{V_c}\right)^2} - \frac{V_t}{V_c} \right\}^2}{\sqrt{1 + \frac{1}{(L/D)^2}}}. \quad (4.2)$$

There is good agreement between our normalized power output and Loyd's results as shown in Fig. 4.9, which also confirms that the maximum power is obtained at $V_t/V_c \cong 0.4$.

Effect of Kite Weight on Power Output

Another study was performed where kite to water density ratios ($\rho_k/\rho_f = 2.0, 3.0$ and 4.0) were varied with other parameters set as in Table 4.1. The instantaneous power output during reel-out and reel-in cycles is presented in Fig 4.10 which shows that when increasing the kite's density, although more power is obtained during the power phase, more power is consumed during retraction phase. Figure 4.11 shows the

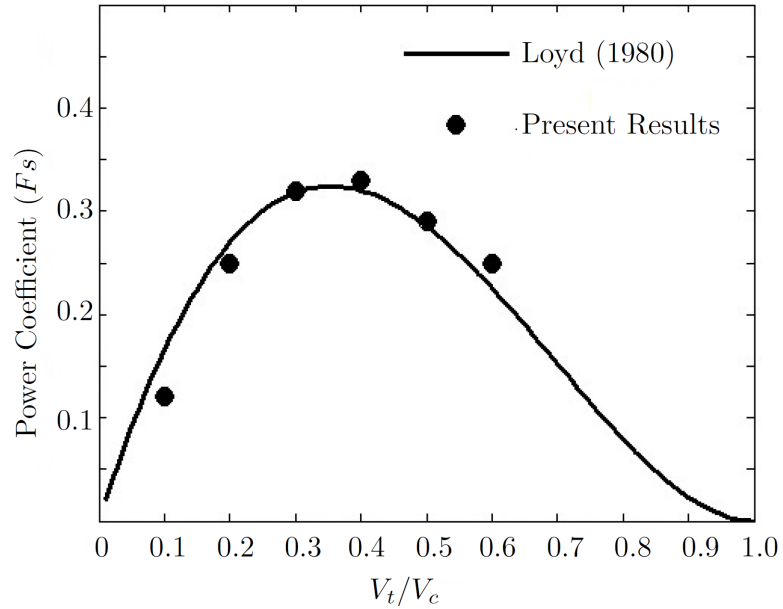


Figure 4.9: Comparison of power coefficients from the simulations with Loyd [15] prediction at $L/D = 0.6$.

variation of normalized power coefficient which is defined by:

$$C_p = \frac{P}{0.5\rho_k V^3 c}, \quad (4.3)$$

where ρ_k is the kite density and c is the chord length of the kite. Figure 4.11 shows that the net generated power is independent of the kite's density in our simulation. This is expected since the generated power due to the falling kite weight (power phase) must be consumed to reel-in the kite weight to a higher elevation during the retraction phase.

The Effect of Ocean Current Velocity

The ocean current velocity effect is studied by carrying out three simulations in which $V_c = 0.5 \text{ m/s}, 1 \text{ m/s}$ and 1.5 m/s , with other input values matching the baseline

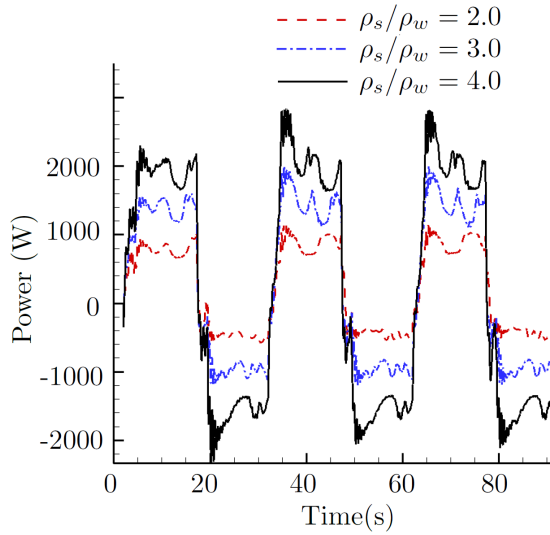


Figure 4.10: Effect of the kite density on power.

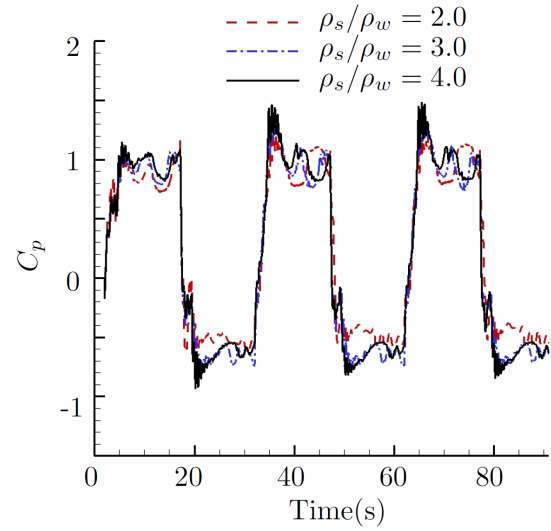


Figure 4.11: Effect of the kite to water density ratio on normalized power coefficient.

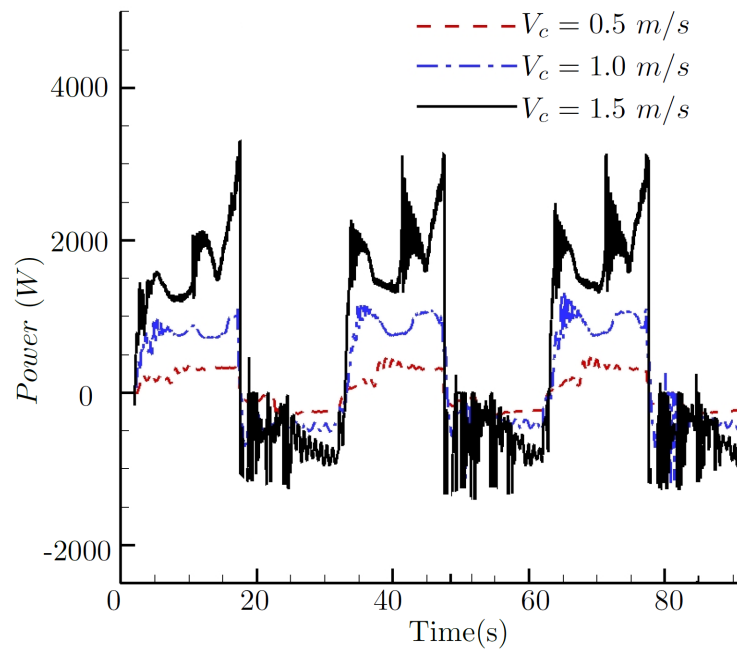


Figure 4.12: Power generated in different ocean current velocity.

simulation. The power output during reel-out and reel-in cycles and the net output

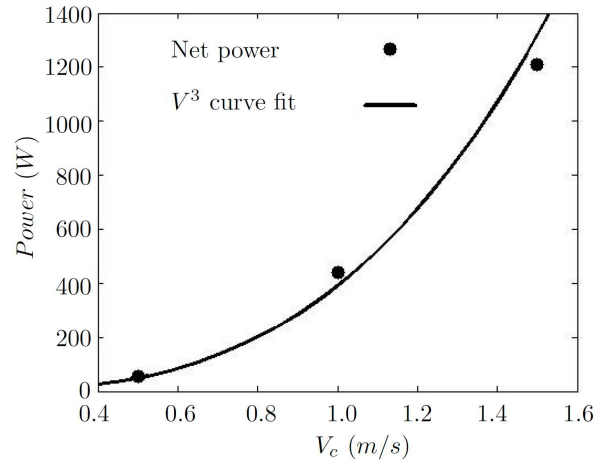


Figure 4.13: Comparison of power generated in different ocean currents with V^3 curve fit.

power are presented in Fig. 4.12 and Fig. 4.13, respectively, and it is observed that the power output is proportional to V_c^3 , as expected.

Effect of Tether Length

The effect of tether length (L_t) on power output was also studied. For this study the computational domain is $25\text{ m} \times 9\text{ m}$, and the ratios of the tether to kite chord length are $L_t/c = 4.5, 15$ and 30 , with other input values matching the baseline simulation. Figure 4.14 shows the instantaneous power output during the power and retraction phases for different ratios of tether to chord length. Since the geometric and effective angle of attack are controlled to have equal values in all three simulations, the hydrodynamic forces and consequently the power are the same for all the cases. Also, the trajectory of the kite center of gravity is plotted in Fig. 4.15 during the time. The kite requires four cycles to reach a near periodic motion for a larger tether to chord length ratio, while in the baseline simulation, where $L_t/c = 4.5$, the kite obtained

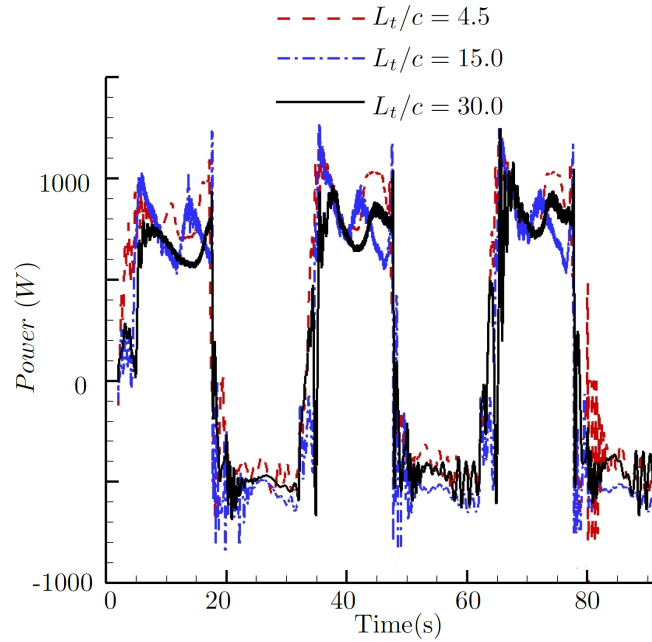


Figure 4.14: Output power vs time for different ratios of tether to chord length.

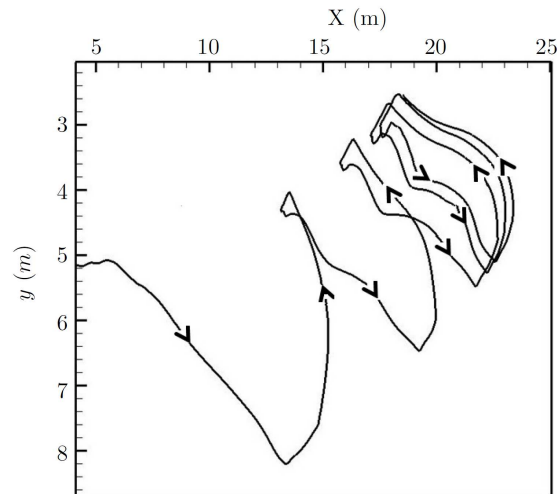
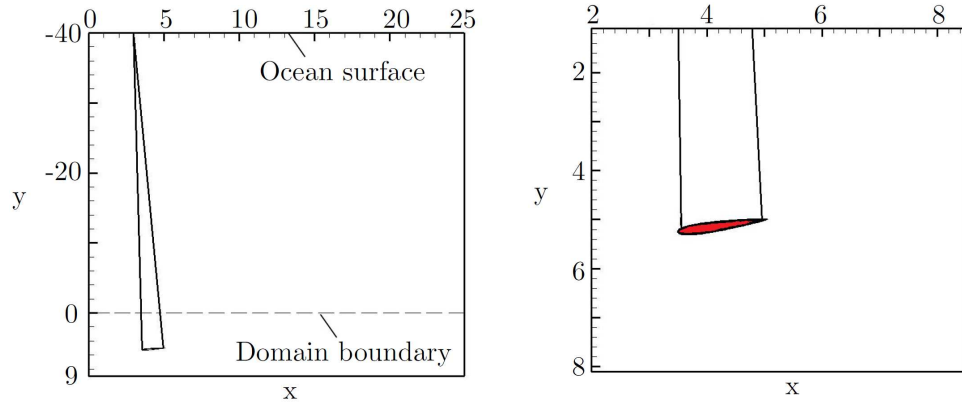


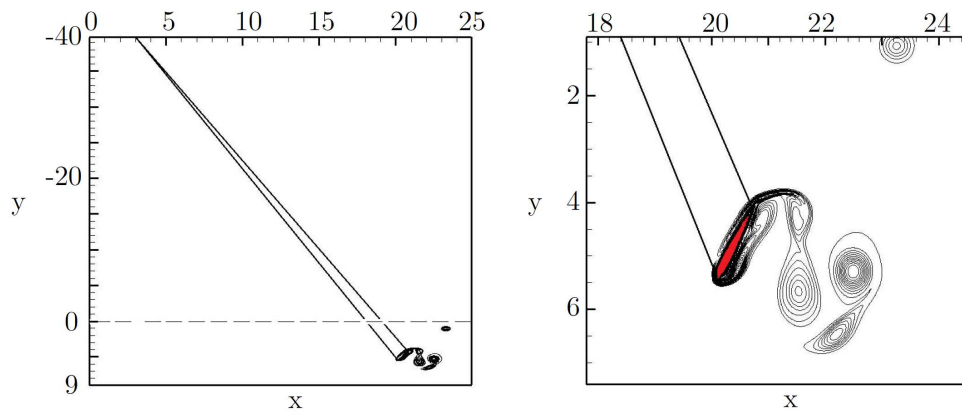
Figure 4.15: Trajectory of the kite center of gravity with $L_t/c = 30$.

the near-periodic path after the first cycle. Figure 4.16 shows vorticity contours at various times for a simulation performed with $L_t/c = 30$. The attachment point of the tethers is placed outside of the computational domain as shown in Fig. 4.16(a).



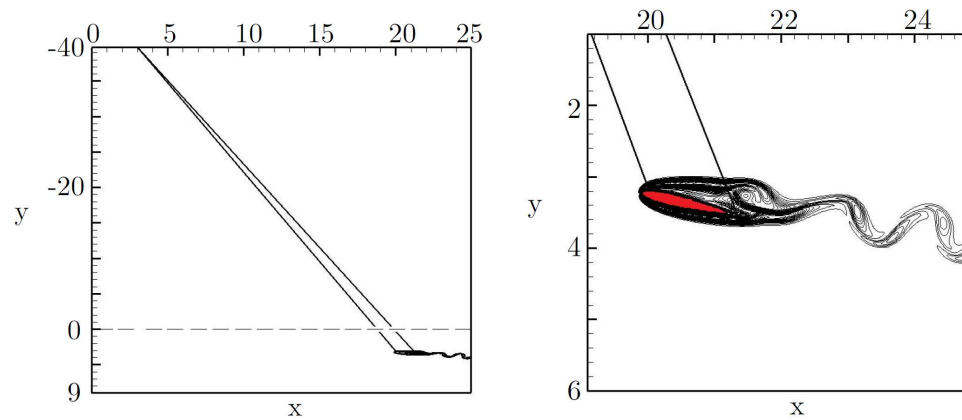
(a) initial position of the kite

(b) Initial position (expand view)



(c) Kite position at 78 s during power phase

(d) Kite position at 78 s (expand view)



(e) Kite position at 91 s during reel-in phase

(f) Kite position at 91 s (expand view)

Figure 4.16: Kite position and vorticity contours with $L_t/c = 30$ at various times.

4.2 Three-dimensional Baseline Simulation

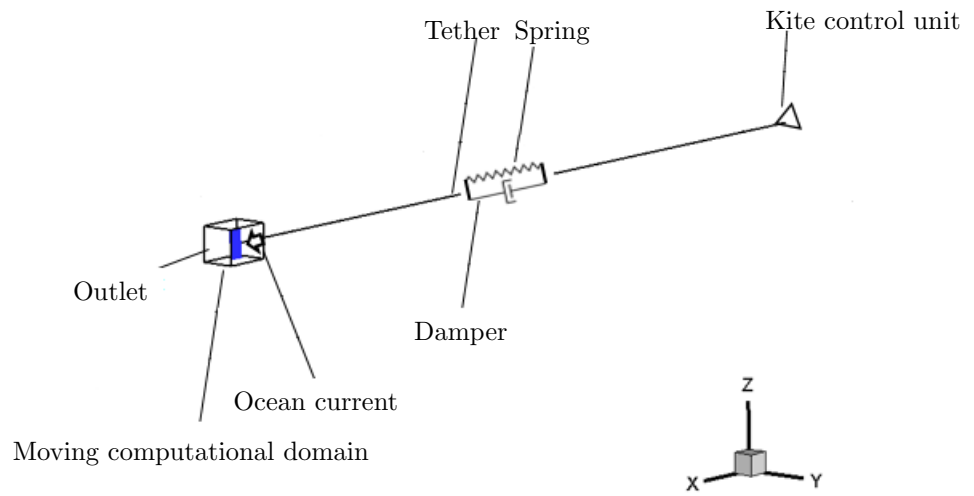
In this section, a baseline simulation for a full-scale three dimensional tethered undersea kite shown in Fig. 4.17 is studied in detail. In order to accurately estimate the kite lift and drag forces in a coarse grid resolution, a free-slip boundary condition is imposed at the kite interface. The simulation assumes a uniform current velocity with ocean depth.

The input parameters for the baseline simulation are presented in Table 4.2. The tether spring stiffness is set to match the elasticity of Nylon 6, a potential TUSK tether materials. The logarithmic decrement of the tether is considered as 0.1 in the baseline simulation, then the damping coefficient of the tether is obtained by the tether stiffness and the mass of the kite.

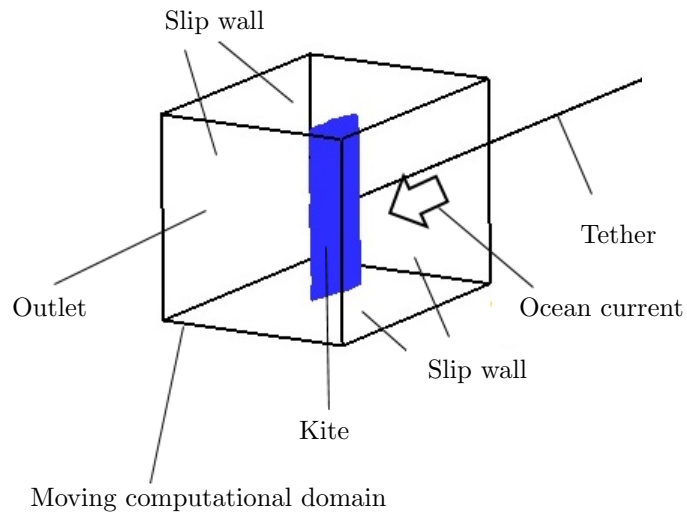
The trajectory of the kite center of mass for a power-retraction cycle is presented in Fig. 4.18. During the reel-out phase the kite moves in successive cross-current motion in a figure-8 pattern, the tether length increases and power is generated. During reel-in the kite motion is along the tether, and kite hydrodynamic forces are reduced so that net positive power is produced.

Top view of instantaneous snapshots (in time) from an animation of the kite motion during a power-retraction cycle are shown in Fig. 4.19. The contours of flow vorticity (λ_2) around the kite from an animation of the kite motion during a power-retraction cycle is shown. λ_2 is defined as the second (in magnitude) eigenvalue of the matrix:

$$S_{ik}S_{kj} + \Omega_{ik}\Omega_{kj}$$



(a) Moving domain and embedded kite which is attached to the fixed structure.

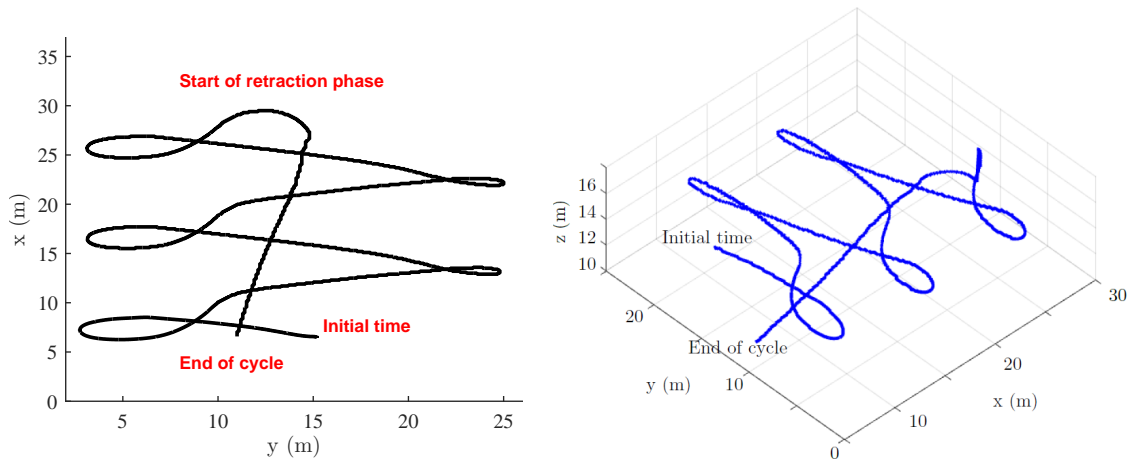


(b) Expand view of the moving computational domain and boundary conditions.

Figure 4.17: Schematic diagram of the tethered underwater kite system and computational domain for the 3D baseline simulation. Not to scale.

Table 4.2: Input parameters for the 3D baseline simulation using the moving numerical domain.

Domain Size	$6\text{ m} \times 5\text{ m} \times 10\text{ m}$
Kite Chord Length	$c = 3.0\text{ m}$
Kite Span Length	$b = 8.0\text{ m}$
Tether Spring Stiffness	$k = 1.0 \times 10^4\text{ N/m}$
Tether Damping Coefficient	$C_{damp.} = 4.0 \times 10^3\text{ N} \cdot \text{s/m}$
Damping Ratio	$\xi = 0.2$
Reynolds Number	$Re = 3.0 \times 10^5$
Power Cycle Time Period	$T = 74\text{ s}$
Retraction Cycle Time Period	$T = 74\text{ s}$
Start Time of Tether Length Changes	$T_s = 7\text{ s}$
Tether Velocity in Power Phase	$V_t = 0.3\text{ m/s}$
Tether Velocity in Retraction Phase	$V_t = 0.3\text{ m/s}$
Ocean Current Velocity	$V_c = 1\text{ m/s}$
Number of Tether Springs	1
Water Viscosity	$\mu = 10^{-5}\text{ Pa}\cdot\text{s}$
Water Density	$\rho_w = 1000\text{ kg/m}^3$
Kite Density	$\rho_k = 1000\text{ kg/m}^3$
Time Step Size	$\Delta t = 4 \times 10^{-3}\text{ s}$
Initial Length of Tether	100 m
Temperature	20°



(a) Top view of kite center of mass trajectory. (b) Kite center of mass trajectory in 3D.

Figure 4.18: Trajectory of kite center of mass vs time.

where:

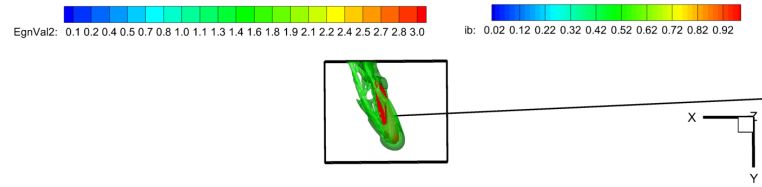
$$S_{ij} = \frac{1}{2} \left(\frac{\partial u_i}{\partial x_j} + \frac{\partial u_j}{\partial x_i} \right), \quad (4.4)$$

$$\Omega_{ij} = \frac{1}{2} \left(\frac{\partial u_i}{\partial x_j} - \frac{\partial u_j}{\partial x_i} \right). \quad (4.5)$$

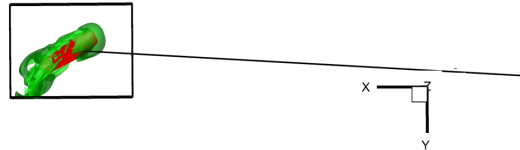
Larger vortices are observed during the power phase (Fig. 4.19(a) and Fig. 4.19(b)) compared to the retraction phase (Fig. 4.19(e)), since the kite has a lower angle of attack in the retraction phase due to reel-in along the tether direction.

Kite orientation angles in pitch, roll and yaw for the baseline simulation are presented in Fig. 4.20. Both the desired (trim) and actual kites angles are shown. The actual kite angles are driven to the trim values which confirms the effectiveness of the PID controller. While the kite roll angle maintains a negative constant value, the kite pitch and yaw angles vary during the reel-out phase to generate cross-current motion. During the reel-in phase, the kite is trimmed to obtain net positive power.

The effective angle of attack is defined based on the kite chord line and the kite



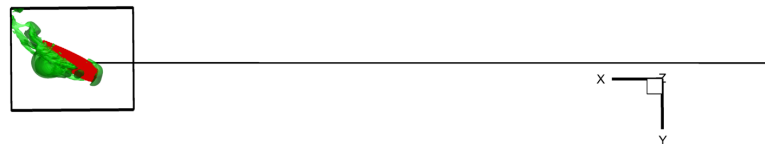
(a) Kite position at 28 s - Power phase.



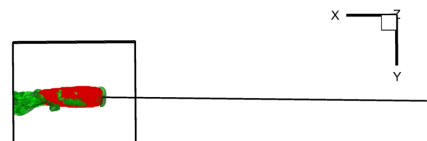
(b) Kite's position at 44 s - Power phase.



(c) Kite's position at 57 s - Power phase.



(d) Kite's position at 84 s - Beginning of retraction phase.



(e) Kite's position at 135 s - Retraction phase.

Figure 4.19: Top view of the kite position with flow vorticity (λ_2) contours.

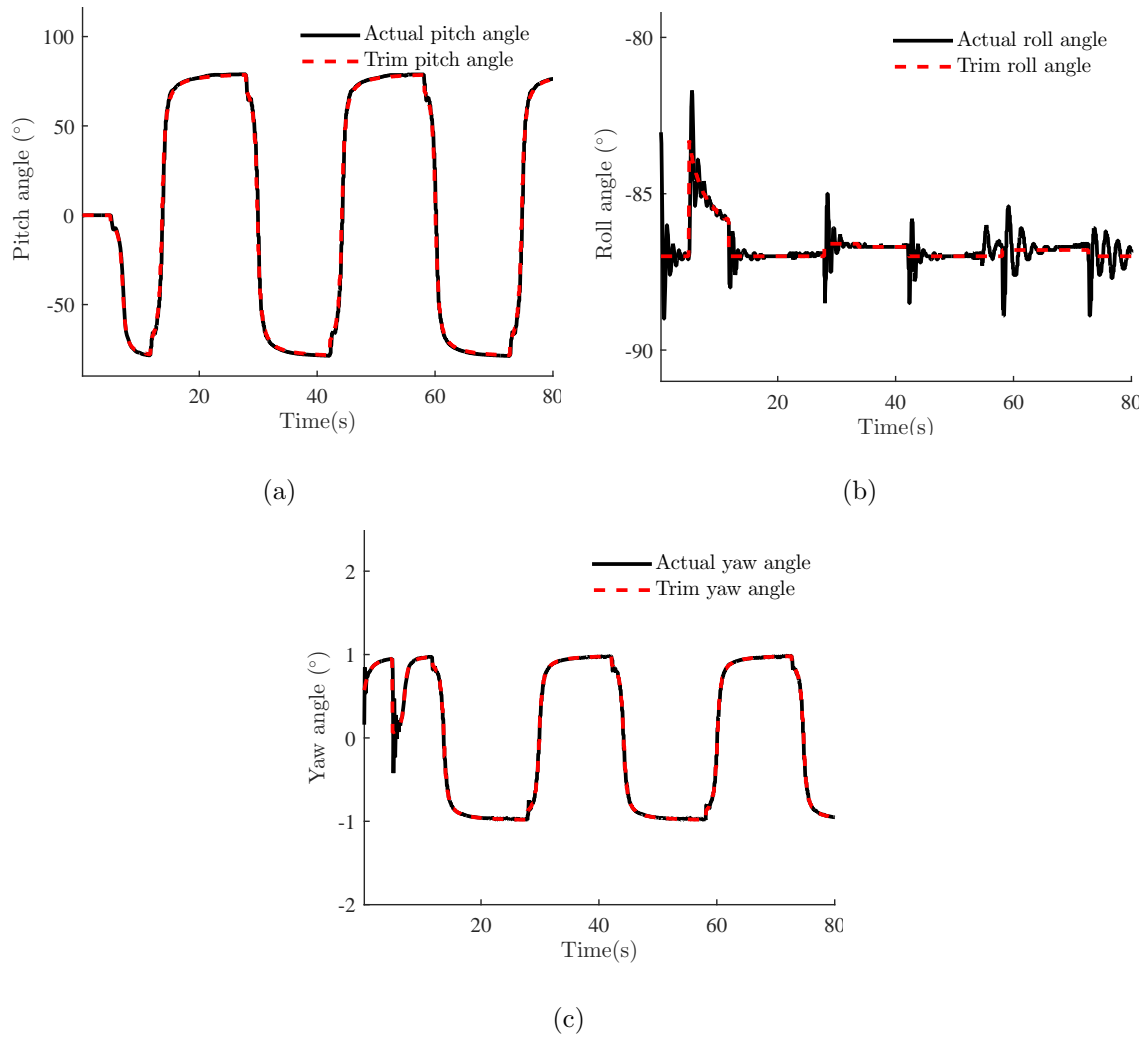


Figure 4.20: Comparison of the actual and trim kite angles vs time. a) Pitch angle
b) Roll angle, c) Yaw angle.

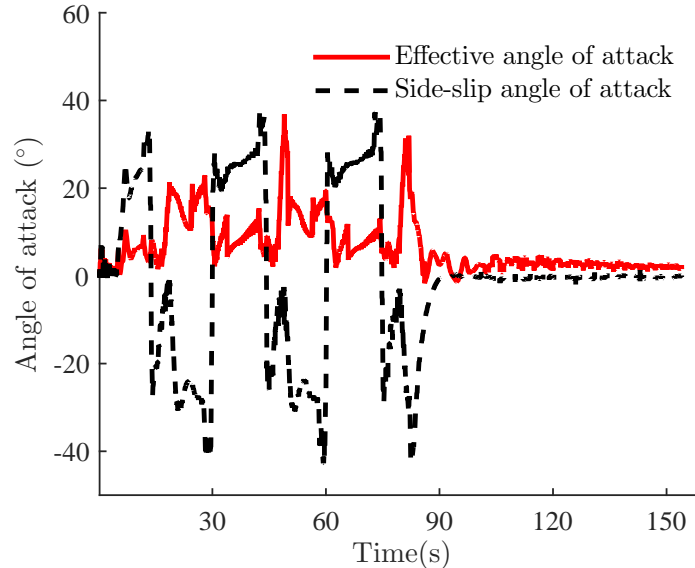


Figure 4.21: Effective and side-slip angles of attack of the kite vs time.

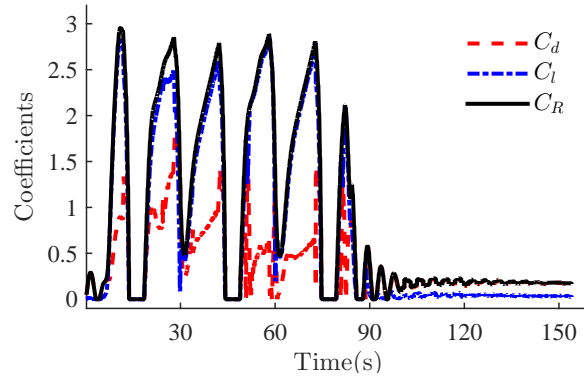
apparent velocity vector. The side-slip angle is obtained as follows:

$$\theta_{side-slip} = \text{Arcsin}\left(\frac{U_{app.,y}}{V_{app.}}\right). \quad (4.6)$$

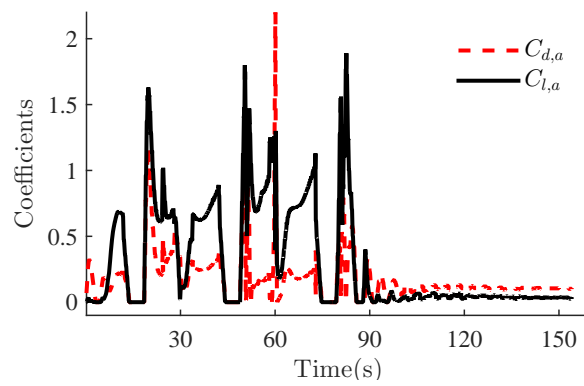
Here, $U_{app.,y}$ and $V_{app.}$ are the kite apparent velocity component in cross-current direction (Fig. 4.17(a)), and the magnitude of kite apparent velocity, respectively.

Hydrodynamic lift, drag and resultant coefficients (C_L , C_d , C_R) on the kite are shown in Fig. 4.22. The lift to drag ratio ($\frac{C_L}{C_d}$) in the 3D baseline simulation is around 3.0 as shown in Fig. 4.23.

It should be noted, a baseline simulation with no-slip condition at the kite interface was performed. Hydrodynamic lift, drag and resultant coefficients (C_L , C_d , C_R) on the kite for no-slip simulation are shown in Fig. 4.24. The observed C_R/C_d ratio in Fig. 4.24 is around 1.5, which is due to low grid resolution as explained in section 3.3. The lower C_R/C_d affects on the generated power as presented in Fig. 4.25. The power consumption during the retraction phase is high due to the large value of the kite



(a) The current velocity is used to calculate C_l , C_d , and C_R



(b) The apparent velocity is used to calculate $C_{d,a}$, $C_{l,a}$.

Figure 4.22: Lift, drag and resultant coefficients for the kite vs time .

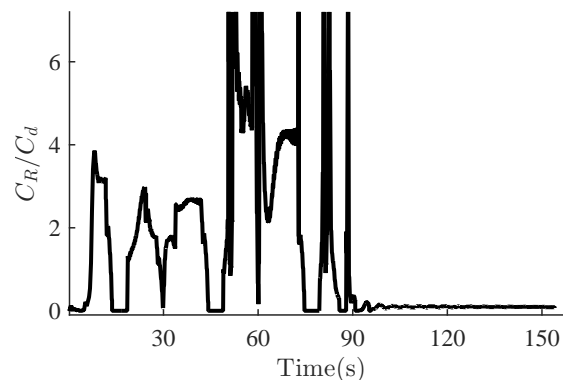


Figure 4.23: The ratio C_R/C_d for the kite.

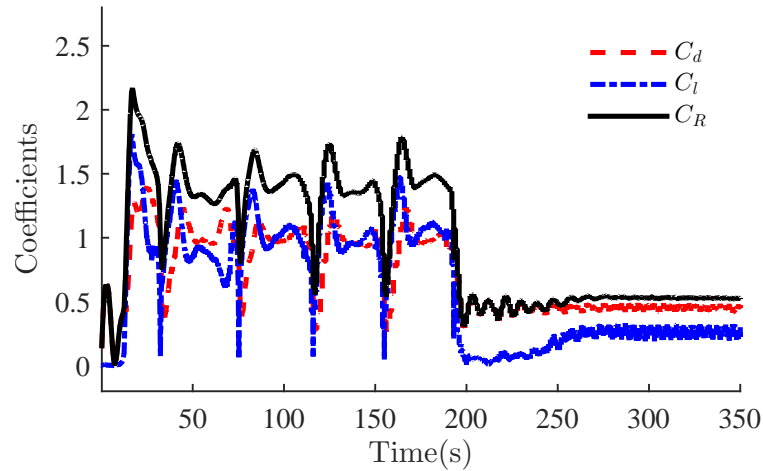


Figure 4.24: Lift, drag, and resultant coefficients of the kite using a no-slip boundary condition at the kite interface.

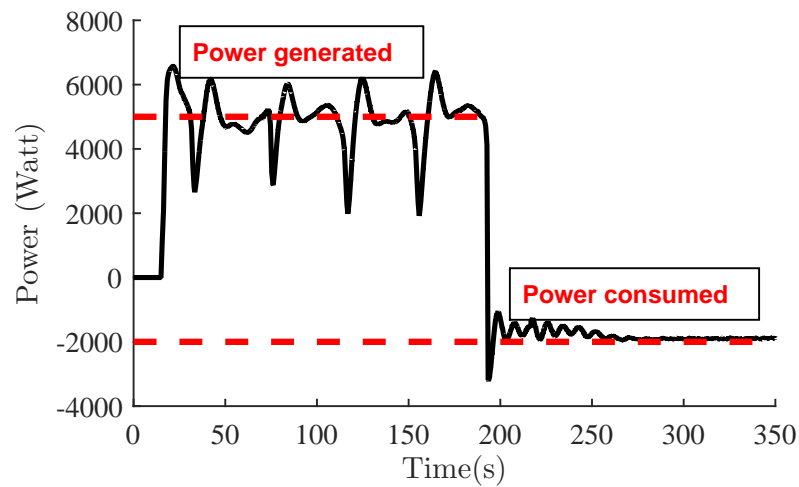


Figure 4.25: Power output using a no-slip boundary condition at the kite interface.

drag during this phase. It leads to decrease the net power output of TUSK system in a power-retraction cycle.

The tether tension for the 3D baseline simulation during the power and retraction cycle is shown in Fig. 4.26(a). Predicted tether tension can help to determine required tether materials for TUSK systems. The rest length of the tether is changed with a

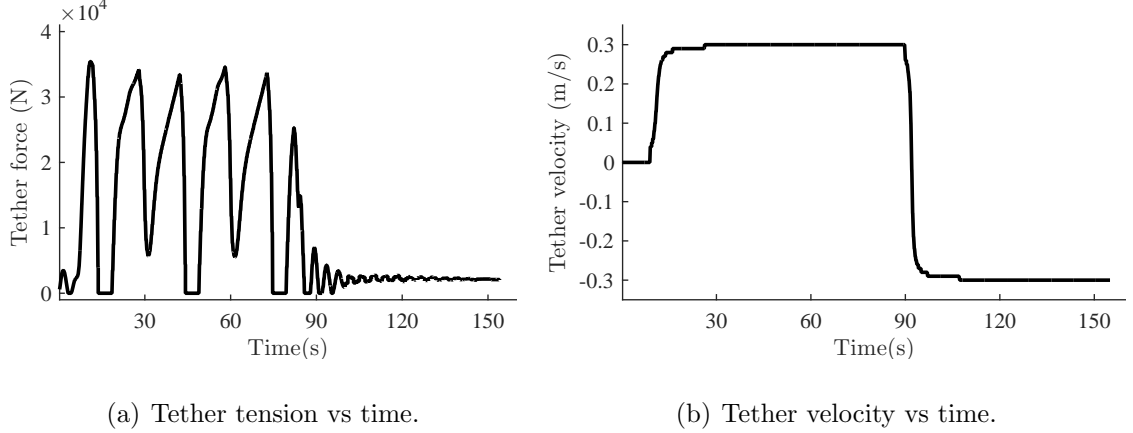


Figure 4.26: Tether parameters in the 3D baseline simulation using slip condition at the kite interface.

constant rate during reel-in and reel-out phases while the actual length is determined from the hydrodynamic forces applied on the kite.

Power is calculated by multiplying the tether tension (Fig. 4.26(a)) by the reel-out or reel-in velocity of the tether (Fig. 4.26(b)) which is 30 % of the ocean current velocity in the power and retraction phases. As is demonstrated in Fig. 4.27 the average power that is generated during reel-out is around seven times higher than the consumed power in the reel-in phase.

The value of the analytical maximum power based on the parameters of this simulation, which is calculated by Eq. 1.1, is also shown in Fig. 4.27. It shows that the efficiency of the TUSK system which is studied in the baseline simulation is around 42%. The efficiency is defined by:

$$\eta_p = \frac{\bar{P}_{act.}}{P_{max.}}, \quad (4.7)$$

where, $\bar{P}_{act.}$ and $P_{max.}$, are the average power output from the numerical simulation and the maximum analytical power proposed by Loyd [15], respectively. Moreover,

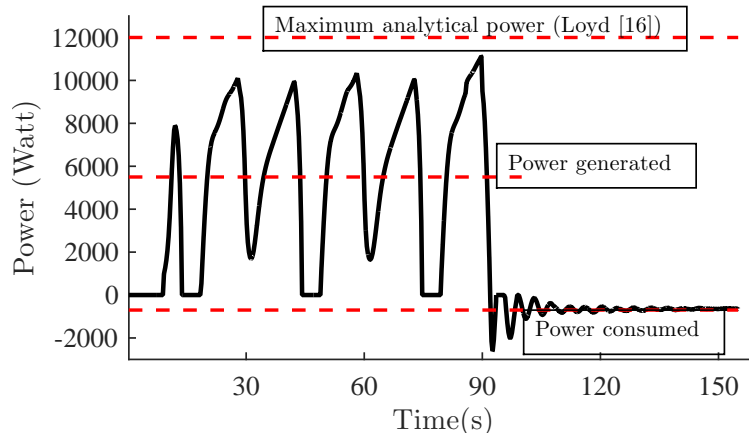


Figure 4.27: Power output of 3D baseline simulation vs time.

the power coefficient of the baseline simulation is calculated by

$$C_P = \frac{P}{\frac{1}{2}\rho A_{cross-current} V_c^3}, \quad (4.8)$$

where, P is the net power obtained in a power-retraction cycle, V_c is the current velocity, and $A_{cross-current}$ is the area swept by kite during cross-current motion. It shows that $C_p = 0.035$ for the baseline simulation which does not violate Betz limit.

4.2.1 Tether Retraction Velocity

The effect of tether velocity during the retraction phase, on power output of TUSK systems is also studied, where four different simulations have been performed. While the tether velocity is kept to $V_t = 0.3 \text{ m/s}$ during the power phase, the tether retraction velocity is set to 0.3 m/s , 0.6 m/s , 0.9 m/s and 1.2 m/s for the four different simulations. The other input values are given in Table 4.2.

The tether force and the tether velocity for the simulations are shown in Fig. 4.28. It can be seen by increasing the tether retraction velocity during the retraction phase,

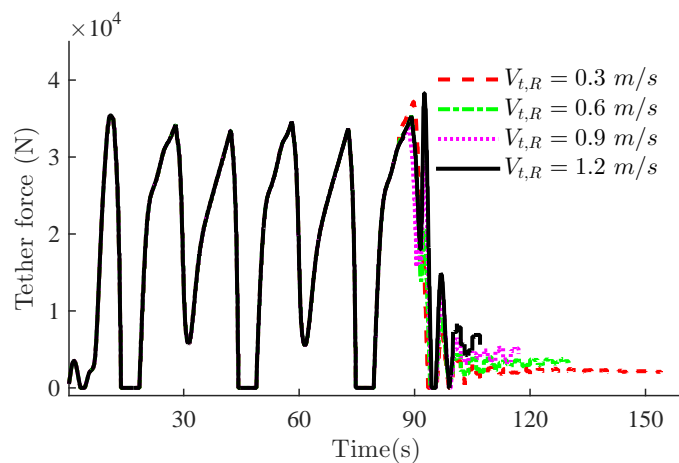
from 0.3 m/s to 0.6 m/s , the tether force increases by the ratio of $(\frac{1.6}{1.3})^2$ (the ratio of square of the apparent velocities for the two simulations). Note that the current velocity is 1 m/s . Also, the tether force approximately increases by the ratio of $(\frac{1.9}{1.3})^2$ and $(\frac{2.1}{1.3})^2$ compared to the baseline simulation, when the kite retracts with 0.9 m/s and 1.2 m/s , respectively as illustrated in Fig. 4.28(b).

Figure 4.29 shows the instantaneous power output during the power-retraction cycle for the different tether retraction velocities. Although increasing V_t during reel-in phase leads to increase the power consumption, it reduces the kite retraction time.

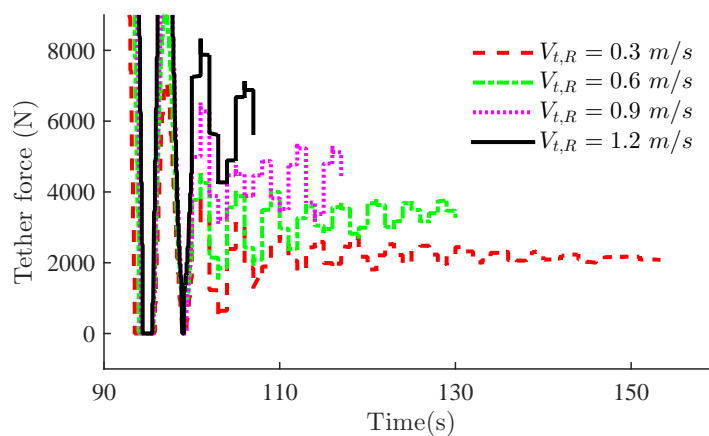
The net power output during a power-retraction cycle, P_{cycle} , is calculated by:

$$P_{cycle} = \frac{P_P \times t_P - P_R \times t_R}{t_P + t_R}, \quad (4.9)$$

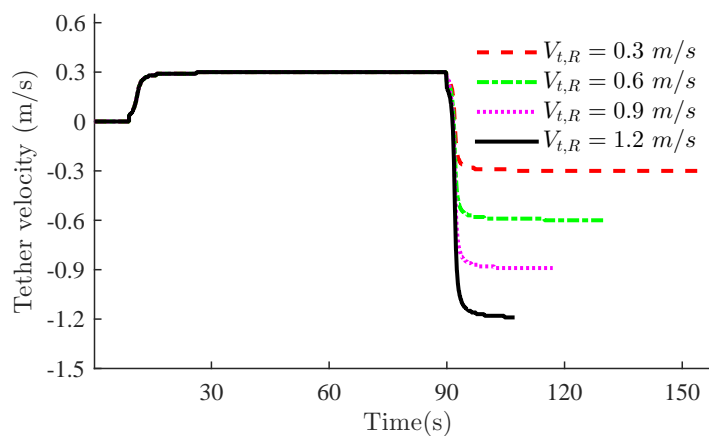
where, P_P , P_R , t_P , and t_R , are the average power obtained during power phase, average power consumed during retraction phase, duration of the power phase and duration of the retraction phase, respectively. The net power output at different ratios of the tether velocity during the power phase to the tether velocity during the retraction phase (γ_{out}/γ_{in}) is shown in Fig. 4.30(a). It illustrates that the maximum net power output during a power-retraction cycle occurs at $\frac{\gamma_{out}}{\gamma_{in}} = 0.33$. Moreover, the effect of the ratio of tether force during the retraction phase over the tether tension during the power phase (T_{in}/T_{out}) on net power output is shown in Fig. 4.30(b). It shows that T_{in}/T_{out} would be around 0.2 to reach the maximum net power output for a power-retraction cycle. Also, Fig. 4.30(c) shows the net power output versus the four ratios of power input which is consumed during the retraction phase over the power output obtained during the power phase (P_{in}/P_{out}). The maximum net power output occurs at $P_{in}/P_{out} = 0.7$. The ratios of T_{in}/T_{out} and P_{in}/P_{out} are obtained from the output of the simulations while the γ_{out}/γ_{in} is an input ratio.



(a) The tether force vs time.



(b) The tether force during the retraction phase vs time (zoom-in).



(c) The tether velocity vs time.

Figure 4.28: The tether parameters at four different tether retraction velocities.

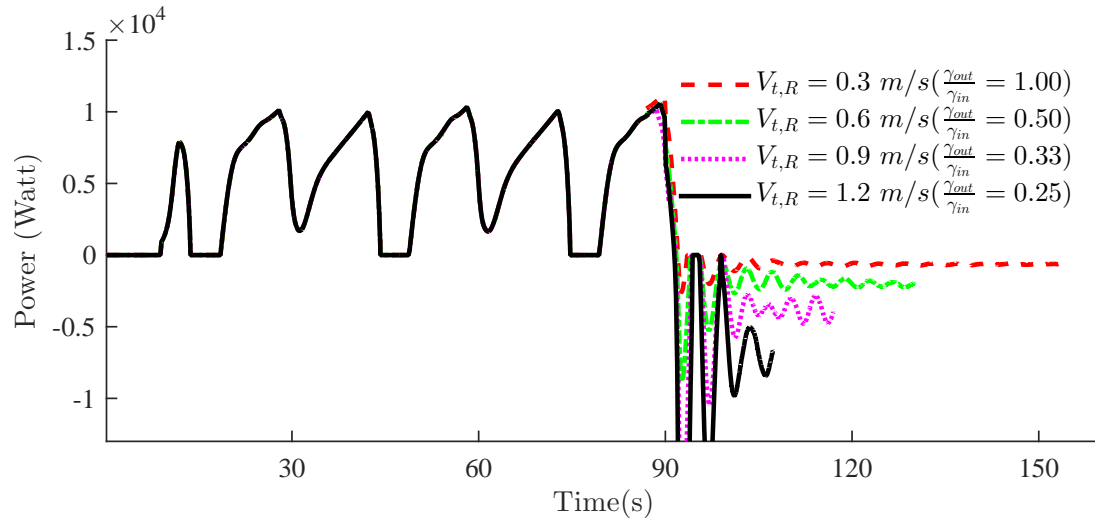


Figure 4.29: Power output vs time at four different tether retraction velocities.

In AWE systems Ahrens et al. [34] found the optimum net power at different ratios of γ_{out}/γ_{in} , T_{in}/T_{out} , and P_{in}/P_{out} versus the cube of lift to drag ratio $(L/D)^3$ as shown in Fig. 4.31. It shows that for the $(L/D)^3 = 27$ (the lift to drag ratio for the 3D baseline simulation) the maximum power for a power-retraction cycle is obtained at $\frac{\gamma_{out}}{\gamma_{in}} = 0.3$, $T_{in}/T_{out} = 0.2$, and $P_{in}/P_{out} = 0.7$. Figures 4.30 and 4.31 illustrate that the current numerical results for TUSK systems match well with the theory in AWE systems done by Ahrens et al. [34].

4.2.2 Tether Drag Effect

In this section, the influence of the tether drag on the performance of TUSK systems is investigated. The method for implementation of the tether drag effect is explained in section 2.12 [13]. The effect of tether drag on kite performance has been considered in AWE systems. The effect of tether drag can usually not be neglected, and can be a significant portion of overall drag on the kite. The tether drag can become the

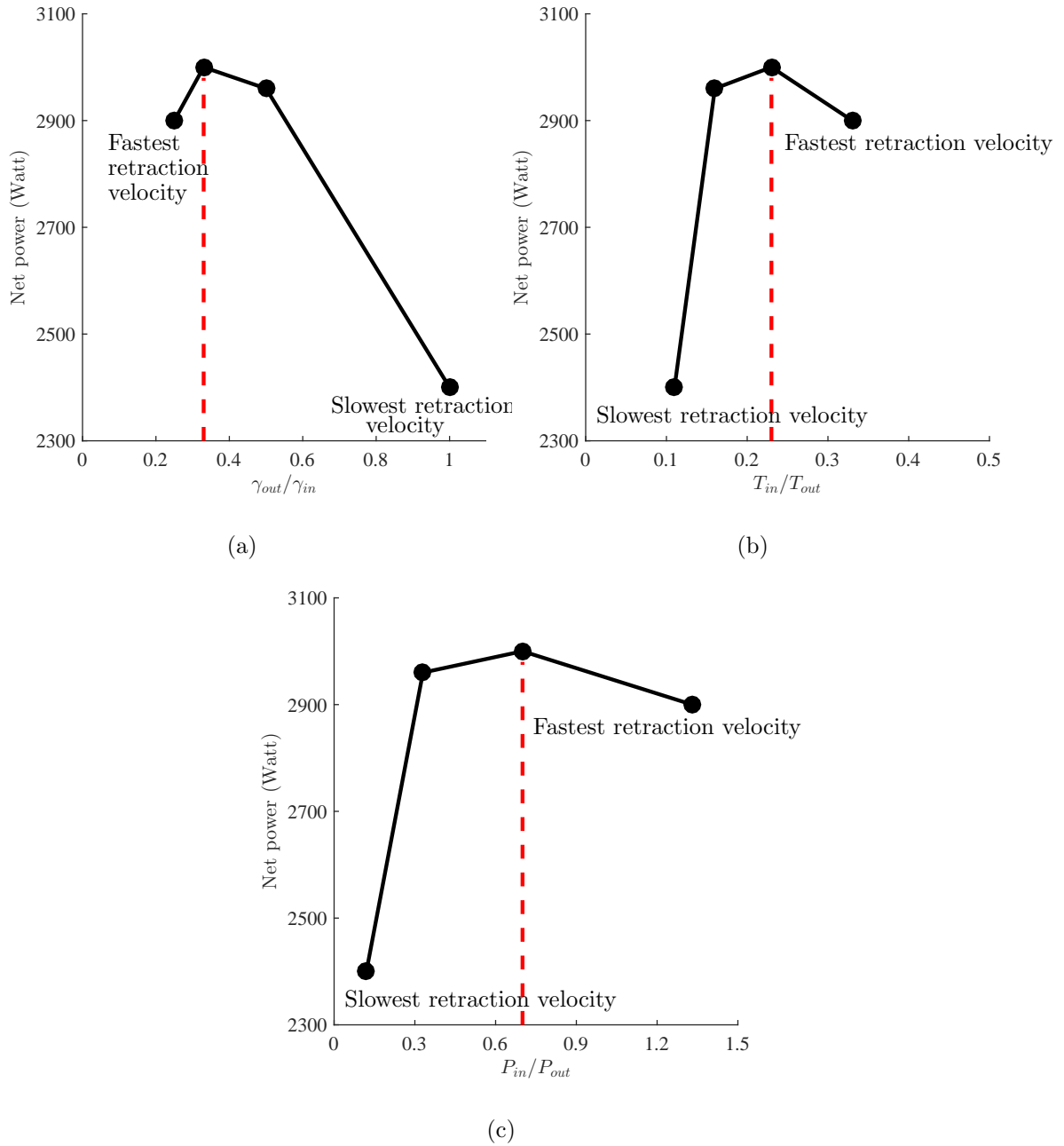


Figure 4.30: a) The net power output at four different ratios of tether velocity during the reel-out phase to tether velocity during the reel-in phase (γ_{out}/γ_{in}). b) The net power output at four different ratios of tether tension during the reel-in phase to tether tension during the reel-out phase (T_{in}/T_{out}). c) The net power output at four different ratios of power output during the reel-in phase to power output during the reel-out phase (P_{in}/P_{out}).

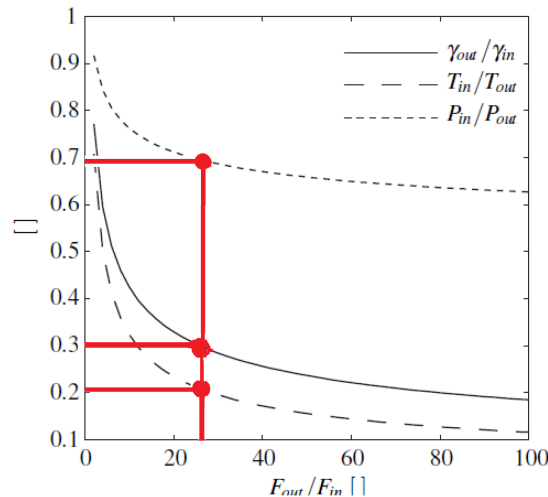


Figure 4.31: Optimum power output at different ratios of tether reel-out to tether reel-in speed (γ_{out}/γ_{in}), tether force ratio (T_{in}/T_{out}), and power ratio of reel-in to reel-out (P_{in}/P_{out}) vs the cube of lift to drag ratio ($F_{out}/F_{in} = (C_l/C_d)^3$) [34].

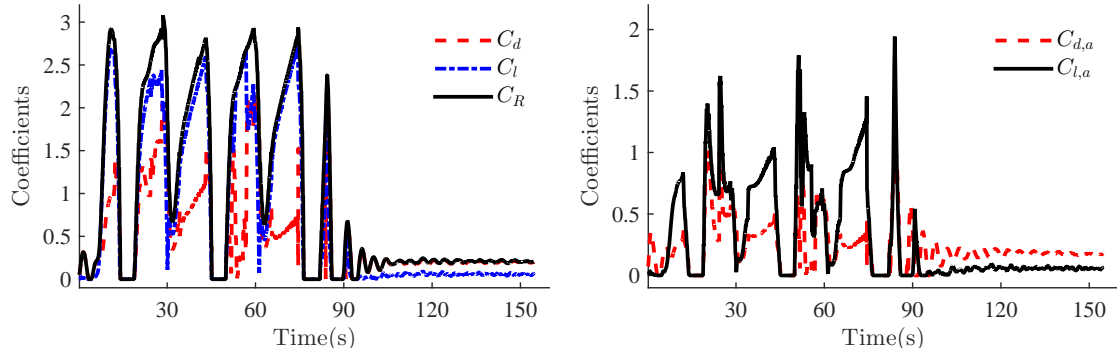
dominant drag contribution for very efficient airfoils [105].

Hydrodynamic lift, drag and resultant coefficients (C_L , C_d , C_R) of the kite are shown in Fig. 4.32. As mentioned earlier, it is seen in literature [13], that the apparent velocity, V_a , is used to calculate non-dimensional lift and drag forces of the kite which are shown in Fig. 4.32(b).

The total drag on the kite system is now calculated based on:

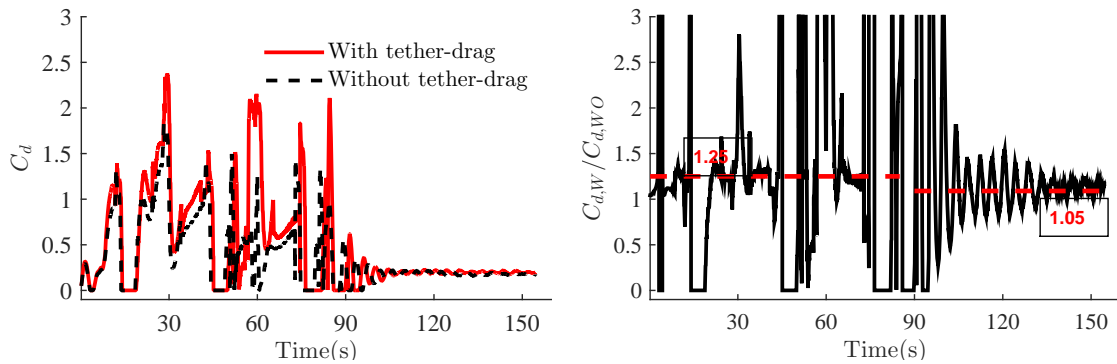
$$C_d = C_d^k + C_d^{tet.} \quad (4.10)$$

Here, C_d is the total kite drag coefficient, and C_d^k , and $C_d^{tet.}$ are the kite drag and the tether drag coefficients, respectively. Figure 4.33 demonstrates that the drag of the TUSK system increases by about 25% during the power phase when the tether drag is included as shown in Fig. 4.33(b). It also demonstrates that the tether drag has a small effect on kite drag during the retraction phase, since the kite is retracted along



(a) The current velocity is used to obtain kite hydrodynamic coefficients. (b) The apparent velocity is used to obtain kite hydrodynamic coefficients.

Figure 4.32: Hydrodynamic coefficients of the kite vs time .



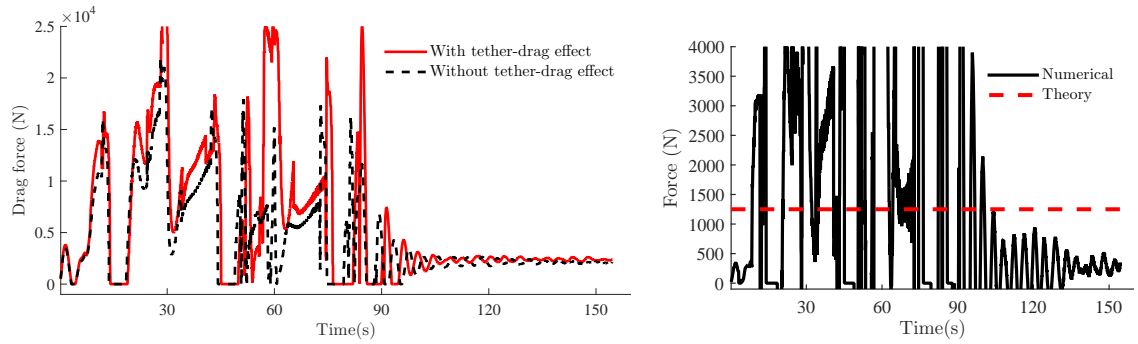
(a) The kite drag coefficient vs time. (b) The ratio of the kite drag with and without the tether drag.

Figure 4.33: Comparison of kite drag coefficient with and without the tether drag effect.

the tether direction.

Houska and Diehl [106] claimed that for AWE systems the effective tether drag force with respect to the perpendicular component of the wind can be calculated by:

$$F_f = \frac{1}{8} C_{tD} \rho d l V_a^2. \quad (4.11)$$



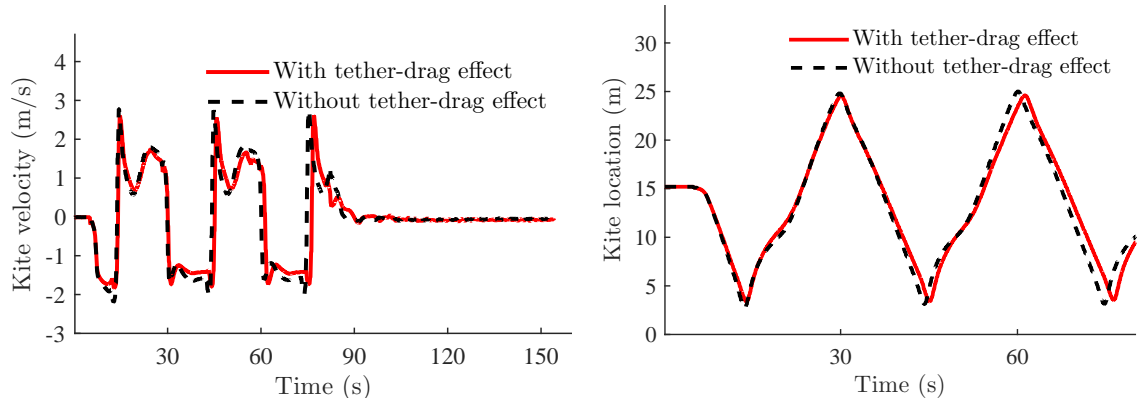
(a) The kite drag force with and without the tether-drag effect. (b) The additional kite drag force due to the tether drag effect compared to the theory [106].

Figure 4.34: The effect of the tether drag on the kite drag force.

Here, d and l are the diameter and length of the tether. V_a is the apparent kite velocity, and C_{tD} the drag coefficient of the tether with respect to the perpendicular component of the wind. In this simulation d , and l are 0.025 m and 100 m , respectively and C_{tD} is 1.2 [23]. Therefore, based on the input parameters of the simulation and Eq. 4.11, the theoretical value of the tether drag force is around 1200 N . The kite drag force with and without considering the effect of the tether drag, and the difference between two drag forces are shown in Fig 4.34(a) and Fig. 4.34(b), respectively. It shows that the net drag force found by the simulation is in a reasonably good agreement with the theoretical result by Houska and Diehl [106].

The effect of the tether drag on the trajectory and the velocity of the kite is also shown in fig. 4.35. Figure 4.35(a) shows that the kite velocity in the cross-current direction decreases around $10 - 15\%$ when the effect of tether drag is included.

Moreover, the effect of the tether drag on the tether tension force is studied. Figure 4.36 and Fig. 4.37 illustrate that the effect of the tether drag on the tether tension



(a) The cross-current velocity of the kite vs time. (b) The cross-current trajectory of the kite vs time.

Figure 4.35: The effect of the tether drag on the kite trajectory and velocity in the cross-current direction.

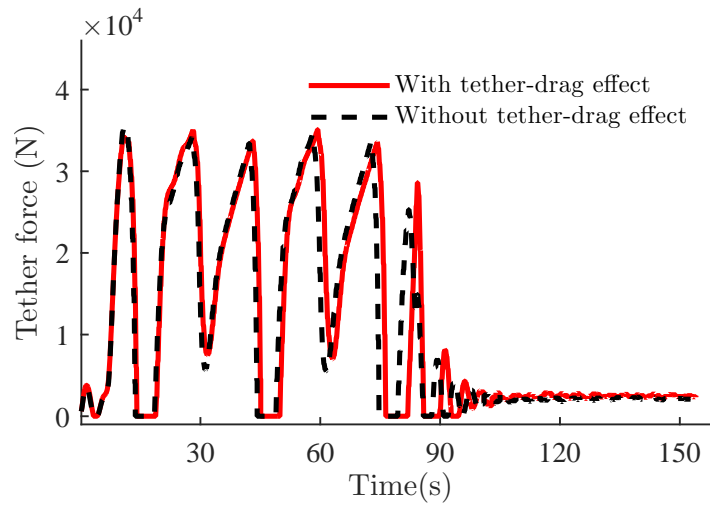


Figure 4.36: The effect of tether drag on the tether force.

and the power generation for the proposed concept of TUSK systems is small.

Since the tether force F_t can be obtained by:

$$F_t = \sqrt{L^2 + D^2}, \quad (4.12)$$

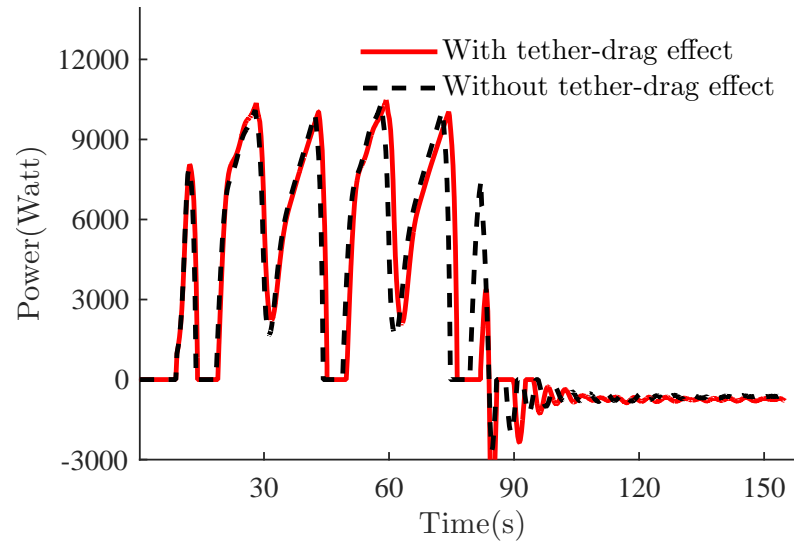


Figure 4.37: The effect of tether drag on the power generation.

It shows that at a larger value of lift to drag ratio ($L/D \geq 3$), the tether tension would be approximately equal to the kite lift force. Therefore, the increase in the kite drag due to the tether drag would have a small effect on the tether tension, and consequently on the power generation for the proposed TUSK concept. However, the effect of the tether drag on the other concept of the TUSK systems should be considered in future.

Chapter 5

Conclusion

This chapter presents a summary and a discussion of the results, and concludes by recommending future steps that can enhance this work.

5.1 Discussion and Conclusion

A computational method has been developed to predict the response of an underwater wing to an ocean current. In TUSK systems, the kite forces are transmitted via extendable tethers to produce power from the ocean current. The method is based on solving the unsteady Navier-Stokes equations with a two-step projection method coupled with OpenMP acceleration. Fluid-kite interaction is captured by the immersed boundary method, which initially considers the kite as a fluid. Therefore, the governing equations for the fluid are solved in the entire computational domain, including the kite domain, and then the kite rigidity condition is imposed. The tethers are modeled using reduced order model in which a simple Hooke's law is used and the effect of tether damping is included. Ocean current is modeled as a constant and uniform thrust force.

As a preliminary step, a numerical model is developed to test a 2D baseline simulation

in which the kite geometric angle of attack is controlled by altering the unstretched length of the tethers to obtain periodic power and retraction phases. A baseline simulation and the effect of varying key parameters in 2D TUSK systems are investigated in this study. The power generated for the two-dimensional baseline simulation matches well with theoretical results from Loyd [15].

A moving numerical domain method is then developed to allow computations of higher amplitude of cross-current motions in a reasonable time. The accuracy of the moving numerical domain method is verified by performing two different test cases. Moreover, the effect of slip and no-slip boundary condition at the kite interface is studied. The grid resolution and Reynolds number independency of the results have also been established. A PID controller is used to adjust the kite pitch, roll and yaw angles during a power-retraction cycle to achieve cross-current kite motion during the power phase, and kite motion along the tether direction during the retraction phase. It has been demonstrated that using slip condition at the kite interface leads to more accurately estimates of kite lift and drag forces in coarse grid resolutions. A baseline simulation study of a full-scale TUSK system is conducted. Vorticity flow fields and effective kite angle of attack are determined for a baseline simulation which shows the formation of larger vortices behind the kite during the power phase compared to the retraction phase, due to higher kite angle of attack. Tether parameters such as tension, reel-in and reel-out velocities are resolved for a baseline simulation to determine required tether materials for TUSK systems. The kite trajectory, hydrodynamic coefficients for the kite and the power generated are also captured. Also, the effect of tether retraction velocity is studied. The optimum condition for tether velocity is observed during reel-in phase to increase the net power of a cycle. The results are verified with theoretical results from Ahrens et al. [34]. Moreover, the effect of the

tether drag is investigated and compared with the results of the 3D baseline simulation. It shows that the kite drag coefficient increases by 25% with including the effect of the tether drag into the baseline simulation. It affects the trajectory and the velocity of the kite. However, it has a small effect on the power generation for the proposed concept of TUSK system.

5.2 Recommendations for Future Work

The goal of this work was the development of a nonlinear model to fully capture the nonlinear response of tethered underwater kite system to ocean currents. Therefore, the developed computational method focuses on modeling of 3D tethered underwater wing in a uniform ocean current in which rather simple models are used for the kite shape and the tether modeling. It is highly desirable to integrate the wing shape and developed hydrodynamic model with more robust models in future.

Considering the effect of ocean current velocity profile near the ocean surface would be an interesting step as a future goal. The variation of the current velocity in time could also be considered.

Although the computational method is parallelized with OpenMP, it would be interesting to parallel the computational tool with more advance parallelization scheme such as Graphic Process Unit (GPU) acceleration to reduce the computational time and increase the robustness of the model to capture smaller scale physics, specially on the solid-fluid interface.

In the current code, a turbulence model is not included. LES turbulence model can be added to the developed approach to increase the performance of the model in order

to be able to cover a broader range of the simulations.

Simple control methods are used to control the kite geometric angle of attack in the simulations. Application of more complex kite control schemes to control the effective angle of attack should be considered as a future work.

The straight-line geometry of the tether is considered in this study. It would be interesting to consider the effect of complex shapes of the tether such as non-straight cable with different tether materials on the TUSK performance.

The developed model could also be extended to simulate other systems in marine environments, especially for renewable energy technologies. Fly-Gen configuration of underwater kite systems could be studied in future where the effect of the turbine blades and cavitation should be considered.

Bibliography

- [1] R. Moodley, M. Nihontho, S. Chowdhury, and S. P. Chowdhury. A technical and economic analysis of energy extraction from the Agulhas current on the east coast of South Africa. *IEEE Power and Energy Society General Meeting: New Energy Horizons - Opportunities and Challenges*, pages 355–361, 2012.
- [2] A. Duerr and M. R. Dhanak. An assessment of the hydrokinetic energy resource of the florida current. *IEEE Journal of Oceanic Engineering*, 37(2):281–293, 2012.
- [3] M. Landberg. Submersible plant, international patent application PCT /EP2007 /050924, 2007.
- [4] R. Fredette. Scale-model testing of tethered undersea kites for power generation. MS Thesis, Worcester Polytechnic Institute, Worcester, US, 2015.
- [5] A. Cherubini, A. Papini, R. Vertechy, and M. Fontana. Airborne wind energy systems: A review of the technologies. *Renewable and Sustainable Energy Reviews*, 51:1461–1476, 2015.
- [6] F. Ferguson. Systems and methods for tethered turbines. PCT patent application WO2006117593.
- [7] F. Ferguson. systems and methods for tethered turbines. PCT patent application WO2010007466.
- [8] Makani Power website. Deep Green technology. www.google.com/makani, 2014.

- [9] Joby Energy website. <http://www.jobyenergy.com>, 2014.
- [10] Altaeros Energies website. <http://www.altaerosenergies.com>., 2014.
- [11] M. Diehl. Airborne wind energy: Basic concepts and physical foundations. In *Airborne wind energy*, pages 3–22. Springer, 2013.
- [12] Minesto Company. Deep green technology. tidalenergytoday.com/2016/07/07/minesto-grabs-deep-green-rd-funding, 2016.
- [13] P. Williams, B. Lansdorp, and W. Ockels. Optimal crosswind towing and power generation with tethered kites. *Journal Guidance, Control and Dynamics*, 31(1):81–93, 2008.
- [14] M. Canale, L. Fagiano, and M. Milanese. Kitegen: A revolution in wind energy generation. *Energy*, 34:355–361, 2009.
- [15] M.L. Loyd. Crosswind kite power. *Energy*, 4(3):106–111, 1980.
- [16] I. Lazakis, O. Turan, and T. Rosendahl. Risk assessment for the installation and maintenance activities of a low-speed tidal energy converter. In *Marine & Offshore Renewable Energy, London, UK*, London, UK, 2012.
- [17] I. Lazakis, O. Turan, and T. Rosendahl. In *Proceedings of the PRADS2013, London, UK*.
- [18] M. Jansson. Hydrodynamic analysis and simulation of a tidal energy converter. MS Thesis, Lund University, Lund, Sweden, 2013.
- [19] Hydrorun Company. www.Hydrorun.ca, 2015.
- [20] SeaCurrent Company. <https://seaurrent.com/a>, 2015.
- [21] Japan New Energy and Industrial Technology Development Organization. https://motherboard.vice.com/en_us/article/ypwqnm/

japanisbuildingunderwaterkitesstoharnesstheoceancurrentforpower,
2014.

- [22] D. J. Olinger and Y. Wang. Hydrokinetic energy harvesting using tethered undersea kites. *Journal of Renewable and Sustainable Energy*, 7(4):1–18, 2015.
- [23] Y. Wang and D. J. Olinger. Modeling and simulation of tethered undersea kites for power generation. In *Proceedings of the ASME ASME 10th International Conference on Energy Sustainability*. American Society of Mechanical Engineers, NC, USA, 2016.
- [24] H. Li, D. J. Olinger, and M. A. Demetriou. Passivity based control of a tethered undersea kite energy system. In *Proceedings of the 2016 American Controls Conference of the IEEE Controls Systems Society, Control of Airborne Wind Energy Systems I Session, Boston, USA, July , 2016*.
- [25] H. Li, D. J. Olinger, and M. A. Demetriou. Control of a tethered undersea kite energy system using a six degree of freedom model. In *Proceedings of the 2016 IEEE Conference on Dynamics and Control, Japan, 2016*.
- [26] M.L. Loyd. Wind driven apparatus for power generation. US patent application US4251040.
- [27] W. Ockels. A novel concept to exploit the energy in airspace. *Aircraft Design*, 4(2):81–97, 2001.
- [28] D. J. Olinger and J. S. Goela. Performance characteristics of a 1 kw scale kite-powered system. *ASME Journal of Solar Energy Engineering*, 132:041009–1 041009–11, 2010.
- [29] L. Fagiano. *Control of tethered airfoils for high–altitude wind energy generation*. PhD thesis, Politecnico di Torino, 2009.
- [30] M. Erhard and H. Strauch. Flight control of tethered kites in autonomous pumping cycles for airborne wind energy. *Control Engineering Practice*, 40:13–

26, 2015.

- [31] H. Li, D. J. Olinger, and M. A. Demetriou. Attitude tracking control of an airborne wind energy system. In *Proceedings of the European Controls Conference, Linz, Austria*, Linz, Austria, 2015.
- [32] I. Argatov and R. Silvennoinen. Asymptotic modeling of unconstrained control of a tethered power kite moving along a given closed-loop spherical trajectory. *Journal of Engineering Mathematics*, 72(1):187–203, 2012.
- [33] C. L. Archer and K. Caldeira. Global assessment of high altitude wind power. *Energies*, 2(2):307–319, 2009.
- [34] U. Ahrens, M. Diehl, and R. Schemehl. *Airborne Wind Energy*. Springer, New York, 2014.
- [35] M. Ippolito. System and process for automatically controlling the flight of power wing airfoils. PCT Patent Application WO2007129341.
- [36] M. Canale, L. Fagiano, M. Ippolito, and M. Milanese. Control of tethered airfoils for a new class of wind energy generator. In *Decision and Control, 2006 45th IEEE Conference on*, pages 4020–4026. IEEE, 2006.
- [37] M. Ippolito. Aeolian system for converting energy through power wing airfoils. European Patent Application EP2463516a1.
- [38] M. Ippolito. Infrastructure for driving and assisted take-off of airfoils for tropospheric aeolian generator. PCT Patent Application WO2009147692.
- [39] A. Cherubini and M. Ippolito. Puleggia perfezionata per verricello ad alta efficienza. Italian Patent Application ITTO20130365.
- [40] S. Dunker. Ram-air wing design considerations for airborne wind energy. In *Airborne Wind Energy*, pages 517–546. Springer, 2013.

- [41] M. Ippolito. Tether for tropospheric aeolian generator. PCT Patent Application WO2010084520.
- [42] M. Ippolito. Tether for tropospheric aeolian generator. PCT Patent Application WO2010143214.
- [43] L. Fagiano and M. Milanese. Airborne wind energy: An overview. In *American Control Conference (ACC)*, pages 3132–3143. IEEE, 2012.
- [44] L. Fagiano, M. Milanese, and D. Piga. High-altitude wind power generation. *IEEE Transactions on Energy Conversion*, 25(1):168–180, 2010.
- [45] L. Fagiano, M. Milanese, and D. Piga. Optimization of airborne wind energy generators. *International Journal of robust and nonlinear control*, 22(18):2055–2083, 2012.
- [46] Kitenergy. <http://www.kitenergy.net>, 2014.
- [47] L. Fagiano M.L. Milanese and I. Gerlero. Actuating systems for controlling the flight of a power wing profile for conversion of wind energy into electrical or mechanical energy. PCT patent application WO2011121557.
- [48] M. Erhard and H. Strauch. Control of towing kites for seagoing vessels. *IEEE Transactions on Control Systems Technology*, 21(5):1629–1640, 2013.
- [49] S. Wrage and S. Brabeck. Wind power plant comprising a steerable kite. PCT Patent Application WO2007112993.
- [50] J. Maaß and M. Erhard. Software system architecture for control of tethered kites. In *Airborne wind energy*, pages 599–611. Springer, 2013.
- [51] S. Wrage and S. Brabeck. Starting and recovering device for an aerodynamic profiled element, and aerodynamic profiled element. PCT Patent Application WO2008019700.

- [52] R. Luchsinger, D. Aregger, F. Beazard, D. Costa, C. Galliot, and F. Gohl. Closing the gap: pumping cycle kite power with twings. In *Abstract submitted to the Airborne Wind Energy Conference. TU Delft*, 2015.
- [53] Kitepower. <http://kitepower.eu/newsevents>, 2015.
- [54] S. Haug. Design of a kite launch and retrieval system for a pumping high altitude wind power generator. Master’s thesis, 2012.
- [55] R. van der Vlugt, J. Peschel, and R. Schmehl. Design and experimental characterization of a pumping kite power system. In *Airborne wind energy*, pages 403–425. Springer, 2013.
- [56] S. Sieberling and R. Ruiterkamp. The powerplane an airborne wind energy system conceptual operations. In *Proceedings of the 11th AIAA ATIO conference*, 2011.
- [57] R. Ruiterkamp and S. Sieberling. Description and preliminary test results of a six degrees of freedom rigid wing pumping system. In *Airborne wind energy*, pages 443–458. Springer, 2013.
- [58] Ampyx Power website. <http://www.ampyxpower.com/SystemDevelopment.html>, 2014.
- [59] A. Bormann, M. Ranneberg, P. Kövesdi, C. Gebhardt, and S. Skutnik. Development of a three-line ground-actuated airborne wind energy converter. In *Airborne wind energy*, pages 427–436. Springer, 2013.
- [60] Windlift website. <http://www.windlift.com>, 2014.
- [61] K. Geebelen, M. Vukov, M. Zanon, S. Gros, A. Wagner, M. Diehl, D. Vandepitte, J. Swevers, and H. Ahmad. An experimental test setup for advanced estimation and control of an airbornewind energy system. In *Airborne Wind Energy*, pages 459–471. Springer, 2013.

- [62] SwissKitePower website. <http://www.swisskitepower.ch>, 2014.
- [63] Control NASA and tracking for tethered airborne wind energy (AWE) vehicles. http://technologygateway.nasa.gov/docs/TOA_LARC120_aWE_7web.pdf, 2014.
- [64] The New Yorker. M. Specter, Inherit the Wind. Deep Green technology. <http://www.newyorker.com/magazine/2013/05/20/inherit-the-wind>, 2013.
- [65] NB. Van C. Hardam, DV. Lind. Tethered system for power generation. US Patent Application US2010295303.
- [66] P. Lynn S. Griffith, C. Hardham and D. Montague. Faired tether for wind power generation systems. PCT patent application WO2009142762.
- [67] P. Lynn S. Griffith, C. Hardham and D. Montague. Bimodal kite system. US patent application US2009072092.
- [68] J. Bevirt. Tethered airborne power generation system with vertical take-off and landing capability. US Patent Application US2010283253a1.
- [69] J. Bevirt. Tethered airborne power generation system with vertical take-off and landing capability. US Patent Application US2010283253a1.
- [70] J. Bevirt and M. Peddie. System and method for controlling a tethered flying craft using tether attachment point manipulation. US Patent Application US2011121570a1.
- [71] C. Vermillion, B. Glass, and A. Rein. Lighter-than-air wind energy systems. In *Airborne Wind Energy*, pages 501–514. Springer, 2013.
- [72] B. Glass. Power-augmenting shroud for energy-producing turbines. PCT Patent Application WO2010045441.
- [73] C. Vermillion and B. Glass. Systems and methods for attitude control of tethered aerostats. PCT Patent Application WO2013043586.

- [74] BW. Roberts. Windmill kite. US Patent Application US6781254b1.
- [75] BW. Roberts. Control system for a windmill kite. PCT Patent Application WO2009126988a1.
- [76] BW. Roberts. Tethered airborne wind-driven power generator. US Patent Application US2011057453.
- [77] BW. Roberts. Electrical generating rotorcraft. PCT Patent Application WO2012024717a1.
- [78] eKite website. <http://www.e-kite.com/wp-content/uploads/2014/12/e-kite-in-sky.jpg>, 2015.
- [79] R. Lozano Jr, M. Alamir, J. Dumon, and A. Hably. Control of a wind power system based on a tethered wing. *IFAC Proceedings Volumes*, 45(1):139–144, 2012.
- [80] GIPSA lab website. http://www.gipsa-lab.grenoble-inp.fr/recherche/platesformes.php?id_plateforme=70, 2014.
- [81] Allister Furey’s personal website. <http://www.sussex.ac.uk/Users/adjf20/index.html>, 2013.
- [82] D. J. Olinger, J. S. Goela, and G. Tryggvason. Modeling and testing of a kite-powered water pump. In *Airborne Wind Energy*, pages 387–401. Springer, 2013.
- [83] H. H. Hu and D. D. Joseph. Direct simulation of fluid particle motions. *Theoretical and Computational Fluid Dynamics*, 3:285–306, 1992.
- [84] A. A. Johnson and T. E. Tezduyar. Simulation of multiple spheres falling in a liquid-filled tube. *Computer Methods in Applied Mechanics and Engineering*, 134:351–373, 1996.

- [85] T. Tezduyar, M. Behr, and J. Liou. A new strategy for finite element computations involving moving boundaries and interfaces the deforming spatial domain/spacetime procedure: I. the concept and the preliminary numerical tests. *Computer Methods in Applied Mechanics and Engineering*, 94:339–351, 1992.
- [86] N. Sharma and N. A. Patankar. A fast computation technique for the direct numerical simulation of rigid particulate flows. *Journal of Computational Physics*, 205:439–457, 2005.
- [87] C. S. Peskin. The fluid dynamics of heart valves: experimental, theoretical, and computational methods. *Annual review of fluid mechanics*, 14(1):235–259, 1982.
- [88] R. Mittal and G. Iaccarino. Immersed boundary methods. *Annual Review of Fluid Mechanics*, 37:239–261, 2005.
- [89] M. Uhlmann. An immersed boundary method with direct forcing for the simulation of particulate flows. *Journal of Computational Physics*, 209:448–476, 2005.
- [90] A. Ghasemi, A. Pathak, and M. Raessi. Computational simulation of the interactions between moving rigid bodies and incompressible two-fluid flows. *Computers & Fluids*, 94:1–13, 2014.
- [91] R. Glowinski, T. Pan, T. Hesla, and D. Joseph. A distributed lagrange multiplier/fictitious domain method for particulate flows. *International Journal of Multiphase Flow*, 25(5):755–794, 1999.
- [92] A. Mayo and C. Peskin. An implicit numerical method for fluid dynamics problems with immersed elastic boundaries. In: *Fluid Dynamics in Biology: Proceedings of an AMS-IMS-SIAM Joint Summer Research Conference, Contemporary Mathematics*, pages 261–277, 1993.
- [93] A. M. Ardekani, S. Dabiri, and R. H. Rangel. Collision of multiparticle and general shape objects in a viscous fluid. *Journal of Computational Physics*,

227(24):10094–10107, 2008.

- [94] S. V. Apte and N. A. Patankar. A formulation for fully resolved imulation (FRS) of particle-turbulence interactions in two-phase flows. *International Journal of Numerical Analysis and Modeling*, 5:1–16., 2008.
- [95] M. Martin, C. Patton, J. Schmitt, and S. V. Apte. Direct simulation based model-predictive control of flow maldistribution in parallel microchannels. *Journal of Fluids Engineering*, 131(11):111201 – 111218, 2009.
- [96] L. Dagum and R. Menon. Openmp: an industry standard api for shared-memory programming. *Computational Science & Engineering, IEEE*, 5(1):46–55, 1998.
- [97] C. S. Peskin. The immersed boundary method. *Acta numerica*, 11:479–517, 2002.
- [98] E.N. Jacobs, K.E. Ward, and R.M. Pinkerton. The characteristics of 78 related airfoil sections from tests in the variable-density wind tunnel. *NACA Report Number 460*, 1933.
- [99] A. Nematbakhsh, D. J. Olinger, and G. Tryggvason. A nonlinear computational model of floating wind turbines. *Journal of Fluids Engineering*, 135:1–13, 2013.
- [100] A. Ghasemi. Computational simulation of the interaction between moving rigid bodies and two-fluid flows. Master’s thesis, University of Massachusetts Dartmouth, MA, USA, 2013.
- [101] T. Yabe, F. Xiao, and T. Utsumi. The constrained interpolation profile method for multiphase analysis. *Journal of Computational Physics*, 169(2):556–593, 2001.
- [102] A. Ghasemi. *Specified Motion and Feedback Control of Engineering Structures with Distributed Sensors and Actuators*. PhD thesis, University of Kentucky, 2012.

- [103] S. Asao, K. Matsuno, and M. Yamakawa. Parallel computations of incompressible flow around falling spheres in a long pipe using moving computational domain method. *Computers & Fluids*, 88:850–856, 2013.
- [104] T. Kempe, M. Lennartz, S. Schwarz, and J. Fröhlich. Imposing the free-slip condition with a continuous forcing immersed boundary method. *Journal of Computational Physics*, 282:183–209, 2015.
- [105] I. Argatov and R. Silvennoinen. Structural optimization of the pumping kite wind generator. *Structural and Multidisciplinary Optimization*, 40(1):585–595, 2010.
- [106] B. Houska and M. Diehl. Optimal control of towing kites. In *Decision and Control, 2006 45th IEEE Conference on*, pages 2693–2697. IEEE, 2006.